Dissertation

Label-Free Cell Analysis:
An Infrared Sensor for CH_2-Stretch Ratio Determination and a Microfluidic Cell-Cell Separator

ausgeführt zum Zwecke der Erlangung des
akademischen Grades eines Doktors der
technischen Wissenschaften unter der Leitung von

Univ.-Prof. Dr. Michael J. Vellekoop

eingereicht an der Technischen Universität Wien
Fakultät für Elektrotechnik und Informationstechnik

von

Sander van den Driesche

Mollardgasse 66/2/11, 1060 Wien
Matr.-Nr. 0726989

Wien, im Mai 2011

Erstbegutachter	Prof. Dr. Michael J. Vellekoop Vienna University of Technology Vienna, Austria
Zweitbegutachter	Prof. Dr. Peter D.E.M. Verhaert Delft University of Technology Delft, The Netherlands

To my parents
Catharina and Gerard van den Driesche

Contents

Summary

In this thesis two label-free cell analysis topics are being discussed. The main subject is an infrared absorbance based sensor system for the determination of the CH_2-symmetric to CH_2-antisymmetric stretch ratio. It was investigated whether the designed label-free measurement method of the sensor system can aid in the detection of the presence of cancer cells.

The other topic is purification methods for cell samples from cell culture debris and bacteria contaminants. In particular the label-free separation method based on travelling wave dielectrophoresis (twDEP) was studied.

The majority of tumour detection methods available to date are based on visual inspection of primary tumours, standard histopathology techniques applied on tumour biopsies using Haematoxylin & Eosin staining, and immunohistopathology using antibodies against tumour antigens. Visual inspection methods are based on morphological interpretation, and therefore subjective, discrepancies in the diagnosis have been reported. Improved and objective diagnostic methods are highly important for increasing the overall survival rates of cancer patients.

The infrared sensor system, which measures a potential diagnostic variable for the detection of tumour cells and tissues within a short time span, records IR absorbance of the CH_2-symmetric and CH_2-antisymmetric stretch at 3.51 µm and 3.42 µm, respectively. In addition, the IR absorbance at two reference wavelengths is determined to compensate for variations in the sample thickness and water content. The main components of the designed and realised sensor system are mid-IR emitting LEDs, a photodiode, and narrow band-pass filters.

To investigate the potential of the realised sensor system, normal and various tumour cell lines originating from melanocytes and kidney epithelial are tested, both in dried condition and in suspension. The presented methodology yielded statistical significant CH_2-stretch ratio differences between the individual cell lines, normal and tumorous, of both epithelial kidney and melanocyte origin. Also, the mechanism influencing the CH_2-stretch ratio of mammalian cell membranes was investigated. A normal non-tumorous cell line was exposed to the plasma membrane bound cholesterol reducing agent methyl-β-cyclodextrin. Measurement results indicate that an increase in CH_2-stretch ratio arises when there is a decrease in the membrane stabilizing agent cholesterol. The sensing method allows the discrimination between normal and tumour cells. In addition, the method shows high potential for improvement of staging of suspicious tissues and can easily be adapted in a point-of-care instrument.

A microfluidic twDEP separator is designed and realised to separate specific cells from a mixture. Viable suspended-grown Jurkat cells were successfully separated from cell culture debris and *L. casei* bacteria.

In conclusion it is shown that label-free techniques can be applied to determine the presence of tumour cells and to separate or sort specific cells from a cell mixture. These methods promise simpler and more cost-effective analysis techniques that can be applied in diagnostic instrumentation and optimisation of curing therapies.

Nomenclature

0.1 List of Abbreviations

Symbol	Description
AC	alternating current
AZ5215	negative photoresist
B/W	bandwidth
CaF_2	calcium fluoride
DAQ	data acquisition
DC	direct current
DEP	dielectrophoresis
DI	de-ionized
DMEM	Dulbecco’s modified eagle medium
FACS	fluorescent activated cell sorting
FCS	fetal calf serum
FEM	finite element model
FTIR	Fourier transform infrared spectroscopy
FWHM	full width at half maximum
IR	infrared
LED	light emitting diode
M	molar
MβCD	methyl-β-cyclodextrin
MACS	magnetic activated cell sorting
MDCK	madin-darby canine kidney
NBP	narrow band-pass filter

Symbol	Description
nDEP	negative dielectrophoresis
NTC	negative temperature coefficient
PBS	phosphate buffered saline
PCB	printed circuit board
PD	photodiode
pDEP	positive dielectrophoresis
PDMS	polydimethylsiloxane
RPMI 1640	Roswell Park Memorial Institute medium
SU-8	epoxy-based negative photoresist
TEC	thermoelectric cooler
twDEP	travelling wave dielectrophoresis
UV	ultraviolet
%(w/w)	weight/weight percentage
%(w/v)	weight/volume percentage

0.2 List of Constants

Constant	Description	Unit
b	Wien's displacement constant	2.898×10^{-3} m·K
c	speed of light	2.998×10^{8} m/s
eV	electron volt	1.602×10^{-19} J
h	Planck's constant	6.626×10^{-34} m^{2}kg/s
N_A	Avogadro's number	6.022×10^{23} mol^{-1}
u	unified mass unit	1.661×10^{-27} kg
ε_0	vacuum permittivity	8.8542×10^{-12} F/m
π		3.142

0.3 List of Variables

Symbol	Description	Unit
A	area	m^2
A	absorbance	-
c	concentration	mol/liter
c_m	membrane capacitance	F/m^2
d	optical path length	m
E	energy	J
$E_{0,\mathrm{RMS}}$	absolute value of the electric field	V/m
$\vec{F}_\mathrm{DEP}$	dielectrophoretic force (vector)	N
$\vec{F}_\mathrm{drag}$	drag force on a particle (vector)	N
f	frequency	Hz
f_co	crossover frequency	Hz
f_CM	Clausius-Mossotti factor	-
f_ROT	rotational (ROT) spectra	s^{-1}
g_m	membrane transductance	S/m^2
I_in	incident light intensity	cd
I_out	transmitted light intensity	cd
j	imaginary unit, j = $\sqrt{-1}$	-
k	effective bond force	N/m
l	optical path length	m
m	mass	kg
m_a	atomic mass	u
m_r	relative atomic mass	u
r	particle or cell radius	m
T	temperature	K
T	transmittance	-
$\vec{v}_\mathrm{l}$	local liquid velocity (vector)	m/s

Symbol	Description	Unit
$\vec{v}_\mathrm{p}$	particle velocity (vector)	m/s
$\overline{v}$	frequency in wavenumbers	cm^{-1}
W	weighting factor	-
x, y, z	Cartesian coordinate axes	-
χ	scaling factor	-
δ	cell membrane thickness	m
η	dynamic viscosity	Pa·s
ε^*	complex permittivity	ε_0
ε	molar extinction coefficient	M^{-1}cm^{-1}
ε_m	medium permittivity	ε_0
ε_p1	membrane permittivity	ε_0
ε_p2	cytoplasm permittivity	ε_0
λ	optical wavelength	m
σ_m	medium conductivity	S/m
σ_p1	membrane conductivity	S/m
σ_p2	cytoplasm conductivity	S/m
ω	angular frequency	s^{-1}
$\Im_m[x]$	imaginary part of a number x	-
$\Re_e[x]$	real part of a number x	-

Chapter 1

Introduction

In recent years, the disease cancer has been one of the major causes of death [1]. The majority of tumour detection methods available to date are based on visual inspection of primary tumours, standard histopathology techniques applied on tumour biopsies using Haematoxylin & Eosin staining, and immunohistopathology using antibodies against tumour antigens [2]. As these inspection methods are based on morphological interpretation, and therefore subjective, discrepancies in the diagnosis have been reported [3,4]. Visual inspection methods still result in a high number of false positives and negatives and there is still no commonly accepted marker set available for the accurate diagnosis of malignant melanoma [3,5]. Between 1999 and 2005, the overall 5-year relative survival rates for kidney and renal pelvis cancer were 90.4% for localized tumours (malignancy limited to the organ of origin), 62.3% for regional tumours (invasion into surrounding organs and/or adjecent tissues; invasion into nearby lymph nodes), and 10.4% for distant tumours (travelled to other parts of the body, and have begun to grow at new locations). For melanoma these rates were respectively, 98.1%, 61.9%, and 15.3% [1,6]. These values show that early detection and accurate staging of the primary tumour will increase the overall survival rate tremendously. Renal cell carcinoma arises from renal tubular epithelial kidney cells. Melanoma originates from dendritic neural crest derived melanocytes, found in the basal cell layer of the epidermis, synthesizing the protective pigment melanin. The incidence of cutaneous melanoma is steadily increasing, faster than that of any other cancer over the past 20 years [7, 8]. Melanoma is characterized by a high tendency to develop metastases and the metastatic potential of melanoma is considerably greater than that of other solid tumours [9]. Once melanoma has metastasised, the average survival is up to 9 months [1].

1.1 Tumour diagnostic methods

Instead of using subjective labelling and staining techniques to determine the presence of tumour cells, there are also objective methods described in literature, which are based on measuring real tumour related cell properties.

An important tumour diagnostic parameter is the metastatic potential of tumour cells. This parameter can be visualised by investigating cell adhesion properties. The standard way to determine the invasiveness capability of tumour cells is by applying the Boyden chamber method [10]. This filter membrane migration assay uses a chamber consisting of two culture medium filled compartments, separated by a microporous membrane [11]. The cells under investigation are loaded in the first chamber and are stimulated to migrate towards the second chamber filled with culture media and a chemotactic agent. The number of migrated cells is determined by fixing and staining the microporous membrane. Instead of using the elaborate Boyden chamber method Tarantola et al. have realised a real-time invasiveness test biosensor that analyses the dynamic properties of adherent cells electro-acoustically [12]. The sensor principle relies on a quartz crystal microbalance technique, which measures the shift in resonance frequency and damping of an oscillating quartz crystal. When adsorption, desorption, or changes in sample properties close to the quartz surface occur, the crystal detects fluctuations, which indicates the micromotility of cells, revealing collective stochastic motion that can be correlated to the malignancy of the cells. Another method that can determine the adhesion capability of cells was proposed by Chen et al. They investigated the binding capability of suspicious cells to lectin arrays (proteins of non-immune origin that recognize and bind to specific carbohydrate structural epitopes), patterned on a gold substrate [13]. Significant differences were observed in the carbohydrate expression patterns of the different breast tumour cell lines, including changes that correlate with metastatic potential.

Invasive tumour cells have, compared to normal cells, an up-regulation in their glycolysis [14]. This change in cell metabolism can be visualised by using the enzyme lactate-dehydrogenase (EC 1.1.1.27), which can catalyse the conversion of lactate to generate NADH (reduced form of Nicotinamide Adenine Dinucleotide) for sensitive autofluorescence detection. Zheng et al. have designed a biochemical sensor consisting of an optical fibre with lactate-dehydrogenase immobilised on the tip [15]. Experiments on single HeLa, MCF-7, and human fetal osteoblast cells yielded distinctly higher extracellular lactate concentrations than measured for normal cells.

A detection method also using a fibre optical biosensor was presented by Schmidt et al. [16]. Instead of measuring the lactate-dehydrogenase enzyme they designed and realised a detection method for the telomerase activity of suspicious cells/tissues. Telomerase, a ribonucleoprotein complex that is responsible for the maintenance of telomeric DNA at the ends of chromosomes, is involved in cellular immortality and carcinogenesis. In 80 - 90% of malignant tumours telomerase is up-regulated [17], which makes it a potential tumour marker. The task of human telomerase is to extend the guanine-rich strands of the telomere with $(\mathrm{TTAGGG})_\mathrm{n}$. DNA oligos were attached on the surface of the optical fibre. These oligos can be elongated with $(\mathrm{GGTTAG})_\mathrm{n}$ strands when nucleotides and cell extract (containing telomerase) are present. The telomerase activity is visualised by hybridising the elongated strands with complement $(\mathrm{CCAATC})_4$ strands labelled with an FITC fluorescent tag.

A promising label-free method to distinguish tumour cells from normal cells, based on mechanoelastic properties of cells, was investigated by De la Rica et al. [18]. They determined the volume increase of cancer cells under hypo-osmotic pressure by using impedimetric transducers. When cells were experiencing hypo-osmotic stress, they were observed to swell. This volume change of cells could reflect to differentiate tumour cells from non-tumorous cells. The working principle is based on the impedance increase at high frequencies when there is an increase in cell volume bound to the transducer.

Henry et al. have shown that the detection of several key health parameters on a single chip was achievable. They designed and tested a microfluidic chip for the detection of tumour cells by electrochemical impedance spectroscopy [19]. Sensor arrays, consisting of three-electrode cells (gold counter and working electrodes and a silver reference electrode) positioned in microfluidic chambers, were fabricated using standard photolithography and metal deposition technology. The gold working electrodes were functionalised with specific tumour markers, such as carcinoembryonic antigen and prostate-specific antigen, as well as genetic breast cancer markers and short DNA probes to capture the tumour cells.

Another tumour diagnosis method using microfluidics is based on an embedded solenoidal coil, allowing diagnostic NMR measurements (Nuclear Magnetic Resonance). Tumour cells of interest, labelled with magnetic nanoparticles are detected in a sample also containing non-labelled cells by measuring the transverse relaxation. Lee et al. were able to detect down to

2 tumour cells per µL sample of unprocessed fine-needle aspirates [20].

Besides for handling small sample volumes (in the nL - µL scale), microfluidic systems can also play an important role in the sample preparation step. Purifying the sample from contaminants (such as cell debris and bacteria) or separating tumour cells from normal cells in blood or lymph fluid, could increase the efficiency and accuracy of the sensing step.

The research for this thesis was conducted within the European Marie-Curie Research Training Network: On-chip Cell Handling and Analysis "CellCheck". This highly multidisciplinary environment of engineering, biotechnology, medicine, and chip-technology has the potential to successfully investigate, design, and realise new and/or improved diagnostic methods to aid physicians in the diagnosis of suspicious patient tissues. The main goal of this work is focussed on label-free analysis and separation methods for mammalian cells, to aid in the diagnosis of tumour presence.

1.2 Objectives

In the previous section, biochemical sensors as well as physical chemosensors were described, which can be used to determine the presence tumour cells. Physical chemosensor can, compared to chemical sensors, determine chemical and/or biological properties of a sample by performing physical measurements without the need of an chemical active interface [21, 22].

It is known that tumour cells that have the ability to move through the blood or lymph system (metastatic tumour cells) have an altered membrane lipid-protein composition [23], e.g. due to over-expression of the BRCA gene in breast tumour cells [24]. Another membrane alteration found for metastatic tumour cells is the change in plasma membrane bound cholesterol concentration. Schroeder et al. showed that there is a significant difference in molar ratio cholesterol per phospholipid between low and high metastatic mouse melanoma cells (a lower molar cholesterol per phospholipid ratio in high compared to low metastatic melanoma cells) [25].

The research objective is to design and realise new tools to determine the presence of tumour cells in suspicious samples. The three main objectives of this thesis are:

1. to design a novel tumour cell indicator based on the cells physical properties.

2. to design and realise a sensor system allowing the measurement found in the first objective.
3. to design and realise microfluidic devices for the preparation of cell samples.

For the measurements a mid-IR sensor and a dielectrophoresis based separator were designed and realised, that have the potential to be further developed in a point-of-care instrument.

1.3 Outline

In the following chapters, a novel tumour diagnostic method and a highly efficient microfluidic based sample preparation devices are presented. A label-free cell type discrimination method based on changes in the CH_2-symmetric stretch and CH_2-antisymmetric stretch is described in Chapter 2. The CH_2-stretch ratio of cells can be determined by mid-infrared absorbance measurements, normally recorded by infrared spectroscopy. In Chapter 3 a self-designed and realised IR sensor system that allows the determination of IR absorption of cells at the specific wavelengths required to derive the CH_2-stretch ratio is presented. After sensor validation and preliminary CH_2-stretch ratio experiments on epithelial kidney cells, the CH_2-stretch ratio based cell discrimination method was tested on epithelial kidney and melanoma cell lines (Chapter 4). For both tumour types, the CH_2-stretch ratio of a normal cell line is compared with multiple malignant cell lines. Instead of determining the CH_2-stretch ratio of dried cells on IR transparent calcium-fluoride slides, in Chapter 5, a method is investigated that allows measurements of cells suspended in phosphate-buffered-saline. Besides the label-free identification of primary solid tumours, it is also of interest to detect tumour cells that developed the ability to metastasise (invading other organs or other regions of the body by moving through the blood stream or lymph system). To allow IR absorbance measurements on suspended cells, the suspicious cells should first be separated and harvested from body fluids containing contaminants, such as non-viable cells, cell debris, and bacteria. In Chapter 6, the design, realisation, and characterisation of a dielectrophoresis based cell separator are presented. In the final Chapter 7, the main conclusions of the research conducted for this thesis and promising future research possibilities are discussed.

Chapter 2

The CH_2-Stretch Ratio

In this chapter, light interaction aspects on biological samples such as (auto)fluorescence, bio-luminescence, and absorption are summarized (Section 2.1). Absorption of infrared light in the wavelength region between 2 and 20 µm gives insight in the molecular composition of biological cells without the need of additional staining or labelling. By means of IR spectroscopy the CH_2-stretches of lipid acyl chains in the mammalian plasma membrane can be visualized [26].

In Section 2.2 the investigation and realisation of a label-free cell type discrimination method based on the CH_2-stretch ratio is described, specifically for distinguishing tumour cells from normal cells. The cell type discrimination method is based on the ratio changes between the two CH-stretches.

2.1 Introduction

The interaction of light with biological tissues is an effect that can be used for the investigation of disease progression. There are multiple strategies to optically analyse cells. The most common methods are: (auto-)fluorescence (Section 2.1.1) [27,28], bio-luminescence (Section 2.1.2) [29,30], and light absorption (Section 2.1.3) [31, 32]. Some methods require additional labelling or staining to highlight some cellular aspects, such as antibodies on the cell surface or cell viability stains (live cells possessing intact cell membranes exclude certain dyes, such as trypan blue, propidium, and eosin, whereas dead cells do not) [2]. Other techniques require a more sophisticated approach, e.g. green fluorescence protein (GFP) expressing genes by genetic modification, or to investigate viral pathogenesis and effects of anti-viral therapies by recombinant viruses engineered to express a luciferase enzyme (Section 2.1.2).

When cells under investigation are being exposed to light, the corre-

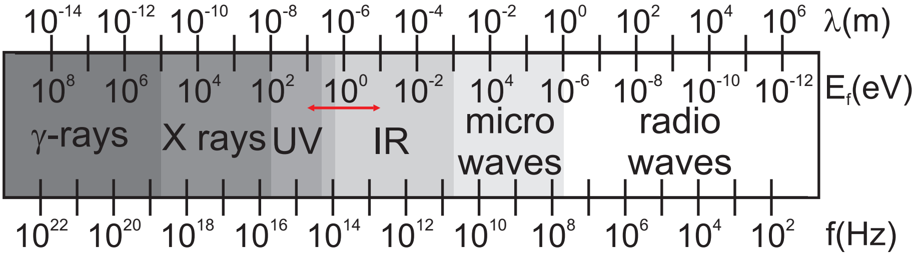

Figure 2.1: Light, electromagnetic radiation spectra with corresponding wavelength, frequency, and single photon energy.

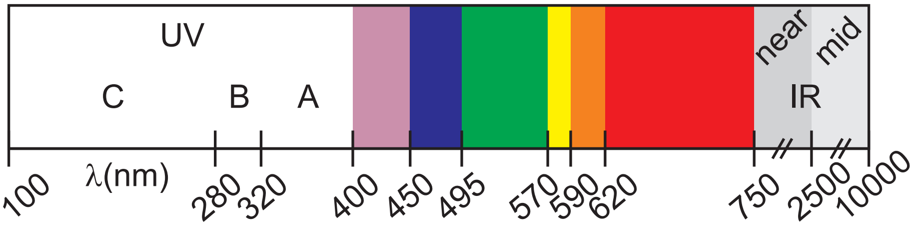

Figure 2.2: UV, visible, and IR spectra.

sponding photon energy could influence, or even harm them. For example, it is known that ultraviolet radiation induces cell damage and apoptosis in the skin [33, 34]. The energy level depends on the wavelength of the used photons. This energy level per photon can be derived by the Planck-Einstein relation (see Eq. and 2.1):

$$E_{\text{photon}} = hf = \frac{hc}{\lambda} \tag{2.1}$$

where E_{photon} is the energy per photon, h the Planck constant, f the frequency of the wave, c the speed of light, and λ the wavelength.

In Fig. 2.1 the electromagnetic radiation spectra with corresponding frequency and single photon energy is depicted [35]. As can be seen, at increasing wavelength the energy of the corresponding photon decreases.

To analyse biological cells, the wavelength regions of interest are: UV, visible, and infrared (depicted in Fig. 2.2).

In Table 2.1 the frequency and energy of single photons at wavelengths in the UV, visible, and infrared spectrum are given.

In the following sections a short overview of fluorescence, luminescence, and light absorption for cell analytical purposes is described.

Table 2.1: The frequency and energy of single photons at wavelengths in the UV, visible, and infrared spectrum.

	λ [nm]	f [THz]	E_{photon} [eV]
UV	260	1153	4.77
red light	650	461	1.91
near IR	1000	300	1.24
mid IR	3505	86	0.35
far IR	25000	12	0.05

2.1.1 (Auto-)Fluorescence

Fluorescence is caused by the absorption of radiation at one wavelength followed by nearly immediate reradiation at a larger wavelength. The emission ceases almost at once when the incident radiation stops. Fluorophores emitting light of a specific wavelength, when being excited at a shorter specific wavelength (see Fig. 2.3), can be bound to biomolecules such as antibodies, mRNA or DNA oligonucleotides, and proteins to visualize enzyme reactions, membranes and lipids, ions, proteins, cell viability, and energy transfer [36, 37].

The excitation and emission maxima of commonly used fluorophores are given in Table 2.2.

An example of fluorescent labelled cells is depicted in Fig. 2.4. As can be seen, the DiO [40] labelled Caki-1 cells can easily be distinguished from non-labelled MDCK cells when being excited at 484 nm. Besides labelling biological cells, there are molecules present in the cells that are auto-fluorescent. A list of endogenous fluorophores is depicted in Table 2.3.

Another method in which fluorescent labels can be used for cell analysis is as reporter (a visible marker). When genes are genetically modified with a vector (a DNA molecule of known nucleotide sequence to be used as a vehicle to transfer foreign genetic material into another cell) containing one or more copies of the coding Green-Fluorescent-Protein (GFP) gene, successful insertions will express the GFP protein emitting bright green light when being exposed to blue or UV light [46]. The GFP gene originates from the jellyfish *Aequoria victoria*. The original GFP gene has been studied and modified to be more stable (reduce photo-bleaching) and fluoresce at different excitation and emission wavelengths [47, 48]. Compared to luciferase

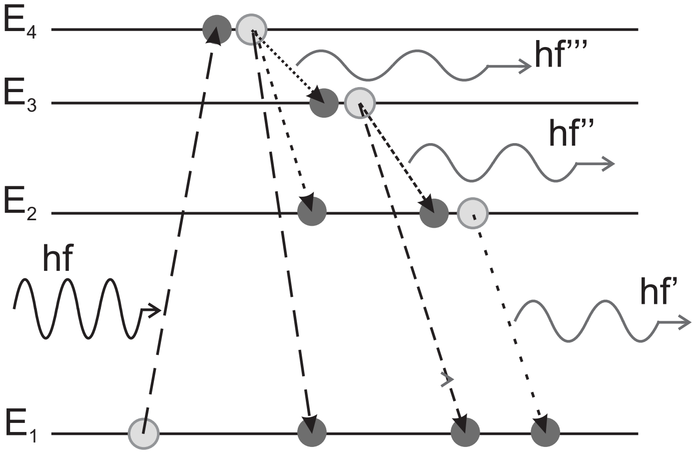

Figure 2.3: Absorption and emission of photons by atoms. When the energy level of an incident photon is great enough to excite an atom to one of its higher excited states, the atom can lose its energy by spontaneous emission as it makes one or more transitions to its lower energy states [35].

Table 2.2: Fluorophores [38, 39].

Fluorophore	Excitation maxima [nm]	Emission maxima [nm]
amplex red	571	585
fluorescein	494	518
eosin	524	544
rhodamine 6G	525	555
X-rhodamine	580	605
rhodamine B	543	565
FITC	495	519
texas red	592	614
Cy-3	548	561
Cy-5	647	665
Cy-7	753	775
DAPI	359	457
DiO	484	501

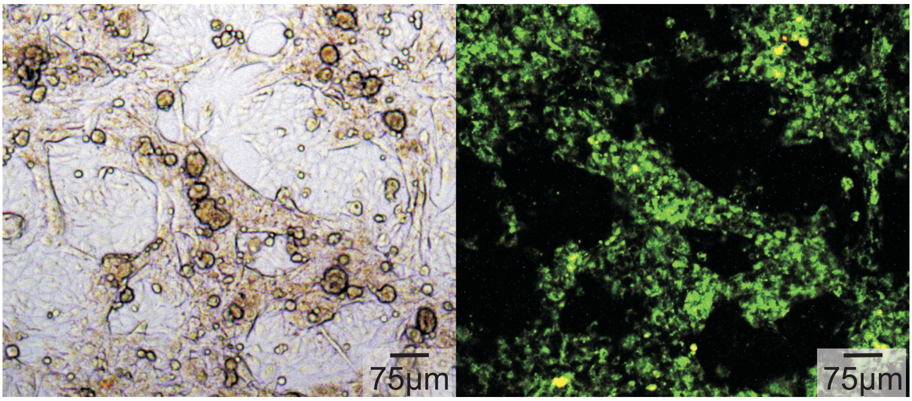

Figure 2.4: A sample slide with a mixture of MDCK and Caki-1 cells. The Caki-1 cells have been stained with the fluorescent viability label DiO prior to mixing with MDCK cells [40]. This label binds to phospholipid bilayer membranes. On the left, a monolayer of MCDK and Caki-1 cells is depicted. On the right, the same field-of-view on the sample slide is shown when being excited at a wavelength of 484 nm, allowing only the Caki-1 cells to fluoresce.

Table 2.3: Endogenous fluorophores at pH 7 [41–45].

Molecule	Excitation maxima [nm]	Emission maxima [nm]
collagen, elastin	325	400
tryptophan	280	350
pyridoxine (Vitamin B6)	332	400
NADH	360	460
FAD	450	515
FMN	445	530
ceroid	350	460
lipofuscin	330 - 390	420, 540 - 560
eosinophils	370	440, 550

(see Section 2.1.2), GFP does not require a substrate to emit light when being excited. Therefore, GFP is an attractive, easy-to-use marker, to aid in assaying cellular processes in real-time [49].

2.1.2 Bio-luminescence

Besides fluorophores, the enzyme luciferase also has proven potential to be used for analysing cells [50]. Luciferase, isolated from the firefly *Photinus pyralis*, catalyses light production. The required substrates are luciferin, ATP, O_2, and magnesium ions [51–55]:

$$\begin{aligned}
\text{luciferin} + \text{ATP} &\overset{\text{ligase} + \text{Mg}^{2+}}{\longleftrightarrow} \text{adenylluciferin} + \text{pyrophosphate} \\
\text{adenylluciferin} + \text{O}_2 &\overset{\text{oxygenase}}{\longrightarrow} \text{peroxyluciferin} + \text{AMP} \\
\text{peroxyluciferin} &\longrightarrow [\text{oxyluciferin}]^* + \text{CO}_2 \\
[\text{oxyluciferin}]^* &\longrightarrow \text{oxyluciferin} + \text{light}
\end{aligned}$$

where $[\text{oxyluciferin}]^*$ is excited oxyluciferin.

The wavelength of the emission peak at pH 7.5 to 8.5 is 560 nm (yellow-green). Besides the firefly *P. pyralis*, there are multiple other species which also emit light by means of bio-luminescence. In Table 2.4 a variety of emission wavelengths are depicted from different marine species [29]. Bio-luminescence can be utilized for dynamic, non-invasive assays of biological processes, such as monitoring genetic modified cells with knocked-out genes when being injected with the substrate luciferin [50].

2.1.3 Light absorption

When light is absorbed by atoms or molecules, the energy of the incoming photons are excited to a higher energy level (Fig. 2.3) [56]. There are three different types of excitation depending on the wavelength of the incoming light. Electrons are excited to higher orbitals by ultraviolet or visible light, vibrations are excited by infrared light (oscillation of the atoms of a molecule), and rotations are excited by microwaves (rotation of the molecule around its centre of mass) [57].

The absorbance of light A by a sample can be defined by the Lambert-Beer Law (see Eq. 2.2).

$$A = log\frac{I_{in}}{I_{out}} = \varepsilon cd \quad \text{with} \quad A = log\frac{1}{T} \tag{2.2}$$

Table 2.4: Bio-luminescent marine species with corresponding emission maxima [29].

Species	Emission maxima [nm]
Scina crassicornis	435
Agalma okeni	444
Photostomias guernei	470
Beroe forskali	491
Umbellula magniflora	501
Plutonaster bifrons	525
Tomopteris nisseni	565
Cyphocaris faurei	595
Malacosteus niger	702

where I_{in} is the incident light intensity, I_{out} the transmitted light intensity, ε the molar extinction coefficient, c the concentration of the sample, d the thickness of the sample cell, and T the transmittance.

In the UV region there are multiple organic molecules absorbing light at specific wavelengths, e.g. purines, pyrimidines, and aromatic amino acids (see Table 2.5).

Infrared absorbance

Instead of exposing biological cell samples to harmful, high energetic UV irradiation to obtain cellular information, the exposure to non-invasive infrared light gives insight to molecular interactions within the cell, such as protein and lipid composition. Infrared spectroscopy, the frequency depended absorbance of infrared light due to specific molecular vibrations, is a proven technique for detecting molecular changes in mammalian cells without the need of additional labels or staining dyes [26, 60–63]. The IR spectrum of biological samples can be recorded between wavelengths 2 and 20 µm with an IR spectrophotometer. Special software packages with baseline correction and normalization functions allow the comparison of different samples.

The oscillation frequency due to the vibrations of a diatomic molecule can be described by Hooke's law of simple harmonic motion [35, 64, 65].

Table 2.5: Molar extinction coefficient of absorbed UV light by organic molecules at pH 7 [58, 59].

Molecule	optimum absorbance wavelength [nm]	molar extinction coefficient [liter mol^{-1} cm^{-1}]
tryptophan	278	5579
tyrosine	274	1405
phenylalanine	258	195
histidine	211	5700
thymine	267	9600
cytosine	271	9100
alanine	260	14500
guanine	253	13600
uracil	262	10000

This vibration frequency (see equation 2.3) can be related to the force exerted by one atom on the other (Fig. 2.5).

$$\omega = \sqrt{\frac{k}{m_{\mathrm{r}}}} \Rightarrow 2\pi f = \sqrt{\frac{k}{m_r}} \tag{2.3}$$

where ω is the angular frequency in [1/s], k the effective bond force constant in [N/m], and m_r the reduced mass (value of a hypothetical mass introduced to simplify the mathematical description of motion in a vibrating or rotating two-body system) with atomic masses $m1$ and $m2$:

$$m_{\mathrm{r}} = \frac{m1 \times m2}{m1 + m2} \tag{2.4}$$

The frequency $\overline{v}$ in wavenumbers [cm^{-1}] (equal to the reciprocal of the wavelength λ in [cm]) of the vibration between two bonded atoms is given by:

$$\overline{v} = \frac{1}{2\pi c}\sqrt{\frac{k}{m_{\mathrm{r}}}} \tag{2.5}$$

where c is the speed of light in [cm/s].

Compared to a spring, which can be stretched and be compressed freely, a molecular bond can break and has a limit to which it can be compressed.

Figure 2.5: The molecular bond between two atoms $m1$ and $m2$ can be represented as a spring.

Table 2.6: The three main vibrational modes of water vapour with corresponding wavenumber, wavelength, frequency, and energy level [67].

Main vibrations of water	wavelength [µm]	frequency [THz]	vibration energy [eV]
ν_{as} antisymmetric stretch	2.66	113	0.47
ν_s symmetric stretch	2.73	110	0.45
ν_b bending	6.27	48	0.20

This means that the molecular bond behaves more like an anharmonic oscillator (not oscillating in simple harmonic motion) [66]. Infrared absorption techniques under normal temperature condition only depends on the excitation of the electronic ground state levels of vibrational and rotational energy levels. For absorbance due to molecular vibrations, the energy between two vibrational states can be derived by the Schrödinger's equation of simple harmonic oscillations (Eq. 2.6):

$$E_\nu = (\nu + \frac{1}{2})hf \quad \text{with} \quad \nu = 0, 1, 2, ... \tag{2.6}$$

where E_ν is the energy level of vibration state ν, h the Planck constant, and f the frequency of vibration. The energy difference between two vibration states is:

$$E_{\nu+1} - E_\nu = (\nu + 1 + \frac{1}{2})hf - (\nu + \frac{1}{2})hf = hf \tag{2.7}$$

Water has three main vibrational modes: bending, symmetric stretch, and antisymmetric stretch. The corresponding frequency and energy level of vibration are given in Table 2.6. A schematic representation of the vibrational modes water are depicted in Fig. 2.6.

Besides detecting specific molecular vibrations of water, many biological relevant vibrations can be investigated by means of IR absorbance, This

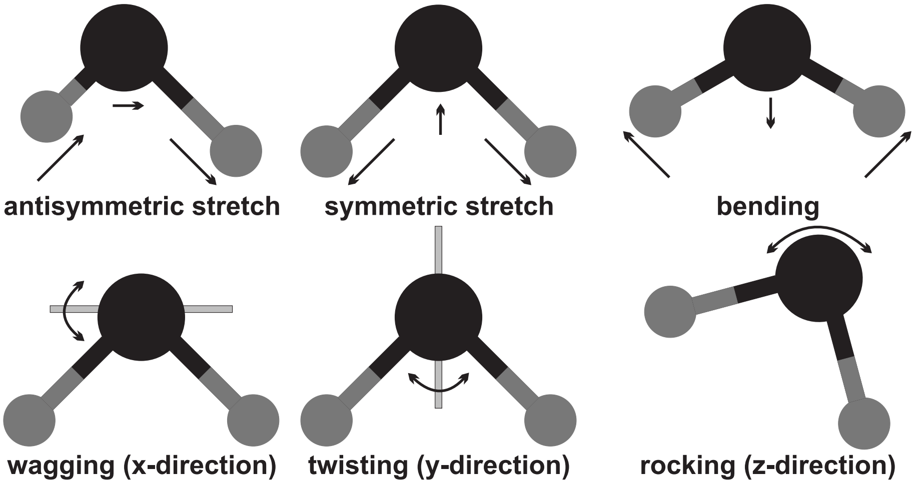

Figure 2.6: The main vibrational modes of water. The oxygen atom is depicted in black and the hydrogen atoms in grey. The vibrational modes are: antisymmetric stretch, symmetric stretch, bending, and liberations in the direction of the x, y, and z-axis. The dipole moments change in the direction of the movement of the black atoms as depicted by the arrows.

makes IR spectroscopy a very attractive detection tool for label-free, objective cell investigations. In Table 2.7, biological relevant specific molecular vibrations with corresponding wavenumber and wavelength are given.

In the following Section (2.2) a label-free cell type discrimination method based on the CH_2-symmetric and CH_2-antisymmetric stretch is proposed.

2.2 The CH_2-stretch ratio cell discrimination method

By comparing the infrared absorbance spectra of normal and malignant cells, which were published in literature (see Table 2.8), a new measurement method to distinguish normal from malignant cell types is hypothesized. It concerns a four-wavelength, mid-infrared absorbance measurement of specific lipid absorbance peaks to derive the CH_2-symmetric and CH_2-antisymmetric stretches of suspicious cells and/or tissues.

The CH_2 and CH_3-stretches derived from published IR absorption spectra of different clinical human tumour samples versus their normal cell type,

Table 2.7: Mid infrared absorption bands of membrane proteins and lipids [26] [68].

Functional group	assignment	wavenumber [cm^{-1}]	wavelength [μm]
CH_3	antisymmetric stretch	2956	3.38
CH_2	antisymmetric stretch	2920	3.42
CH_3	symmetric stretch	2870	3.48
CH_2	symmetric stretch	2850	3.51
C=O (ester)	stretch	1730	5.78
C=O, C=N-C	stretch, vibration	1690 - 1620	5.92 - 6.17
COO^-	antisymmetric stretch	1623	6.16
N-H	bending	1570 - 1530	6.37 - 6.54
O-P=O	antisymmetric stretch	1228	8.14
-CO-O-C	antisymmetric stretch	1173	8.53
O-P=O	symmetric stretch	1085	9.22
-CO-O-C	symmetric stretch	1063	9.41

Table 2.8: CH_2 and CH_3-symmetric and antisymmetric stretch changes of different human cell types derived from infrared spectra published in literature. The first three types are normal versus malignant cells, the last two are benign versus malignant tumours, and the last are non-resistive versus resistive melanoma cells. (All spectra were baseline corrected through base points at 2800 and 3000 cm^{-1}, and normalized to the CH_2-antisymmetric stretch peak at 2920 cm^{-1}).

Malignant cell type	CH_2 υ_{symm} 2850 cm^{-1}	CH_3 υ_{symm} 2870 cm^{-1}	CH_3 υ_{asymm} 2956 cm^{-1}
colorectal cells [69]	increase	decrease	decrease
oesophagus cells [70]	increase	decrease	decrease
breast tissue [71]	increase	decrease	decrease
breast tissue [72]	increase	increase	decrease
melanocytes [73]	increase	decrease	decrease

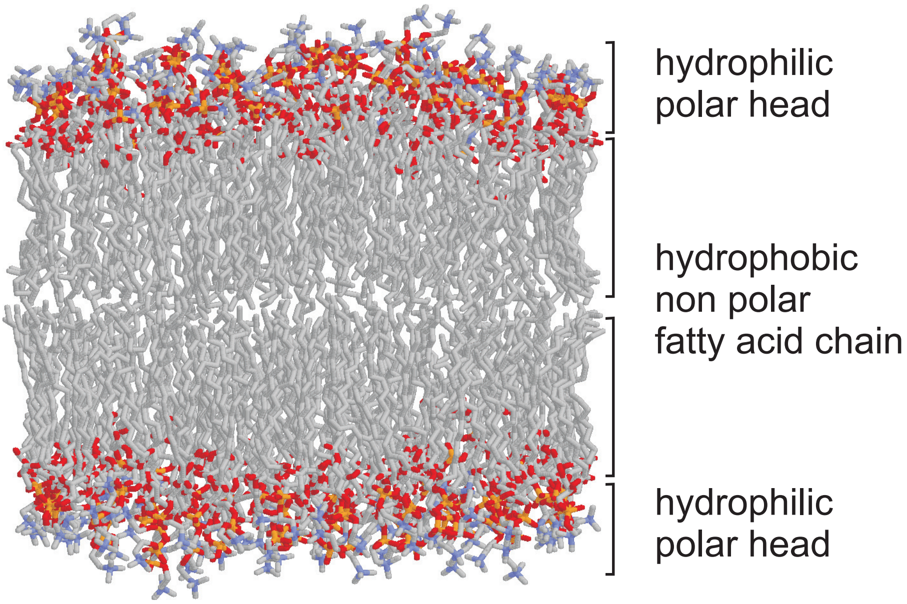

Figure 2.7: Schematic representation of a phospholipid bilayer. (pdb data adapted from reference [75]).

show an increase in CH_2-symmetric stretch IR absorption and a decrease in CH_3-antisymmetric stretch IR absorption. For example, CH_2 and CH_3-stretch differences were found in tissue sections of human colorectal cancer compared to histologically normal mucosa [69], malignant versus normal oesophageal tissue [70], pathological breast tissue compared to connective tissue [71], malignant versus benign fibroadenoma breast tissue [72], and cisplatin-resistant versus non-resistant melanoma cell lines [73].

Mammalian cell membranes (Fig. 2.7) are composed of three main classes of lipid molecules: phospholipids, cholesterol, and glycolipids. The four most commonly found phospholipids in the plasma membrane are: phosphatidylcholine (Fig. 2.8), sphingomyelin, phosphatidylserine, and phosphatidylethanolamine [74]. They consist of a hydrophilic head and a hydrophobic, fatty-acid, carbon-hydrogen based tail.

As far as we know the molecular mechanism that leads to a change in lipid CH_2-symmetric stretch and CH_2-antisymmetric stretch is unknown, but it is clear that during tumour formation changes in the cell membrane occur (e.g. over-expression of genes such as HER-2 in breast tumours, which encodes a cell membrane located growth factor receptor [76]; changes in

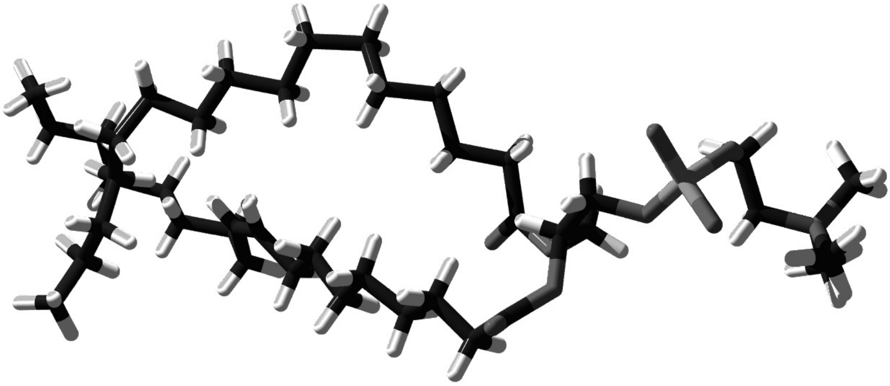

Figure 2.8: Drawing of a phosphatidylcholine molecule consisting of two alkane chains. The Alkane chains are polymers of CH_2 monomers. The white sticks represent the hydrogen atoms, the black sticks the carbon atoms, and the grey sticks nitrogen, oxygen, or sulpher atoms (pdb data adapted from reference [75]).

composition of integrin, a membrane molecule responsible for cell-cell adhesion to induce cell metastasis [74]).

Mammalian plasma membranes of normal cells consist of about 20 - 25% lipid mass cholesterol [77], which is the most important substance of the three membrane lipid molecule classes influencing the conformation of the fatty-acid alkane chains.

The CH_2-stretch ratio as label-free indicator for tumour detection is a strong concept. Instead of comparing differences in molecular composition, such as the lipid-to-protein ratio or CH_2 versus CH_3 amount, the CH_2-stretch ratio cell discrimination method compares the interaction of CH_2-chains with infrared light at specific wavelengths. We postulate that the increased CH_2-stretch ratio, CH_2-symmetric stretch / CH_2-antisymmetric stretch, of tumour cells compared to normal cells is caused by a reduction or reallocation of membrane stabilizing agents such as cholesterol. Supporting evidence was found in publications by Cai et al. and Guyot-Sionnest et al. They showed that after over-expressing caveolin-1 in the plasma membrane of doxorubicin-resistant breast cancer cells (Hs578T) the cholesterol level decreases with 30% [78]. By sum-frequency vibrational spectroscopy of a Langmuir film, it is shown that when straightening up a pentadecanoic acid molecule the CH_2-symmetric peak decreases [79].

This “disorder” in the lipid membrane of cells can be visualized by the CH_2-symmetric / CH_2-antisymmetric stretch ratio. Changes in CH_2-stretch

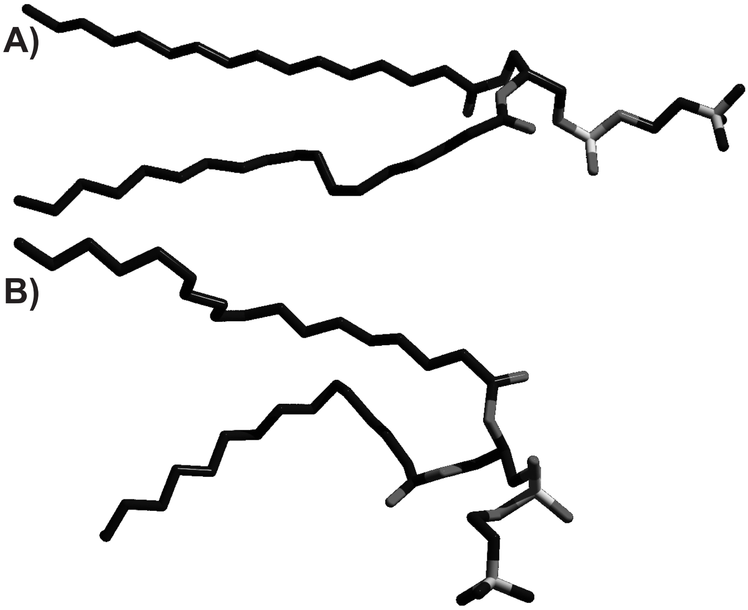

Figure 2.9: Conformation of a phosphatidylcholine phospholipid in **A)** crystal and **C)** in liquid form. When a lipid becomes more disordered, it occupies a larger area. (pdb data file used from reference [75]).

ratio are based on the chain conformation of alkane chains in the membrane lipid layer. The more a chain is disordered, resulting in kinks and twists, the higher the CH_2-symmetric stretch absorbance. A more disordered chain also results in a higher area per molecule [79] (see Fig. 2.9).

The difference between CH_2-symmetric and CH_2-antisymmetric stretch exists due to bond dissociation energy (bond enthalpy at room temperature) differences between carbon and hydrogen atoms [80]. When the acyl chain is stabilized, e.g. the carbon backbone of phospholipids stretched by cholesterol (see Fig. 2.13), the vibration is CH_2-symmetric stretch. The effective bonding forces between the carbon and hydrogen atoms of both symmetric and antisymmetric stretches can be derived from introducing their respective wavenumber frequencies, found in literature [62], in equation 2.4 and 2.5. In Fig. 2.10, Table 2.9, and Table 2.10 the force constant, bond length, and dissociation bond energy influenced by the carbon-hydrogen bond of single, double, and triple bond carbon-carbon molecules are given.

At increasing bond energy levels the vibration frequency (in wavenumbers) increases. Table 2.10 shows that the carbon-hydrogen

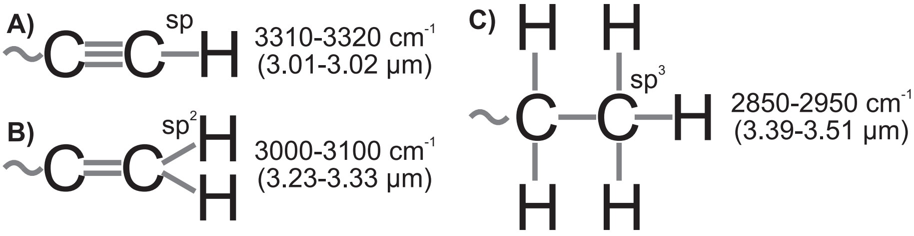

Figure 2.10: Stretching vibrations of a bond between C-H molecules with **A)** sp, **B)** sp^2, and **C)** sp^3-hybridized carbon.

Table 2.9: C-H stretch absorption bands with their corresponding frequency and relative force constant. (υ_{symm} is symmetric stretch and υ_{asymm} is antisymmetric stretch).

Functional group	wavenumber [cm^{-1}]	frequency [THz]	force constant [N/m]
-CH_2 υ_{symm}	2850	85.4	445
-CH_3 υ_{symm}	2870	86.0	451
-CH_2 υ_{asymm}	2920	87.5	467
-CH_3 υ_{asymm}	2956	88.6	479
=CH_2	3010	90.2	496
≡CH	3315	99.4	602

Table 2.10: The bond length and energy of different carbon-carbon and carbon-hydrogen conformations [80,81]. The bond energies given between brackets correspond for hypothetical single bonds. The bond energies between carbon-hydrogen are higher compared to their sp* carbon-carbon bonds.

Functional group	bond length [pm]	bond dissociation energy [kJ/mol]
$\mathbf{C}$-$\mathbf{C}$ (sp^3)	154	368
$CH_3CH_2\mathbf{CH_2}$-$\mathbf{H}$ (sp^3)	110	410
$\mathbf{C}$=$\mathbf{C}$ (sp^2)	134	607 (304)
CH_3CH=CH-$\mathbf{H}$ (sp^2)	108	452
$\mathbf{C}\equiv\mathbf{C}$ (sp)	121	795 (265)
$CH_3C\equiv\mathbf{C}$-$\mathbf{H}$ (sp)	106	523
$\mathbf{CH_3}$-$\mathbf{H}$	-	439
$CH_3\mathbf{CH_2}$-$\mathbf{H}$	-	423
$CH_3CH_2\mathbf{CH_2}$-$\mathbf{H}$	-	414
$CH_3CH_2CH_2\mathbf{CH_2}$-$\mathbf{H}$	-	406

bond energies of alkanes decrease with increasing substitution: $\mathbf{C}H_3$-$\mathbf{H}$ $>$ $CH_3\mathbf{CH_2}$-$\mathbf{H}$ $>$ $CH_3CH_2\mathbf{CH_2}$-$\mathbf{H}$ $>$ $CH_3CH_2CH_2\mathbf{CH_2}$-$\mathbf{H}$, respectively: $439 > 423 > 414 > 406$ kJ/mol. This means that at increasing CH_2 substitution the bond length between the carbon and hydrogen atoms increases and, therefore, a decrease in electron pulling force between the two atom. Similarly, increased hybridization of the carbon centres increases the carbon-hydrogen bond energy as: sp $>$ sp^2 $>$ sp^3, respectively: $523 > 452 > 410$ kJ/mol [80,81].

All bond dissociation energies given above are of pure gases. When mixed with other gases, these values change due to molecular interactions. The bonding force strength between carbon-hydrogen of the CH_2-antisymmetric stretch vibration is stronger compared to that of the CH_2-symmetric stretch (respectively, 467 and 445 N/m. See Table 2.9). A stronger bond between the carbon-hydrogen atoms results in a shorter distance between the two atoms.

By stretching the “carbon-carbon” chain, the distance between the carbon atoms increases (larger bond lengths), resulting in a decrease of the electron pulling force by the protons between the carbon atoms. Under the same circumstances, the effective bond strength between the “hydrogen

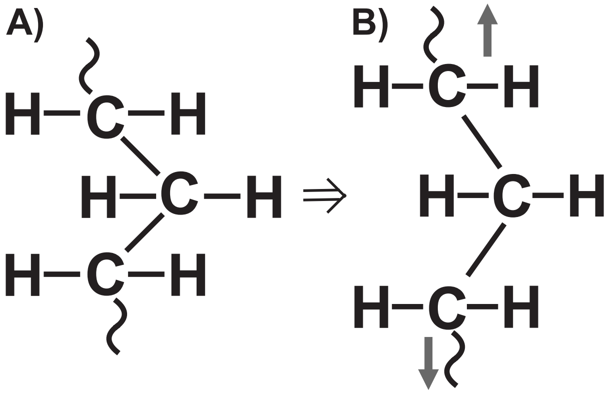

Figure 2.11: Stretching the carbon chain increases the distance between the carbon atoms. **A)** relaxed and **B)** stretched alkane chain.

and carbon" atoms increases (smaller bond length) and the effective pulling force of the hydrogen proton on the electron bond between hydrogen and carbon is increased. At a low effective bonding force, the hydrogen atoms move symmetrically away or towards the carbon atom, allowing symmetric stretch. An increase in effective bonding force, on the other hand, only allows antisymmetric movement of the hydrogen atoms in respect to the carbon atom (see Fig. 2.11 and 2.12 for a more detailed explanation). When the carbon backbone is less stretched, allowing more kinks and twists, the distance between the carbon atoms is decreased (larger bonding force) and the carbon-hydrogen bond distance is increased (lowering the bonding force). The amount of CH_2 of the acyl chain stretching antisymmetrically is then reduced and the amount of CH_2 stretching symmetrically increased (resulting in an increase in CH_2-symmetric / CH_2-antisymmetric stretch ratio).

Table 2.10 also shows that the bond energy between an sp^3 carbon-hydrogen (410 kJ/mol) is larger than that of an sp^3 carbon-carbon bond (368 kJ/mol). When a carbon-carbon bond is replaced by a carbon-hydrogen bond, the average bonding force between all carbon-hydrogen bonds are increased due to this increased bonding energy, resulting in that the CH_3-stretch peaks appear at higher wavenumbers than that of their corresponding CH_2-stretches.

The previously mentioned stretching of the carbon-hydrogen chains in the mammalian plasma membrane is, in real life, affected by hydrophobic interactions, hydrogen bonding between glycerolipids and cholesterol, and Van der Waals forces between membrane molecules [82, 83]. Cholesterol

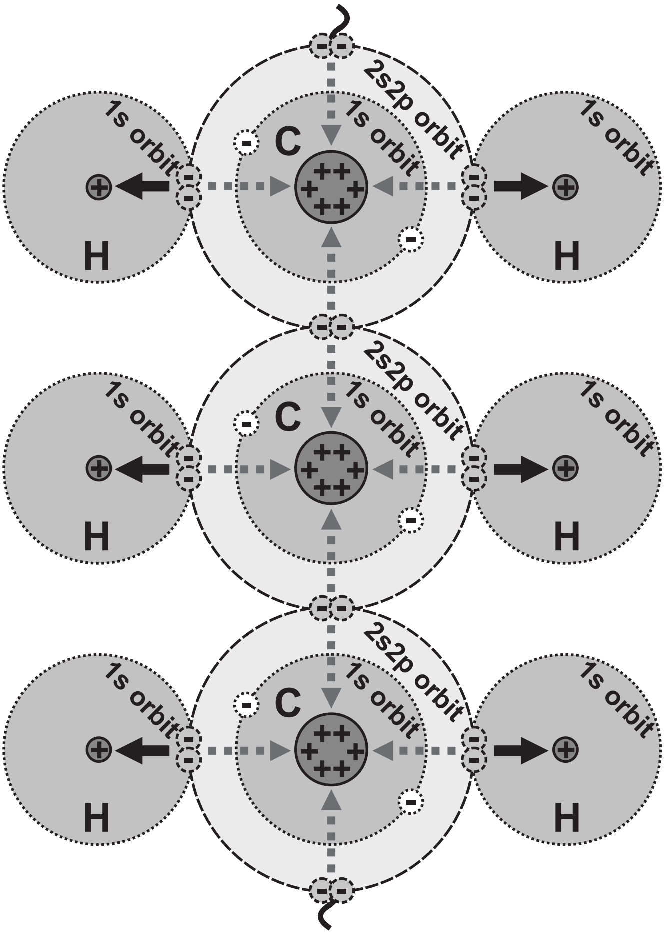

Figure 2.12: A simplified schematic representation of a small part of a fatty acid chain. Of each atom, carbon and hydrogen, the electron orbits and protons in the nucleus are depicted. The arrows represent the bonding force between the atoms. An increase in CH_2-antisymmetric stretch and reduction in CH_2-symmetric stretch (so a decrease in the CH_2-symmetric / CH_2-antisymmetric stretch ratio) occurs when the carbon backbone chain is more stretched. Here, the distance between the carbon atoms is increased, which results in a smaller bonding force due to an increased distance between the protons in the carbon nucleus and the electrons in the 2s2p shell. At the same time, the distance between the carbon and hydrogen atoms decreases, resulting in a larger bonding force. Due to the higher carbon-hydrogen bonding force, the preferred vibration is anti-symmetrical.

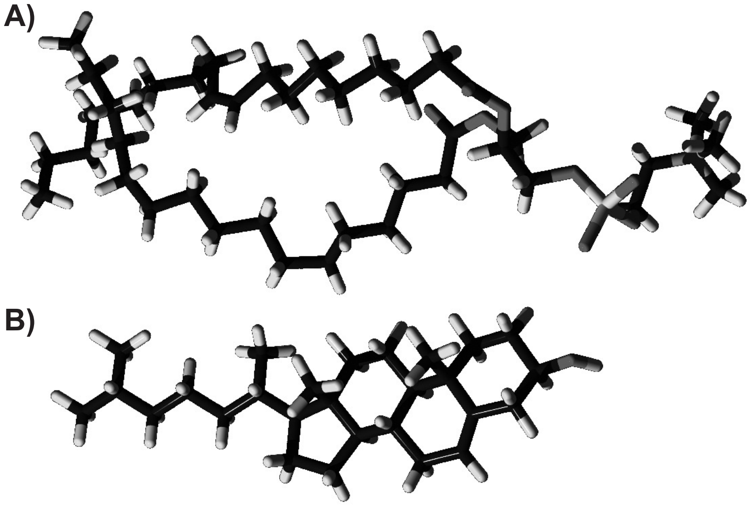

Figure 2.13: Cholesterol has a condensation effect on the lipid bilayer. **A)** phosphatidylcholine **B)** cholesterol.

plays an important role in stabilizing the alkane chain and regulating membrane protein interactions and activity (see Fig. 2.13) [84–87]. It reduces the mean molecular area [77], decreasing the CH_2-symmetric stretch peak and, therefore, decreasing the CH_2-stretch ratio.

Besides the CH_2-symmetric to CH_2-antisymmetric IR absorbance peak shift (when stretching the lipid chains), there are also small wavelength absorbance peak shifts due to chain rotation configurations. In the Figures 2.14, and 2.15 the energy levels and conformations of butane (C_4H_{10}, an alkane consisting of CH_2) are given as example. The most stable chain conformation is the one where the largest substituents of the carbon-carbon chain are located anti (trans) to each other (Fig. 2.14D) [81].

To test the label-free cell type discrimination method based on the CH_2-stretch ratio, the IR absorbance of two epithelial kidney cell lines MDCK (normal) and Caki-1 (carcinoma) have been recorded with a Bruker Equinox 55 infrared spectroscope and compared (240 scans per spectrum, 4 cm^{-1} resolution, and 1 mm beam diameter). The IR absorbance recordings were made in cooperation with Prof. B. Lendl and Dr. S. Armenta-Estrela, Institute of Chemical Technologies and Analytics, Vienna University of Technology. Standard baseline correction and normalization scripts were used in order to allow comparison between the IR absorbance spectra of the two kidney cell lines. Significant differences in the IR absorbance

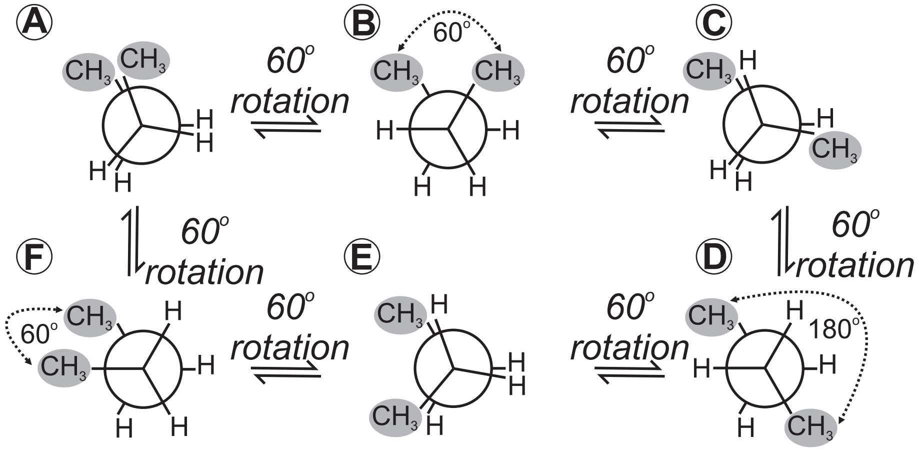

Figure 2.14: Newman projections of the different conformations of butane. **A)**, **B)**, and **F)** gauche conformation, **C)** and **E)** eclipsed (less stable), and **D)**, the most stable conformation where the largest distance between the two CH$_2$ substituents is reached.

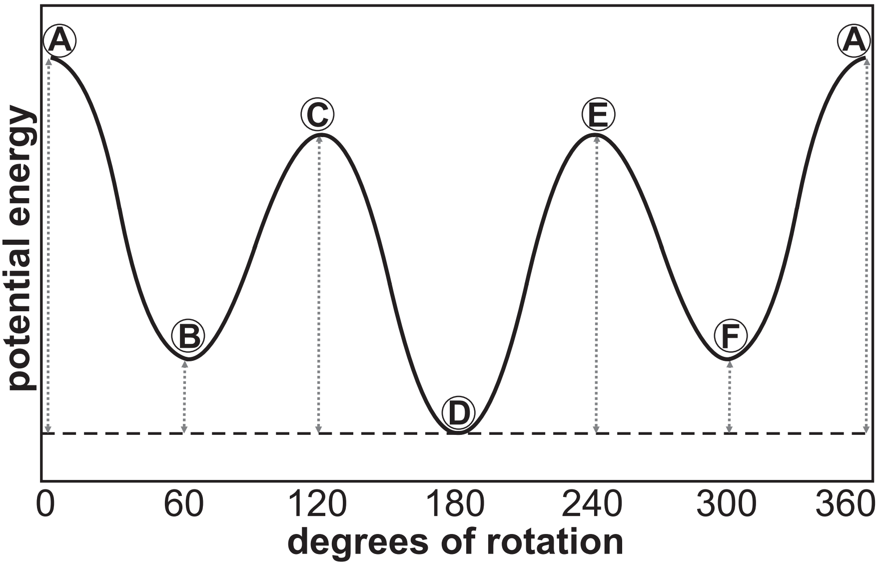

Figure 2.15: Energy diagram of the different conformations of butane.

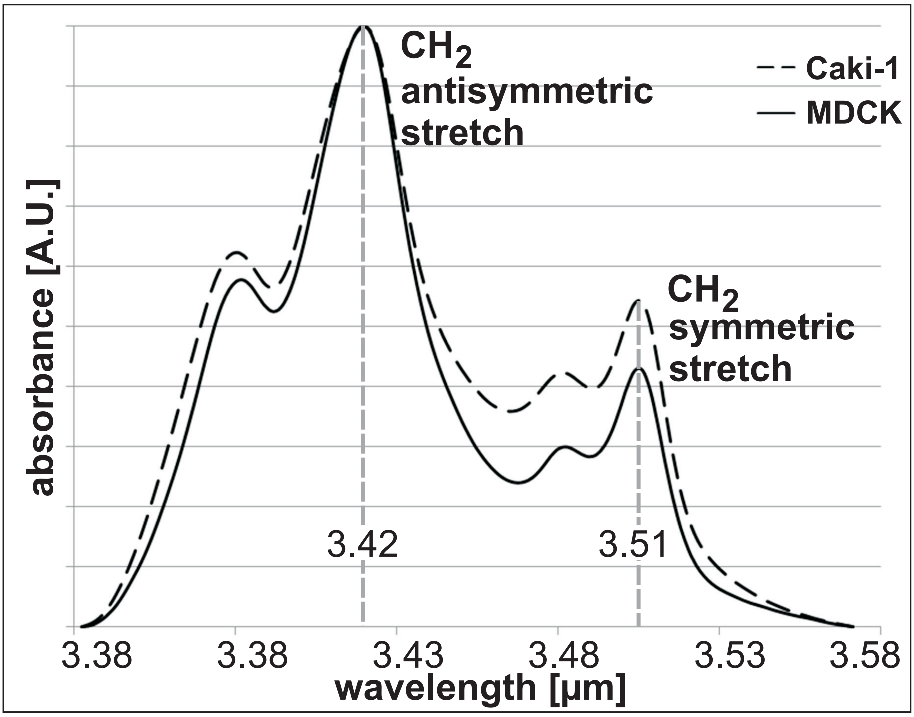

Figure 2.16: Normalized and baseline corrected IR absorbance spectra of normal MDCK and carcinoma Caki-1 epithelial kidney cells, recorded with a Bruker Equinox 55 spectrometer (240 scans per spectrum, 4 cm^{-1} resolution, and 1 mm beam diameter). The intensity of the CH_2-symmetric stretch peak at 3.51 µm of Caki-1 carcinoma cells is higher compared to that of the normal MDCK cells.

ratio CH_2-symmetric / CH_2-antisymmetric stretch (3.51 / 3.42 µm) between the two cell lines were detected. This ratio is higher in the carcinoma cell line compared to the normal cell line (Fig. 2.16).

In the following chapter (CH. 3) the design and realisation of the four-wavelength mid-infrared sensor system are described as well as first measurement results of a normal and malignant epithelial kidney cell line.

Chapter 3

Sensor Design and Technology

In this chapter, a self-designed and realised IR sensor system that allows the determination of IR absorption of cells at the specific wavelengths required to derive the CH_2-stretch ratio is shown. This section also comprises sensor validation measurements of yeast (an easy to handle sample also consisting of CH_2 chains but does not require elaborate cultivation), which are compared to absorbance spectra obtained by FTIR spectroscopy.

3.1 Introduction

In recent years, cancer has become the number one disease of death causes [88]. Tumour screening, the detection and identification of possible carcinoma cells, plays an important role in understanding the fundamentals of tumour development and in selecting the proper treatment. When suspicious tissue is detected, e.g. by mammography or magnetic resonance imaging (MRI) [89], biopsy cell type identification can be done by visual inspection of slides with labelled or stained cells. These labelling and staining techniques are expensive and require time consuming visual inspection, which can only be performed by highly trained personnel and also results in false positives and negatives (e.g. for cervical tumour screening the inter-observer reproducibility is very low [3]).

IR absorbance spectra recordings of normal (MDCK) and malignant (Caki-1) epithelial kidney cells with a conventional IR spectroscope showed significant differences in the absorbance ratio 3.51 µm / 3.42 µm (CH_2-symmetric / CH_2-antisymmetric stretch, see Fig. 2.16 Chapter 2.2). However, for the determination of the CH_2-stretch ratio of biological samples, it is sufficient to measure the IR absorption at four specific wavelengths. Therefore, instead of recording the whole IR absorbance spectrum with an expensive liquid nitrogen cooled IR spectroscope to distinguish normal from malignant cells or tissue samples, a LED-photodiode based mid-infrared absorption sensor, operating at four specific wavelengths has been designed and realised. This strategy should allow the realisation of point-of-care instrumentation. Compared to common techniques, this method does not require specific labelling or staining. The sensing principle is based on a "quadruple infrared wavelength" measurement to derive the CH_2-symmetric / CH_2-antisymmetric stretch ratio. This is realised by mid-infrared emitting LEDs, a photodiode, and narrow band pass filters [90, 91]. Two of the four wavelengths, 3.33 and 3.57 µm, are used as reference points. The other two wavelengths are specific for CH_2-symmetric and CH_2-antisymmetric stretch absorption (respectively at 3.51 and 3.42 µm).

3.2 Materials and methods

3.2.1 Cell lines and sample preparation

In order to investigate the feasibility to distinguish normal from malignant cell types by comparing their CH_2-symmetric / CH_2-antisymmetric stretch ratio, the IR absorbance spectra of a epithelial kidney cell lines were recorded with a conventional IR spectroscope. The investigated cell lines were normal Madin-Darby Canine Kidney (MDCK, ATCC CCL-34) and human carcinoma Caki-1 (ATCC HTB-46). Both cell lines were cultivated under the same conditions in monolayer on IR transparent calcium-fluoride slides at 37°C and 5% CO_2. The culture medium consists of Dulbecco's Modified Eagle Medium (DMEM), 2 mM L-glutamine, 10% FCS (fetal calf serum), and antibiotics (100 units/mL penicillin, 100 µg/mL streptomycin, and 0.25 µg/mL Amphotericin B), all obtained from Lonza Bioscience. Before measuring the IR absorbance, the sample slides were washed with 37°C PBS (phosphate buffered saline) to remove detached cells and medium components. In Fig. 3.1, monolayers of different dried kidney cell spots are depicted. The results obtained from spectroscopic measurements of the two kidney cell types (Fig. 2.16) confirmed the normal from malignant cell type discrimination hypothesis and was the basis to develop a quadruple-wavelength IR sensor system. To validate the sensor system and to make a first comparison to spectroscopic recordings we prepared yeast samples. Yeast also contains the CH_2-symmetric and CH_2-antisymmetric stretch bands, but is also much easier to prepare without the need of cell cultivation. Dried grains of yeast were dissolved in PBS and 4 µL were pipetted on a calcium-fluoride slide. To remove the water fraction, the investigated

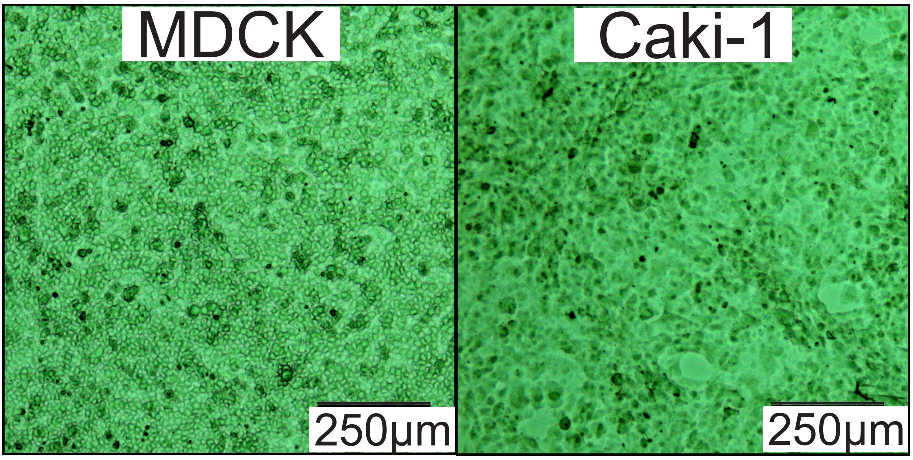

Figure 3.1: Dried normal (MDCK) and carcinoma (A-498 and Caki-1) epithelial kidney cells grown attached as monolayers on infrared transparent calcium-fluoride slides.

samples were dried for four hours in a sterile laminar flow cabinet. For sensor CH_2-stretch measurements on normal and malignant kidney cells we used the same sample preparation protocol as used for the spectroscopic measurements.

3.2.2 Detection method

The IR absorbance ratio between CH_2-symmetric and CH_2-antisymmetric stretch can be determined by a “quadruple wavelength” infrared absorbance measurement (Fig. 3.3). Due to baseline artefacts such as variations in sample thickness and water concentration, care must be taken to derive the proper data out of the recorded signals. To compare the CH_2-stretch ratio of different samples, baseline correction and normalization is required. The IR absorbance spectra of biological cells show an IR absorbance minimum at 3.33 µm (3000 cm^{-1}) and an “empty area” in the wavelength region between 3.57 - 4.00 µm (2500 - 2800 cm^{-1}), (see Fig. 3.2).

The selected reference points to derive the baseline are the IR absorbance values at 3.33 and 3.57 µm (3000 - 2800 cm^{-1}). As a result, the non-functional absorbance values under the baseline can be calculated and subtracted from the total absorbance signal, resulting in the functional values at 3.42 and 3.51 µm. By dividing the functional absorbance value from the CH_2-symmetric stretch (3.51 µm) with the CH_2-antisymmetric stretch

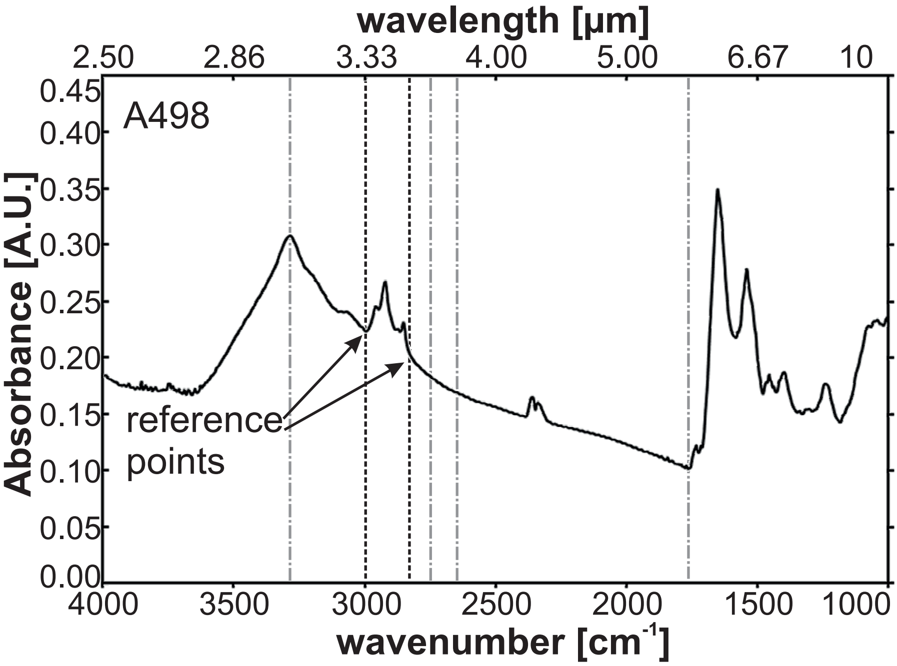

Figure 3.2: IR absorbance spectra of A498 cells in the wavelength range between 2.5 and 10 µm recorded with a Bruker Equinox IR spectrometer (240 scans per spectrum, 4 cm^{-1} resolution, and 1 mm beam diameter). The reference points selected for the determination of the CH_2-stretch ratio are marked with arrows.

band (3.42 µm), the normalized ratio will be obtained, which makes sample comparison possible even when different amounts of cells are being investigated.

By selecting a different baseline procedure, for example a linear baseline through reference points 3.33 µm (3000 cm^{-1}) and 3.77 µm (2650 cm^{-1}) instead of 3.33 µm (3000 cm^{-1}) and 3.57 µm (2805 cm^{-1}), the values of the CH_2-stretch ratio of a typical measurement increases a few percent. Also when a polynomial between 3.05 µm (3280 cm^{-1}) and 5.68 µm (1760 cm^{-1}) following the baseline is selected as baseline, the CH_2-stretch ratio increases a few percent. For the data set depicted in Fig. 3.2 this CH_2-stretch ratio increase is 2.8%. However, because this is valid for the normal and tumour cells the influence on the CH_2-stretch ratio is very small (normally less than a few percent). All the described baseline procedures can be successfully used to determine the CH_2-stretch ratio for the discrimination of tumour cells from normal cells. The linear baseline through reference points

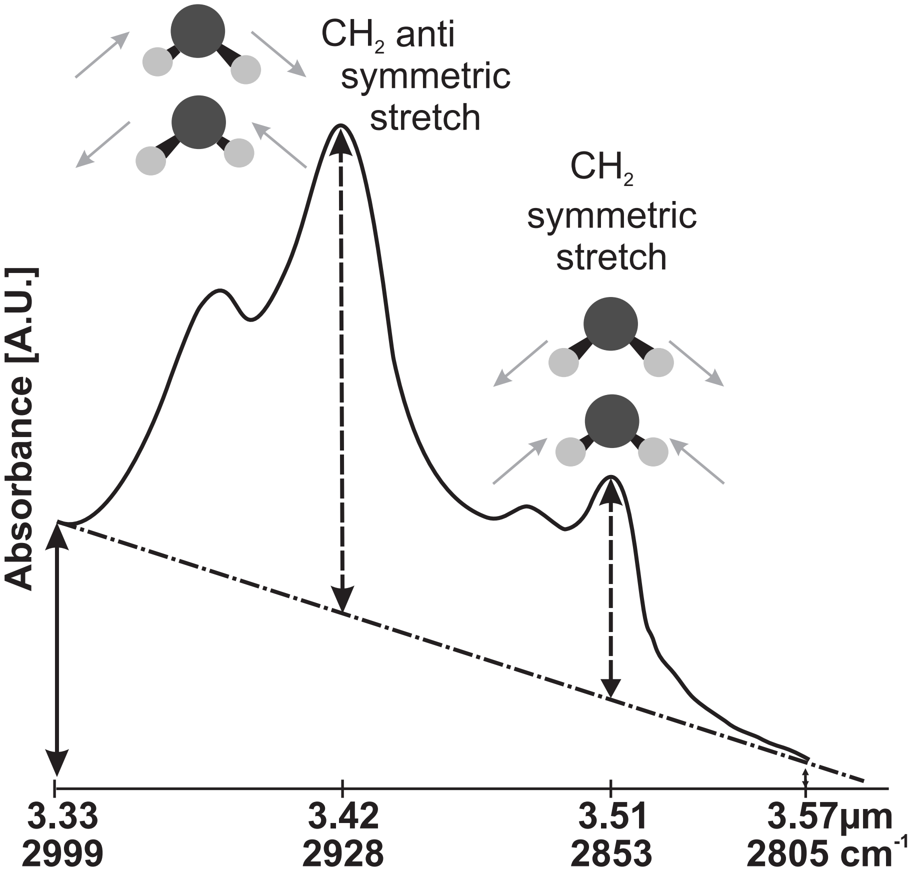

Figure 3.3: CH_2-stretch ratio detection method. To evaluate the CH_2-stretch ratios of different samples base line correction is required. The absorbance values at 3.33 and 3.57 µm (solid arrows), are used to determine the base line. As a result, the functional absorbance values of 3.51 and 3.42 µm (dashed arrows), can be calculated. By dividing the functional absorbance values, 3.51 / 3.42 µm, the normalized CH_2-stretch ratio will be obtained that can be used for sample comparison.

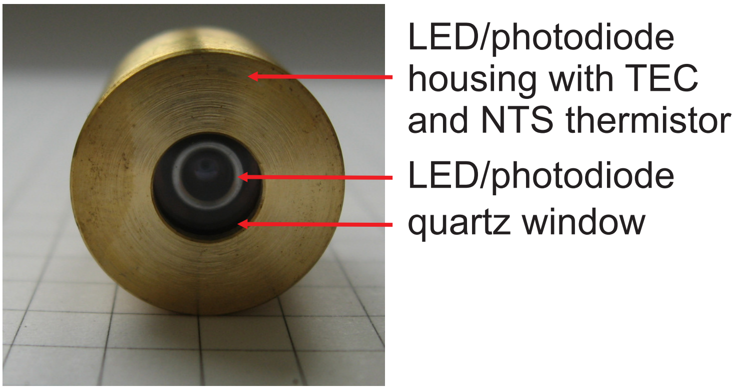

Figure 3.4: Photo of a 3.34 µm wavelength LED, fabricated from III-V heterostructures grown onto InAs substrates. The LEDs and PD contain an immersion silicon lens to optimize the optical performance. The housing comprises a quartz window, a thermo-electric-cooler (TEC), and NTS thermistor to set and control the working temperature.

at 3.33 µm (3000 cm^{-1}) and 3.57 µm (2805 cm^{-1}) is for our four-wavelength sensing system the most attractive procedure, compatible with the emission spectra of mid-infrared LEDs.

3.2.3 Sensor system

Instead of labelling or staining of suspicious biological samples, or recording their IR absorbance spectra in the entire wavelength region between 2 and 20 µm with an IR spectroscope, the sensor system measures the IR absorbance at four specific wavelengths. As IR source, two pulsed LEDs with centre wavelengths of 3.40 and 3.65 µm and an emission bandwidth of 0.5 µm are used (see Fig. 3.4 and Table 3.1 for more specifications). The emitted light of the two LED IR sources is collimated by plano-convex lenses and directed at a filter wheel comprising narrow band-pass filters (NBP) to obtain the specific IR wavelengths. As a result, from each LED multiple wavelengths can be selected (in this case 3.33 and 3.42 µm from the 3.40 µm LED and 3.51 and 3.57 µm from the 3.65 µm LED).

Before introducing the MID - infrared sources and detector, the optical parts of the sensor system have been aligned with 660 nm (red light) emitting LEDs. The beam angle of these LEDs are similar to that of the infrared LEDs (both have a 10° beam angle). However, instead of being a perfect

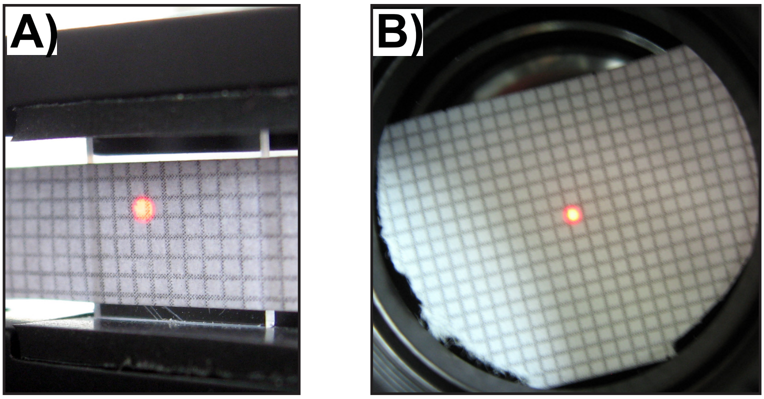

Figure 3.5: Photo of a focused LED spot on a 1 x 1 mm^2 grid for sensor alignment. **A)** Focused light at the sample position, containing a 1 mm thick IR transparent calcium-fluoride slide. **B)** Focused light at the detector position.

Table 3.1: LED (pulsed at a current of 1A) and photodiode specifications at 22 °C.

	LED 34	LED 36	PD 34	
Peak wavelength	3.40 ± 0.05	3.65 ± 0.05	3.35	µm
Pulsed power	500 ± 100	350 ± 70	-	µW
Switching time	≤20	≤20	≤20	ns
Far-field pattern	≤20	≤20	≤20	°
Cut-off wavelength	-	-	3.7	µm
Detectivity	-	-	$\geq 0.5 \times 10^{11}$	$\frac{\text{cm}\sqrt{\text{Hz}}}{\text{W}}$
Emission bandwidth	0.5	0.5	-	µm
Detection range	-	-	2.85 - 3.65	µm

point source, the emitted light pattern of an LED is shaped like a square surrounded by a ring. After alignment, the smallest achieved focused light spot had a diameter of approximately 1 mm at both sample and detector position (see Fig. 3.5). This is due to the square die shape and size.

The NBPs (obtained from NDC Infrared Engineering Ltd, Essex, United Kingdom) all have a bandwidth (B/W) of less than 1% of the centre wavelength at full width and half the maximum peak transmission. The transmittance spectra of the four NBPs are depicted in Fig. 3.6. After passing the NBP, the two selected wavelengths are focused on a 1.5 mm diameter aperture by a beam-splitter (obtained from ISP Optics, Irvington, NY, USA) and another plano-convex lens. To direct the transmitted light through a sample

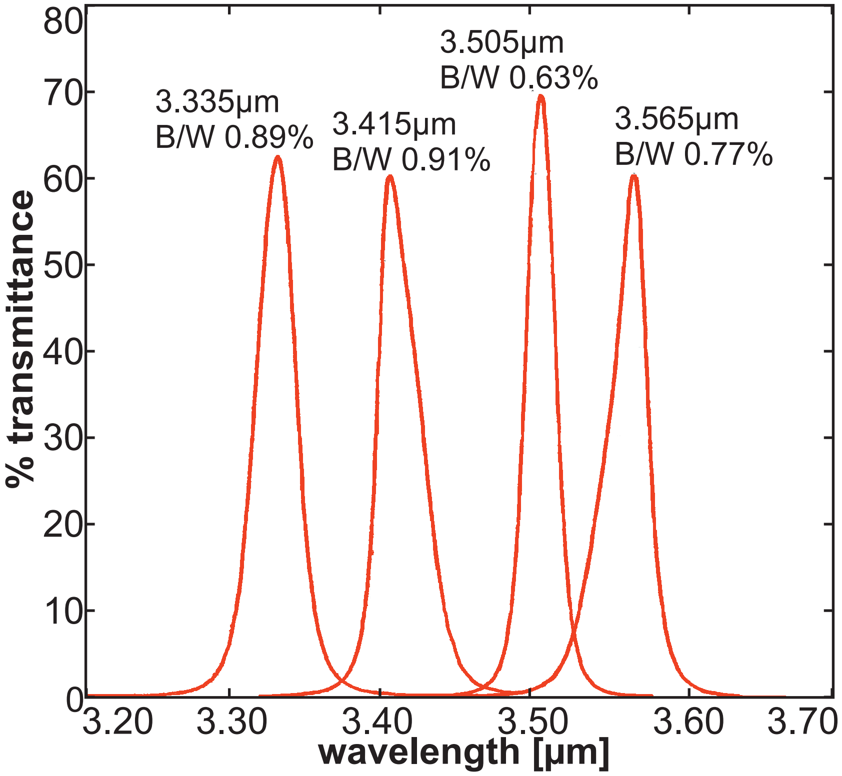

Figure 3.6: Transmittance spectra of the four narrow band-pass filters. The filters with centre wavelength of 3.335 and 3.565 µm are used to measure the IR absorbance for the reference points, the 3.415 and 3.505 µm filters are used for specific CH_2-antisymmetric and CH_2-symmetric stretch measurements. All filters have a bandwidth (B/W) of less than 1% (percentage of the centre wavelength at the full filter width at half the maximum peak transmission).

to a room temperature operable photodiode, two additional plano-convex lenses are used. By rotating the filter wheel, the two other filters can be selected. During experiments, centre wavelength shifting of the LEDs and photodiode is prevented by keeping them at a constant temperature (which can be chosen in the range of 5 - 20 °C). This is realised by a thermo-cooler built into the housings. The LEDs and PD were obtained from Mid-IR Diode Optopair Group, St. Petersburg, Russia. All other components were obtained from Thorlabs, Dachau, Germany.

Two drivers, DLT-37M obtained from IBSG Co. Ltd, St. Petersburg, Russia, were used to operate the LEDs (with a centre wavelength of 3.4

Table 3.2: Logic states LD34 driver versus LD36 driver.

LED 34 driver Clock	LED 34 driver Master reset	LD36 driver Clock
0	0	1
0	1	0
1	0	0
1	1	0

and 3.6 µm, respectively). The current of the LED pulses can be set from 0 to 2A, with a duration of 0.6, 0.8, 1, 1.2, 2, 4, 8, 10, 15, or 20 µs, at a carrier frequency of 0.5, 2, 8, or 16 kHz. To measure infrared absorbance at two wavelengths simultaneously, we needed to adjust the LED drivers to operate the LEDs at alternating pulse mode. This was realised by connecting the divided clock frequencies from the 12 channel binary counter (HEF4040B) of one driver (0.5, 2.0, 8.0, and 16 kHz carrier frequencies extracted from a 32 kHz oscillator signal), and the master reset signal through a NOR gate (Table 3.2) to a 4 stage analogue multiplexer of the second driver (of which the clock and 12 stage binary counter were disconnected). As a result, all driver settings, temperature, pulse current, and duration, are still adjustable per LED. The fraction of infrared light transmitted through the sample was captured by a photodiode, with 3.35 µm centre wavelength and 3.7 µm as cut-off wavelength, and converted to a current. The current-to-voltage amplified photodiode signal (AMT-7M amplifier, also obtained from IBSG Co. Ltd, St. Petersburg, Russia) is only recorded when an LED is emitting. This is realised by connecting the clock signals of both LED drivers and the amplified photodiode signal to a data acquisition board (National Instruments USB 6251, sample rate of 1.25 MS/s at a 16 bit ADC resolution), which is programmable with a software script. This method is used to measure the IR absorbance values at two wavelengths simultaneously. In Fig. 3.7 the schematic of the sensor system is depicted and in Fig. 3.9 a photograph is shown of the realised system.

3.2.4 Data analysis

The absorbed IR light at the four wavelengths to determine the CH_2-stretch ratio is obtained by comparing the transmittance difference of a sample-containing slide and an empty reference slide. We used 9.5 x 9.5 x 1 mm^3

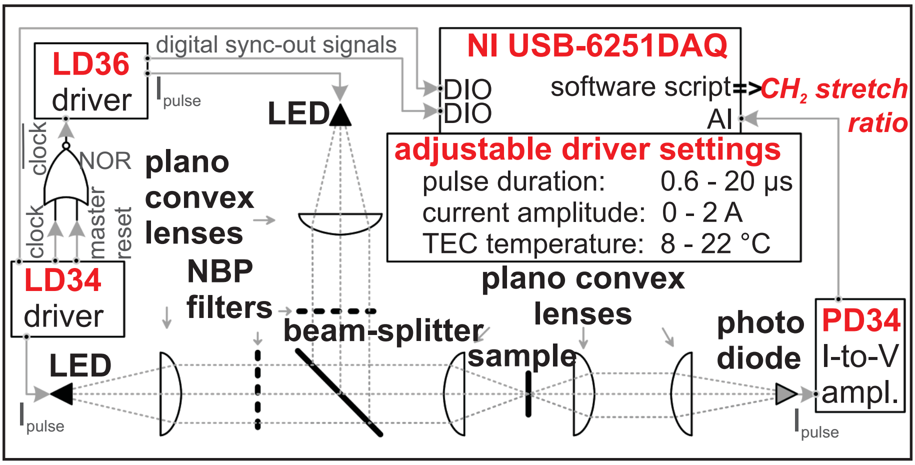

Figure 3.7: Schematic of the quadruple wavelength IR sensor system. Two LEDs emitting in a broad range so that with changeable narrow band pass filters two wavelengths can be selected (3.33 and 3.42 µm for LED34 and 3.51 and 3.57 µm for LED36). Both LEDs operate at an alternating pulse mode. A beam-splitter and plano-convex lens are used to focus the two beams through a 1.5 mm aperture on the same sample spot. A photodiode is used as detector and can be operated at room temperature. The current-to-voltage amplified photodiode signal is only recorded when a LED is emitting. This is realised by connecting the clock signals of both LED drivers and the amplified photodiode signal to a data acquisition board, which is programmable with a software script. By rotating the filter wheel, the two other filters can be selected.

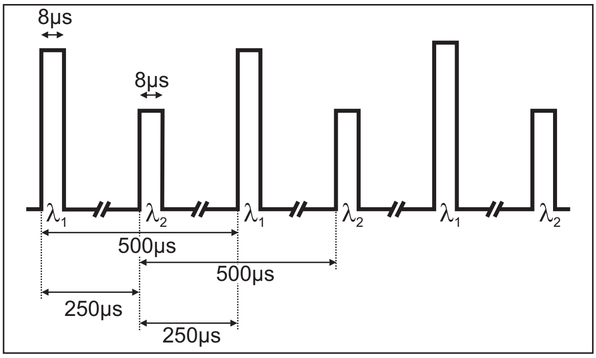

Figure 3.8: Synchronized pulses of two LEDs (λ_1 and λ_2) operated in alternating pulse mode.

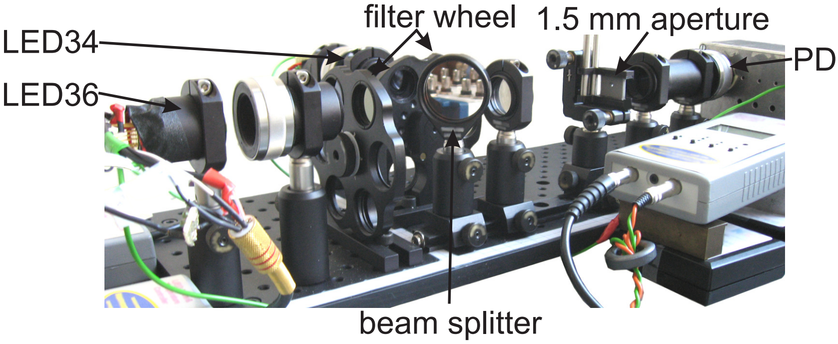

Figure 3.9: Photograph of the quadruple wavelength IR sensor system.

and 6 x 6 x 1 mm^3 infrared transparent calcium-fluoride slides. When the clock signal of one of the LED drivers gives an up-flank (trigger), the current-to-voltage amplified photodiode signal is recorded for a duration of 12 µs. With a sample rate of about 1.25 MS/s, the data acquisition board records 15 data points per pulse (in Fig. 3.10, a single recorded pulse is depicted). To extract the information out of a pulse, the mean voltage of the four second highest values between the rise and fall time is used. By averaging values of multiple pulses, more accurate absorbance values are obtained. The extracted absorbance per wavelength values (in voltage) are used to calculate the absorbance ratio between CH_2-symmetric and CH_2-antisymmetric stretch as is described in the detection method section. In Fig. 3.11 a flow chart is depicted of how to determine this ratio by measuring the IR absorbance at four wavelengths.

Compared to FTIR spectroscopy where the whole IR spectrum can be recorded, the raw data measured with the sensor system consist of IR transmittance data at the four specific wavelengths (the averaged data of a single MDCK spot measurement is given in Table 3.3).

3.3 Results

3.3.1 Sensor validation

The quadruple wavelength IR absorbance sensor system has been validated by recording 500 emitted IR pulses at each of the four wavelengths. The voltage distribution of the current-to-voltage amplified IR pulses recorded by the photodiode per wavelength are depicted in Fig. 3.12.

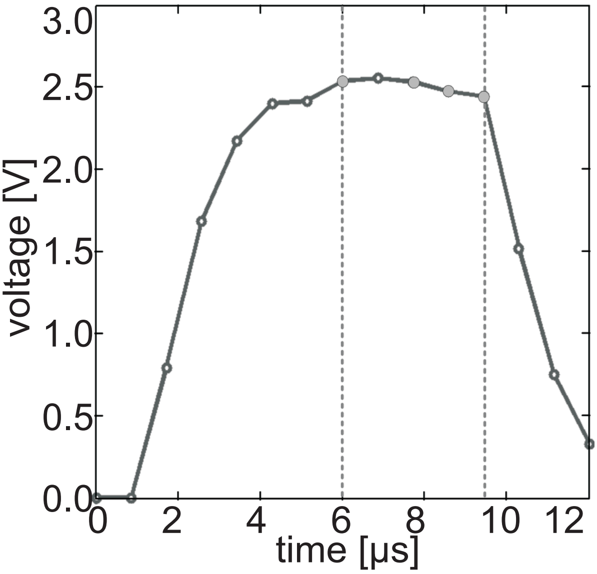

Figure 3.10: Current-to-voltage amplified photodiode signal of a single recorded LED pulse. By averaging the voltage values of the four second highest sample points (grey dots), one voltage value will be assigned to the pulse for further comparison.

Table 3.3: Average IR transmittance values of a MDCK spot recorded by a photodiode connected to a current-to-voltage amplifier. Each value is based on 2500 measurements.

Wave-length [µm]	wave-number [cm^{-1}]	ref. (no cells) [V]	st-dev [mV]	MDCK [V]	st-dev [mV]
3.33	3000	2.607	1.2	1.871	1.2
3.42	2928	1.627	1.9	1.083	0.8
3.51	2853	0.882	1.9	0.646	0.5
3.57	2805	0.636	1.1	0.499	0.5

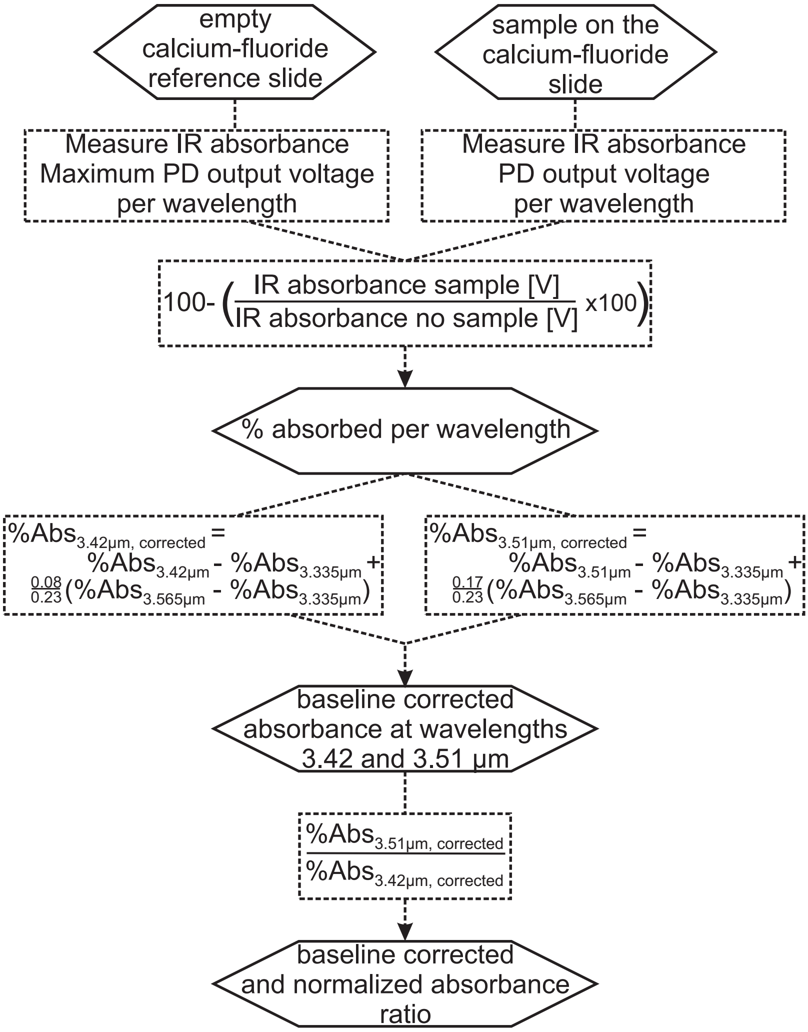

Figure 3.11: Flow chart explaining how the lipid CH_2-symmetric / CH_2-antisymmetric stretch ratio (3.51 / 3.42 µm, respectively) is determined. By comparing the amplified current-to-voltage photodiode signal of an empty reference and a sample-containing calcium-fluoride slide, baseline correction and normalization is applied to calculate the CH_2-stretch ratio. The two measured absorbance values at 3.335 and 3.565 µm are used to describe the baseline. With this baseline the functional absorbance values at wavelengths 3.42 and 3.51 µm can be calculated (e.g. 0.08 / 0.230 corresponds with the fraction of the absorbance difference between the two base points; 3.42 µm is 0.08 µm from the base point at 3.335 µm; 0.230 µm corresponds with the wavelength distance between the two base points).

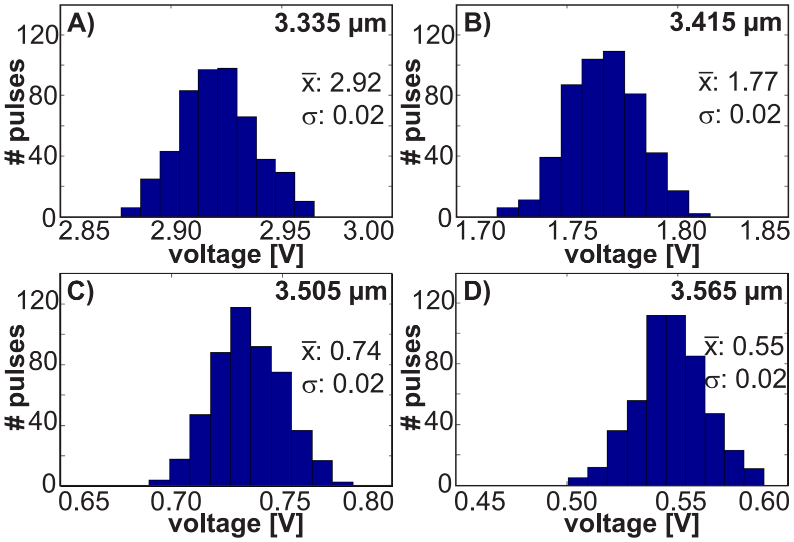

Figure 3.12: The distribution of the current-to-voltage amplified IR pulses recorded by the photodiode per wavelength. At each wavelength the averaged voltage $\overline{x}$ and standard deviation σ is shown in voltage.

The standard deviation σ of the recorded pulses is 20 mV (or 1% for the recorded pulses emitted by the 3.4 µm wavelength LED and approximately 3.5% for the pulses emitted by the 3.6 µm wavelength LED).

In order to validate the sensor system with a biological sample the CH_2-symmetric / CH_2-antisymmetric stretch ratio of a yeast sample has been derived both by IR spectroscopy and the sensor system. Yeast samples, which also contain the CH_2 absorbance peaks, are, compared to mammalian cell lines, much easier to prepare. The bars f1 - f3 in Fig. 3.13 represent the CH_2-stretch ratio of three sample spots of dried yeast. Each spot, located on a single IR-transparent calcium-fluoride slide, was measured twice with a Bruker Equinox 55 spectrometer. The settings were: 1 mm IR beam diameter, 128 scans per spectrum, and a resolution of 4 cm^{-1}.

To measure the CH_2-stretch ratio with the sensor system, the LEDs were set to emit pulses with a duration of 8 µs, operating at a carrier frequency of 2 kHz (duty cycle of 1.6%). More accurate data values were obtained by averaging 500 recorded pulses per wavelength for a single measurement. The thermo-coolers of the two LEDs (3.40 and 3.65 µm centre wavelength) and photodiode were set to 10, 8.5, and 20°C, respectively. In Fig. 3.13 the CH_2-stretch ratio recordings of four sample spots (s1 - s4) of yeast located

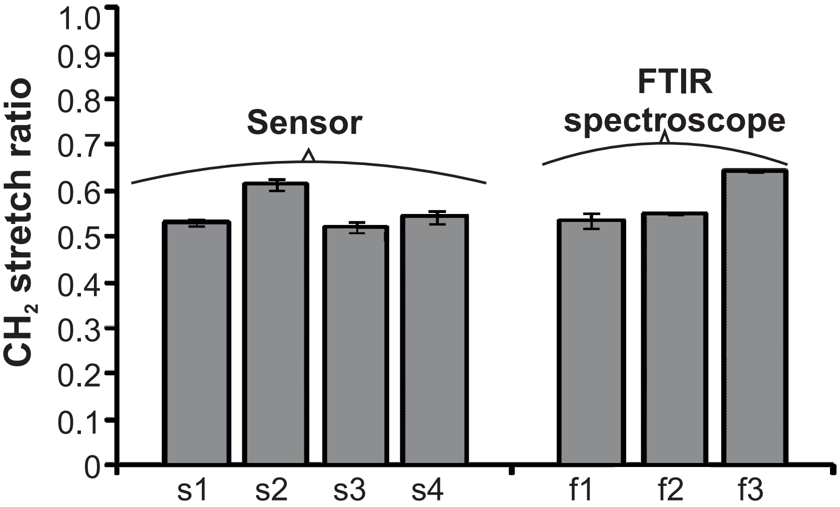

Figure 3.13: CH_2-stretch ratio of four sample spots of yeast, each recorded four times with the quadruple wavelength sensor (s1 - s4). The three sample spots f1 - f3 were measured with a Bruker Equinox IR spectrometer (settings: 1 mm beam diameter, 128 scans per spectrum at a resolution of 4 cm^{-1}). The spots were all located on the same 9.5 x 9.5 x 1 mm^3 IR transparent calcium-fluoride slide. Bars represent means ± standard deviation per measured sample spot.

on a single calcium-fluoride slide are shown. Each 1.5 mm diameter spot was recorded four times and averaged. Besides the mean CH_2-stretch ratio value per sample spot, the standard deviation is also given.

As can be seen in Fig. 3.13, the recorded IR absorbance values of both measurement systems, IR spectroscope and sensor, yields similar CH_2-symmetric / CH_2-antisymmetric stretch ratios. The proof-of-concept study shows that the sensor system, which measures the IR absorbance at only four wavelengths, can be successfully used to determine the CH_2-stretch ratio of cell samples. The CH_2-stretch ratio could otherwise only be determined by using an IR spectroscope.

3.3.2 Normal versus malignant cell type discrimination

The CH_2-stretch ratio has been investigated to determine its potential as indicator for malignant versus normal cells. After the successful validation of the sensor system with biological yeast samples, two epithelial kidney cell samples were prepared, normal MDCK and carcinoma Caki-1. Both cell types were cultivated and prepared under the same conditions. The

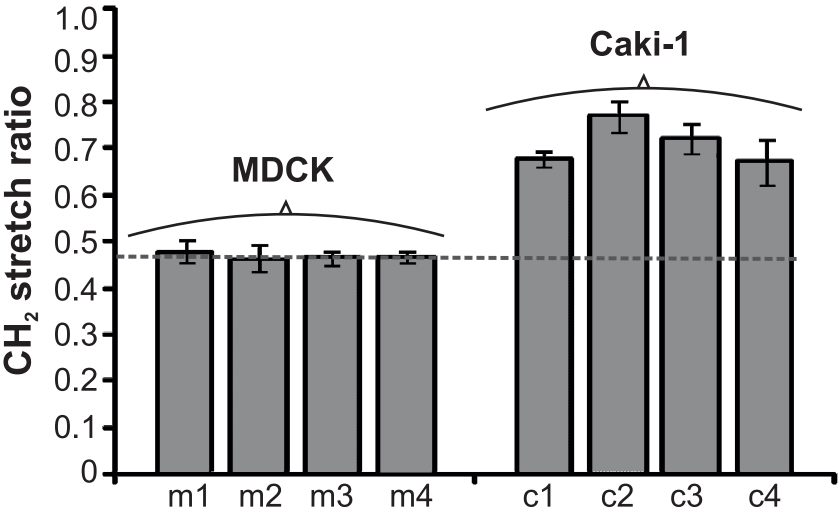

Figure 3.14: Sensor CH_2-stretch ratio measurement of four sample spots of dried normal MDCK (m1 - m4) cells and carcinoma Caki-1 cells (c1 - c4), each recorded four times. Bars represent means ± standard deviation per measured sample spot. There is a significant and well-detectable increase in CH_2-stretch ratio of the Caki-1 carcinoma cell line compared to the normal MDCK cell line (respectively 0.73 compared to the MDCK value of 0.47).

LEDs were set to emit 8 µs pulses at a carrier frequency of 2 kHz. From each prepared sample, the CH_2-stretch ratio of four spots were measured four times. The results have been depicted in Fig. 3.14.

The CH_2-stretch ratio measurements of both cell types, MDCK and Caki-1, yielded mean values with small standard deviations, respectively 0.47 ± 0.01 and 0.73 ± 0.03. As can be seen in Fig. 3.14, there is a significant and well detectable CH_2-stretch ratio difference between the normal MDCK and carcinoma Caki-1 epithelial kidney cells: the ratio changes from 0.47 to 0.73. Repeated measurements of the same sample slides, stored for one week at room-temperature, yielded similar results (MDCK 0.48 ± 0.01 and Caki-1 0.71 ± 0.04).

3.4 Discussion

By comparing IR spectroscope recorded absorbance spectra of benign and malignant breast [72], oesophagus [70], and brain [92] tissue slides, found in literature, differences in lipid CH_2-stretch ratios due to tumour development can be derived. These tissue slides, all prepared from biopsies, comprise identified regions of normal and tumour cells. Both with IR spectroscopy and with our sensor system it is possible to investigate spots within such sample regions. The sample slides used for our sensor measurements were prepared from well defined cell lines, in order to have known samples to test the sensor response to normal and carcinoma cells. On each sample slide only cells from a normal or carcinoma cell line were attached, resulting in a homogeneous tissue layer of a single cell type. The repeatability of the sensor measurements, comparing different measurements per spot, shows slight variations. By averaging multiple recordings of the same spot, more accurate CH_2-stretch ratios were obtained.

The reliability of the quadruple wavelength sensor system measurement method was tested by recording the CH_2-stretch ratio of four different spots on the same sample slide. It can be seen in the measurements that although the absolute IR absorption per sample spot can differ, the ratio CH_2-symmetric / CH_2-antisymmetric stretch is fairly equal.

In chapter 4 the feasibility of the CH_2-stretch ratio as biomarker to distinguish between normal and tumour cells of epithelial kidney and melanocyte origin will be further investigated.

3.5 Conclusions

A novel sensor system was designed and realised to measure the CH_2-stretch ratio by recording IR absorbance at four specific wavelengths. Sensor experiments on dried spots of baker's yeast yielded comparable ratios as with the IR spectroscope measurement. After that the new quadruple wavelength infrared sensor was used to determine the CH_2-symmetric / CH_2-antisymmetric stretch ratio between normal and tumour epithelial kidney cells. The results show a significant difference of this ratio (0.47 to 0.73).

Chapter 4

Label-Free Tumour Screening

The research described in this chapter consist of three main parts. In section 4.3.1 - 4.3.3, the feasibility to distinguish between normal and malignant cells by a four-wavelength, mid-infrared absorbance measurement method is investigated. The cancer types are of epithelial kidney and melanocyte origin. For both types the CH_2-stretch ratio of a normal cell line is compared with multiple malignant cell lines.

The main contributor stabilizing the lipid chains in the cell membrane is cholesterol. To investigate whether cholesterol bound to the lipids in the plasma membrane influences the CH_2-ratio, MDCK cells were exposed to the cholesterol reducing agent methyl-β-cyclodextrine at different concentrations (section 4.3.4).

Besides investigating the feasibility of the CH_2-ratio as tumour cells indicator another, highly interesting aspect would be if it could also be a method to monitor therapy on tumour cells. To investigate this aspect the influence of chemotherapy drugs on tumour cells has been investigated. When the chemotherapeutic drug is effective, the drug induces membrane changes, e.g. tightening the inner membrane of cells when in apoptosis. The influence of the drug cisplatin on the CH_2-stretch ratio of melanoma cells is presented in section 4.3.5.

4.1 Introduction

As described previously, the majority of tumour detection methods available to date are based on visual inspection of primary tumours. Visual inspection methods still result in a high number of false positives and negatives and there is still no commonly accepted marker set available for the accurate diagnosis of malignant melanoma [3, 5]. Improved diagnostic methods are highly important for increasing the overall survival rates of cancer patients [13, 18]. In this chapter, the potential of the proposed label-free infrared absorbance based measurement method for determination of the CH_2-symmetric to CH_2-antisymmetric stretch ratio, to aid in the detection of the presence of cancer cells and to differentiate between various cancer cells, was assessed [91, 93]. The monitoring of CH_2-stretches of phospholipid acyl chains is a very strong concept, because it enables to look at changes in molecular interactions and it inherently compensates for differences in cell amount and measurement spot size. For this study a normal epithelial kidney cell line, three carcinoma epithelial kidney cell lines, an adult primary human melanocyte cell line, and three human melanoma cell lines were investigated. As described in section 2.2, cholesterol is required for normal cellular function of mammalian cell membranes. Plasma membranes of typical mammalian cells consist of about 20 - 25% lipid mass cholesterol. It has a condensation and ordering effect on the lipid structure [84–87, 94], which leads to an increased ordering of the hydrocarbon chains of lipids, a reduction of their mean molecular area, and to a decrease in CH_2-symmetric stretch [77, 95, 96]. We postulate that the increased CH_2-stretch ratio of tumour cells compared to normal cells is caused by a reduction or reallocation of membrane stabilizing agents such as cholesterol. We have found supporting evidence in publications by Cai et al. and Guyot-Sionnest et al. They show that after overexpressing caveolin-1 in the plasma membrane of doxorubicin-resistant breast cancer cells (Hs578T) the cholesterol level decreased by 30% [79]. It is shown by sum-frequency vibrational spectroscopy of a Langmuir film that, when straightening up a pentadecanoic acid molecule, the CH_2-symmetric peak decreases [78]. Methyl-β-cyclodextrin (MβCD; see Fig. 4.3) redistributes cholesterol in the plasma membranes of MDCK cells without influencing the cell viability [97,98]. To investigate the mechanism influencing the CH_2-stretch ratio of mammalian cell membranes, a normal epithelial kidney cell line was exposed to the plasma membrane bound cholesterol reducing agent methyl-β-cyclodextrin. Cisplatin (Fig. 4.1) is an antitumour agent commonly used for the treatment of various tumours including melanoma. At a lethal dose, it kills cells by the formation of DNA adducts, triggering apoptosis [99–101]. After intravenous administration, cisplatin is relatively non-reactive due to the high concentration of chloride ions (± 100 mM) in the extracellular space. When crossing the plasma membrane, the chloride concentration drops to 3 mM, activating cisplatin. In active form, cisplatin (an electrophile) reacts with any nucleophile including sulfhydryl groups on proteins and nucleophile groups on nucleic acids [102]. Determining the lowest “working dosage”

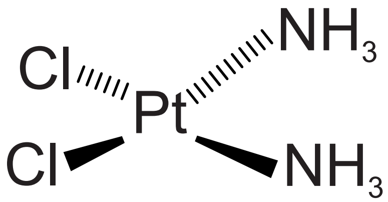

Figure 4.1: Fischer projection of *cis*-diamminedichloroplatinum(II), cisplatin.

is of clinical importance because the chance of severe side effects such as multiorgan toxicity, deafness, blindness, seizures, and vomiting must be reduced [103]. When inducing apoptosis in human colon cancer cells by cisplatin, lipid raft aggregates are formed [104, 105]. Singh et al. showed that apoptotic cells change morphology [106]. Plasma membrane pores, or leaky spots, are formed by rigid patches of tight packed phospholipids in the inner plasma membrane. These rigid patches are formed due to an increased amount of saturated fatty-acids. In this chapter, also the change in CH_2-stretch ratio when cells are in apoptosis will be investigated, specifically the decrease in CH_2-stretch ratio due to the formed, rigid, tightly packed phospholipids.

4.2 Material and methods

4.2.1 Cell lines

The CH_2-stretch ratio as indicator for tumour cells have been tested on two different cancers. The first type was of epithelial kidney origin. As normal cell type we used MDCK (Madin-Darby Canine Kidney, ATCC CCL-34), as carcinoma mouse Renca (ATCC CRL-2947) and human carcinoma A498 (ATCC HTB-44), and Caki-1 (ATTC HTB-46). The second cancer type is originated from human melanocyte cells. As normal cell type HEMa (Primary Human Melanocytes adult, obtained from Invitrogen, Germany) was used and as melanoma A375 (ATCC CRL-1619), M14 (a gift from Dr. Soldano Ferrone; Dept. of Immunology, University of Pittsburgh), and 518A2 (a gift from Dr. Peter Schrier, LUMC, Leiden, the Netherlands) were used.

4.2.2 Sample preparation

The cell lines were all cultivated under the same conditions in monolayer on 6 x 6 x 1 mm^3 IR transparent calcium-fluoride slides, in a humidified atmosphere containing 5% CO_2 and 95% ambient air at 37°C. The cell cultures were free of mycoplasma and pathogenic viruses. The epithelial kidney cell lines were cultivated in Dulbecco's Modified Eagle Medium (DMEM), 2 mM L-glutamine, 10% fetal calf serum (FCS), and antibiotics (100 units/mL penicillin, 100 µg/mL streptomycin, and 0.25 µg/mL Amphotericin B), all obtained from Lonza Bioscience, Germany. The melanocytes were maintained in M254-500 medium (Invitrogen, Germany) supplemented with PMA-Free HMGS2 (Invitrogen, Germany).The human melanoma cell lines were maintained in RPMI 1640 medium (Biochrom AG, Germany). Media were supplemented with 10% fetal calf serum and 1% antibiotics. Mixtures of Caki-1 and MDCK cells were prepared by trypsinizing both cell lines, and their concentrations were determined with a coulter counter. Both cell types were afterwards transferred, in % Caki-1 / % MDCK cell ratio's of 100/0, 80/20, 50/50, 20/80, and 100/0 to CaF_2 slides containing wells of a 24-well plate. To visualize the mixing method, one of the two cell types has been stained with DiO, a viability stain that binds to phospholipid bilayer membranes, prior to mixing them with the other cell type (see Fig. 4.2). Before the IR absorbance was measured, the sample slides were rinsed in warm PBS to remove detached cells and culture medium components. The high IR absorbing water fraction was removed by drying the slides for 3 hours in a sterile laminar flow cabinet.

To determine a CH_2-stretch ratio change by extracting cholesterol from the cell membrane, three different MDCK cell slides where exposed to respectively 0 (as control), 10, and 20 mM MβCD (obtained from Sigma-Aldrich, product number C4555, MW = 1320 gram/mol) for 1 h at 37°C and 5% CO_2. After incubation, the cell sample slides were washed twice in PBS to remove the MβCD solution and dried for 3 hours in a laminar flow cabinet to remove the water fraction. Three melanoma cell lines were exposed for 16 h to 20 µM cisplatin. Of each cell line exposed to cisplatin two sample slides were prepared. The kinetic response of A375 melanoma cells to 20 µM cisplatin was investigated by exposing them for 0 min, 15 min, 30 min, 2 h, and 16 h to cisplatin. Before IR absorbance was measured the slides were rinsed in warm PBS to remove detached cells and culture medium components. The high IR absorbing water fraction was removed by drying the slides for 3 hours in a sterile laminar flow cabinet.

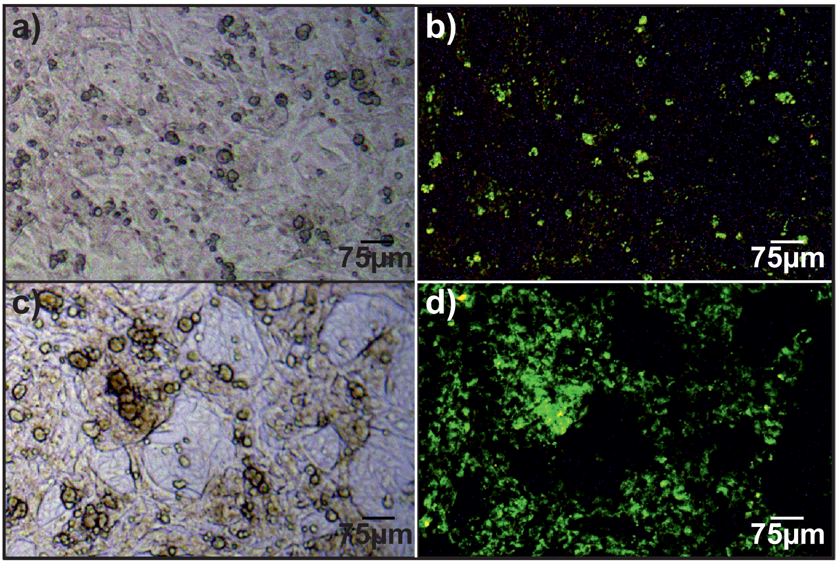

Figure 4.2: Mixed Caki-1 and MDCK epithelial kidney cells. **a)** and **c)** are photographs of mixed Caki-1 and MDCK cells by light microscopy. **b)** and **d)** are images taken by fluorescence microscopy (the green/grey dots in represent the stained cells) of the same sample slides as depicted in **a)** and **c)**. In **b)**, only the MDCK cells were stained and in **d)** only the Caki-1 cells were stained.

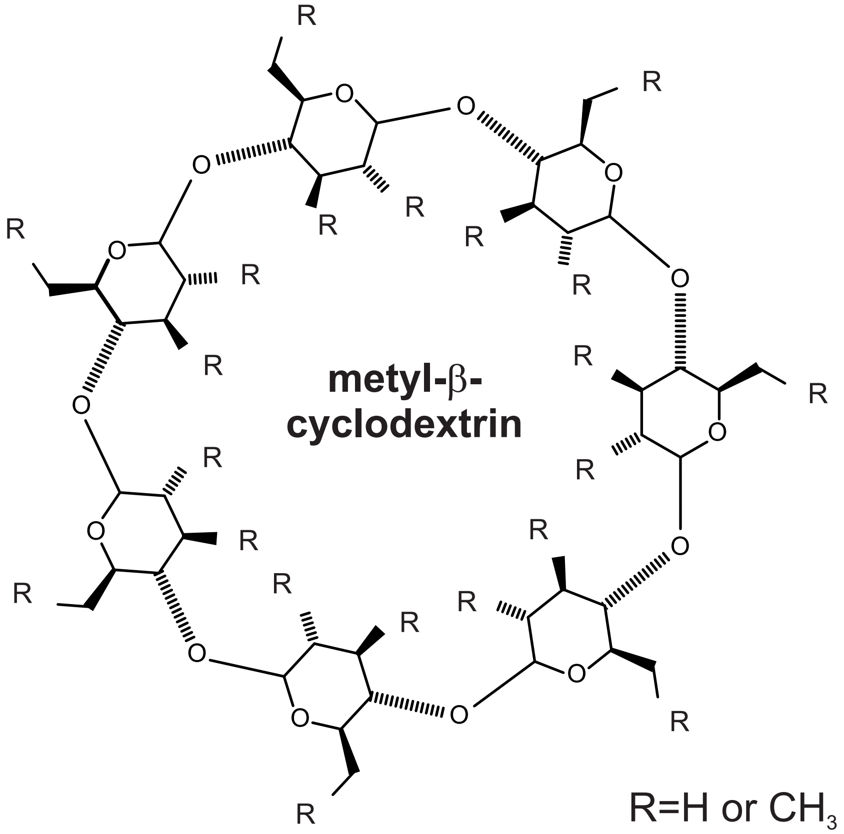

Figure 4.3: Fisher projection of a methyl-β-cyclodextrin molecule. MβCD is a cyclic oligomer comprising 7 sugar molecules.

4.2.3 Cholesterol redistribution

The influence of cholesterol on the CH_2-stretch ratio was investigated by exposing MDCK cells to 0, 10, and 20 mM of MβCD. The chosen incubation time was 1 hour. Francis et al. have shown that most of the cholesterol reduction in MDCK cells occurred in the first 30 min of exposure [107, 108]. Cyclodextrins are cyclic glucose oligomers that have the capacity to segregate lipids in their hydrophobic core. The water - soluble MβCD, a seven sugar ring molecule, is known to form soluble inclusion complexes with cholesterol, thereby enhancing its solubility in aqueous solution [98, 109]

Table 4.1: LED and photodiode settings.

	LED 3.4 µm	LED 3.6 µm	Photodiode 3.4 µm	
current	470	1470	-	mA
temperature	10.1	10.6	19.8	°C

4.2.4 Sensor settings

The LEDs were set to pulsate for 12 µs at a repetition rate of 2 kHz, 2.4 % duty cycle. Of each cell sample, the CH_2-stretch ratio of four 1.5 mm diameter spots were averaged. Each of the four spots were measured 1250 - 2500 times. Specific settings are depicted in Table 4.1.

4.2.5 Data analysis

The data acquisition method was further improved by recording the current-to-voltage amplified photodiode output signal at 100 µs instead of 12 µs (compared to Section 3.2.4), allowing to determine the minimum voltage value after the 12 µs LED pulse. To extract the information out of a single pulse, the mean voltage of the four second highest values, between the rise and fall time, is used. In Fig. 4.4, a single recorded pulse is depicted. By averaging the values of multiple pulses more accurate absorbance values are obtained. These extracted absorbance per wavelength values, in voltage, are used to derive the absorbance ratio between CH_2-symmetric and CH_2-antisymmetric stretch.

The CH_2-stretch ratio of a single 1.5 mm diameter sample spot was obtained by averaging the values of five measurements. Small wavelength absorbance peak shifts due to chain rotation configurations will not influence the measurements, because of the 30 nm bandwidth of the selected NBP filters [81].

4.2.6 Statistical analysis

Kruskal - Wallis tests were performed to test for statistically significant differences between the CH_2-stretch ratios of the measured cell types.

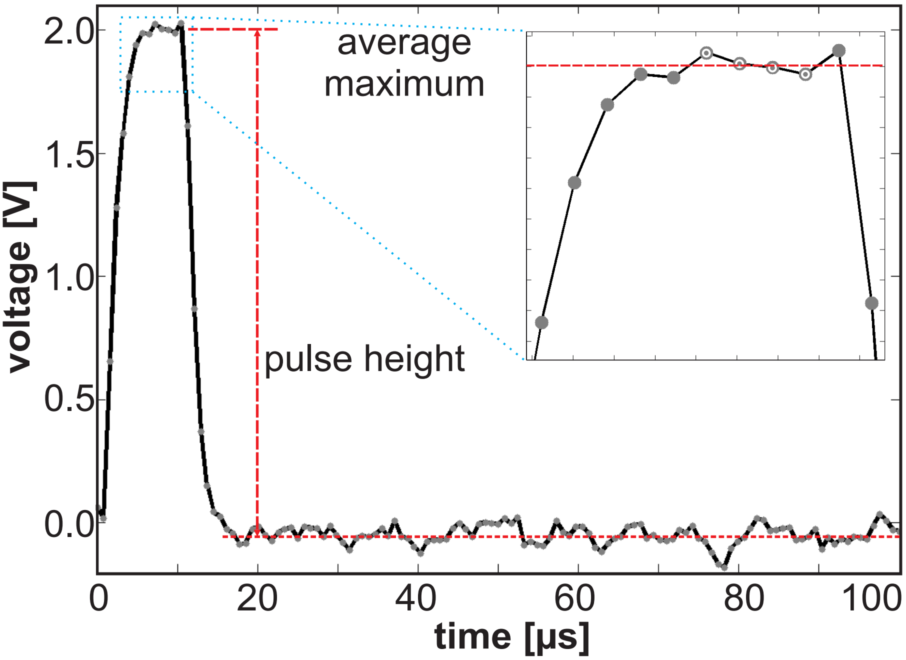

Figure 4.4: Current-to-voltage amplified photodiode signal of a single recorded LED pulse. By averaging the voltage of the four second highest sample points (insert: white dots), one voltage value is assigned to the pulse for further comparison.

4.3 Results

4.3.1 Epithelial kidney carcinoma cells

The IR absorbance ratio between CH_2-symmetric and CH_2-antisymmetric stretch of mammalian cells is determined by a quadruple wavelength infrared absorbance measurement (see Fig. 3.3 Section 3). The cell lines of epithelial kidney origin were normal MDCK cells and the three carcinoma cell lines were Renca, A-498, and Caki-1. From each prepared $6 \times 6\,mm^2$ sample slide the CH_2-stretch ratio of four different 1.5 mm diameter spots were measured. Of each spot the CH_2-stretch ratio of 1250 - 2500 measurements were averaged. The reproducibility of the CH_2-stretch ratio as tumour indicator was evaluated by comparing measurement results of two different passages per cell line. Between the cell passages no significant differences in CH_2-stretch ratio have been detected, indicating the usability and reproducibility of the CH_2-stretch ratio method as tumour indicator. As is shown in Fig. 4.5, the Renca, A-498, and Caki-1 carcinoma cell lines had a significant and well-detectable higher CH_2-stretch ratio compared to the normal MDCK cell line. The measurement values of the stretch ratios have standard deviations of 5, 1, 7, and 2% for the first measured cell passage and 2, 1, 1, and 2% for a different cell passage. Also, between the carcinoma cell lines a statistical significant difference in CH_2-stretch ratio has been detected. A statistical analysis, to determine if there is a significant difference between the mean CH_2-stretch ratio of the individual cell lines, has been made by performing a Kruskal - Wallis test for non-normal distributed datasets. The null hypothesis is that all groups have the same CH_2-stretch ratio. The test yielded a probability $P = 3.6 \times 10^{-5}$, indicating that the individual cell lines have a statistical significant difference between their mean CH_2-stretch ratio.

4.3.2 Melanoma cells

We then applied the CH_2-stretch sensing system on melanoma cells. Of this cell type the CH_2-stretch ratio of normal, human melanocyte (HEMa), and three human tumour cell lines (M14, 518A2, and A375) were investigated. The same measurement strategy was used as described previously; four different spots of two different cell passages per cell line were evaluated. As has been shown for the epithelial kidney cell measurements, the CH_2-stretch ratio of the three melanoma cell lines were also higher compared to the nor-

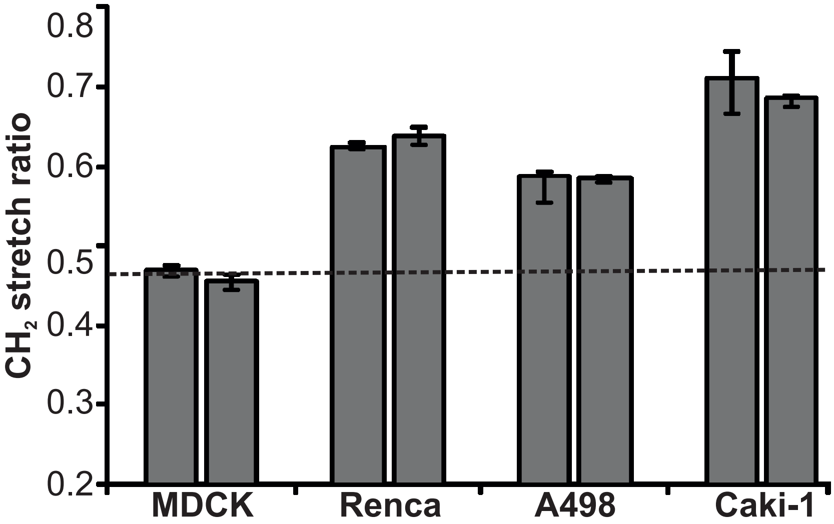

Figure 4.5: Sensor CH_2-stretch ratio measurement of MDCK (mean ± standard deviation, 0.47 ± 0.01 and 0.46 ± 0.01) and carcinoma Renca (0.62 ± 0.01 and 0.64 ± 0.01), A498 (0.59 ± 0.03 and 0.58 ± 0.01) and Caki-1 (0.71 ± 0.05 and 0.69 ± 0.01). Of every cell type the CH_2-stretch ratio of two different cell passages were measured (4 months between measurements). Bars represent means ± SD per cell passage and cell type (each bar comprises the average CH_2-stretch ratio of 4 spots with 1250 - 2500 measurements per spot). There is a significant and well-detectable higher CH_2-stretch ratio measured for the Renca, A-498, and Caki-1 carcinoma cell lines compared to the normal MDCK cell line (respectively 0.63, 0.59, and 0.70 compared to the MDCK value of 0.47).

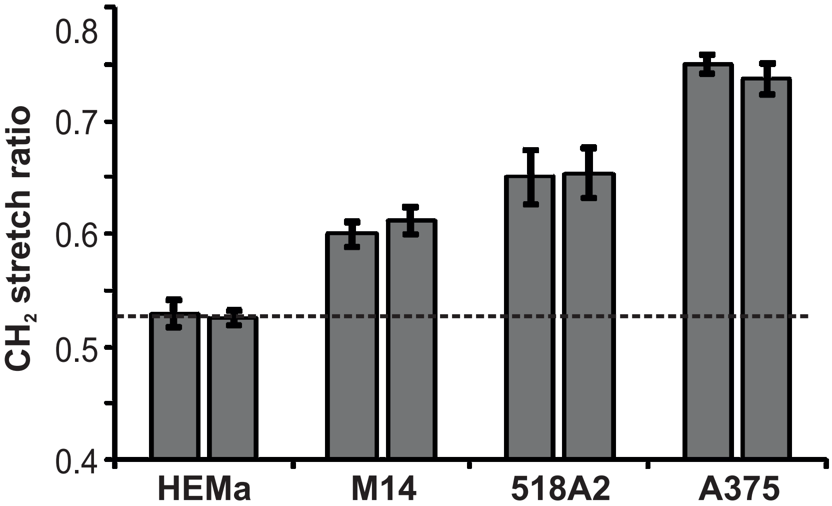

Figure 4.6: Sensor CH_2-stretch ratio measurement of melanocyte HEMa (mean ± standard deviation, 0.53 ± 0.01 and 0.52 ± 0.01) and melanoma M14 (0.60 ± 0.01 and 0.61 ± 0.01), 518A2 (0.65 ± 0.02 and 0.65 ± 0.02), and A375 (0.75 ± 0.01 and 0.74 ± 0.01). Of every cell type two different cell passages were measured (10 - 12 days between measurements). Bars represent means ± SD per cell passage and cell type (each bar comprises the average CH_2-stretch ratio of 4 spots with 1250 - 2500 measurements per spot). There is a significant and well-detectable increase in CH_2-stretch ratio of the M14, 518A2, and A375 melanoma cell lines compared to the normal HEMa melanocyte cell line (respectively 0.61, 0.65, and 0.75 compared to the melanocyte value of 0.53).

mal melanocytes (Fig. 4.6). The standard deviations of the HEMa, M15, 518A2, and A375 cell line measurements were, respectively, 1, 3, 1, and 2% for the first cell passage and 2, 3, 1, and 2% for the next measured cell passage (see error bars). Between the different cell passages no significant differences in CH_2-stretch ratio have been detected. Statistical analysis results of a Kruskal - Wallis test were significant $P = 3.0 \times 10^{-6}$; indicating that the CH_2-stretch ratio of the individual cell lines were significantly different.

4.3.3 Mixed MDCK and Caki-1 cells

In order to determine the feasibility to detect tumour cells in mixtures with “normal” cells, not only pure cell lines were investigated, but also the CH_2-stretch ratio of various mixtures of Caki-1 and MDCK were measured. The investigated cell mixtures have a % Caki-1/% MDCK cell ratio (in cell

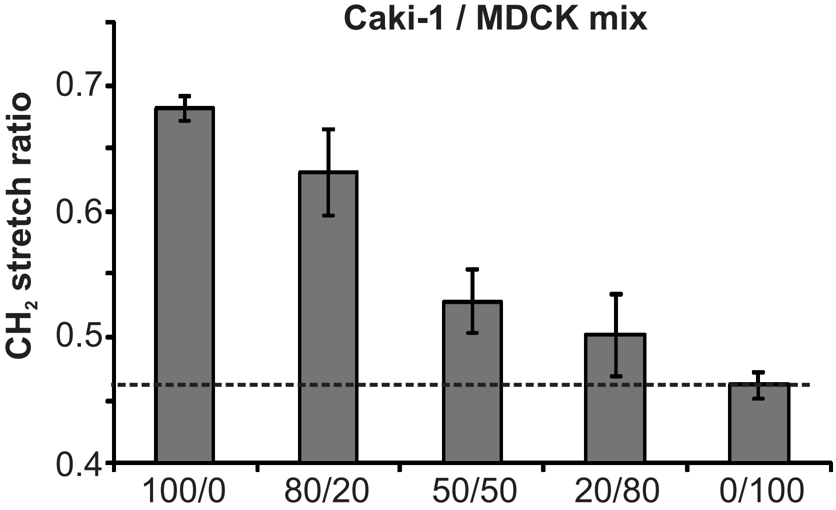

Figure 4.7: Sensor CH_2-stretch ratio measurement of mixtures of MDCK and Caki-1 epithelial kidney cells: 100/0 (mean ± standard deviation, 0.71 ± 0.01), 80/20 (0.62 ± 0.03), 50/50 (0.51 ± 0.01), 20/80 (0.50 ± 0.03), and 0/100 (0.47 ± 0.01) % Caki-1/% MDCK). Bars represent means ± SD per cell mix (each bar comprises the average CH_2-stretch ratio of 4 spots).

amount) of 100/0, 80/20, 50/50, 20/80, and 100/0.

As shown in the histogram depicted in Fig. 4.7, the CH_2-stretch ratio of the cell mixtures decreases when the MDCK cell concentration increases, in other words, an increased concentration of tumour cells yielded a measurable increase in CH_2-stretch ratio.

4.3.4 The influence of cholesterol on the CH_2-stretch ratio

It was investigated whether the membrane stabilizing agent cholesterol has an influence on the CH_2-stretch ratio of MDCK cells. By reducing the amount of plasma membrane bound cholesterol, the CH_2-stretch ratio increases. Several research groups have shown that β-cyclodextrins are capable to sequester cholesterol from cellular membranes. MβCD (methyl-β-cyclodextrin) has been found as the most effective cyclodextrin because of its solubility properties in aqueous solutions so that it can be effectively washed away after the exposure period [110–112]. This was also shown for the cell line that we investigate in this study. Francis et al. have shown that a concentration of 20 mM MβCD is sufficient to reduce the plasma mem-

Table 4.2: Cholesterol reduction efficiency of MDCK by MβCD.

Sample	raw spot volume [A.U.]	background subtracted [A.U.]	cholesterol reduction vs. control [%]
background	34062	-	-
0 mM (control)	185801	151739	0
10 mM MβCD, 1 h	95688	61625	59
20 mM MβCD	86761	52699	65
pure cholesterol	1812998	1778936	-

brane bound cholesterol levels of MDCK cells up to 80% (most cholesterol decrease occurs in the first 30 min [107]). By exposing MDCK cells for 1 h to 0 (control), 10, and 20 mM MβCD, the influence of cholesterol on the CH_2-stretch ratio has been investigated. The cholesterol extraction efficiency (Table 4.2) was determined by performing membrane lipid extraction of the MDCK cells (the two MβCD exposed and control cell samples) and cholesterol separation by TLC (Thin Layer Chromatography) analysis (protocol given in Appendix B).

The measured CH_2-stretch ratios of the three MβCD exposed MDCK cell samples were, respectively (mean $\pm$ SD) $0.46 \pm 0.01, 0.50 \pm 0.01$, and 0.57 ± 0.01, indicating that an increase in CH_2-stretch ratio arises when there is a decrease in, or redistribution of, the membrane stabilizing agent cholesterol (Fig. 4.8).

An increase in CH_2-stretch ratio (an increase in membrane lipid disorder) was successfully measured by exposing viable MDCK cells to respectively, 10 and 20 mM MβCD for 1 h.

4.3.5 The influence of cisplatin on the CH_2-stretch ratio

The measurement results of melanoma cells exposed for 16 h to 20 µM cisplatin yielded a significant CH_2-stretch ratio decrease compared to untreated cells. The CH_2-stretch ratio of M14 cells for example, decreased from 0.60 to 0.42 (see Fig. 4.9).

From the measurement results of a following experiment, it can be concluded that the initial membrane change due to cisplatin occurs within the first 30 min of exposure (see Fig. 4.10).

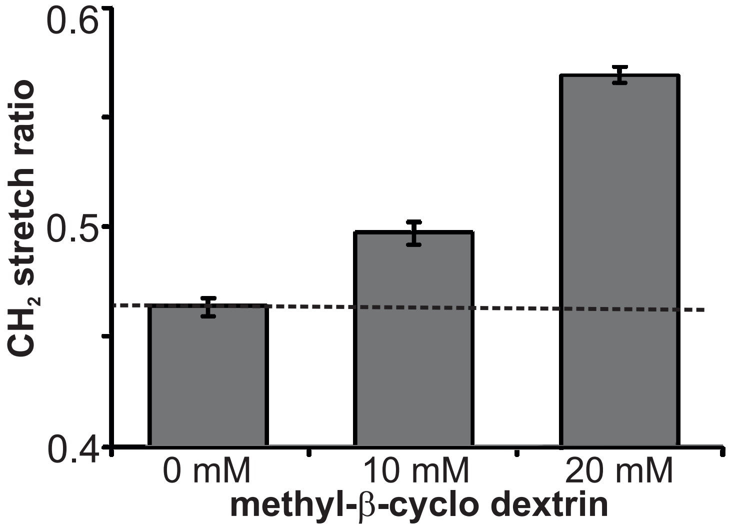

Figure 4.8: Sensor CH_2-stretch ratio measurement of MDCK cells exposed for 1 h to respectively 0 (mean ± standard deviation, 0.46 ± 0.01), 10 (0.50 ± 0.01), and 20 mM (0.57 ± 0.01) Methyl-β-cyclodextrin. Bars represent means ± standard deviation per exposed MβCD concentration (each bar comprises the average CH_2-stretch ratio of 4 spots with 1250 - 2500 measurements per spot). There is a clear CH_2-stretch ratio increase detected when the cholesterol concentration of the MDCK cells is being lowered. The CH_2-stretch ratio increased from 0.46 to 0.57 when MDCK cells were exposed to 20 mM MβCD for 1 h.

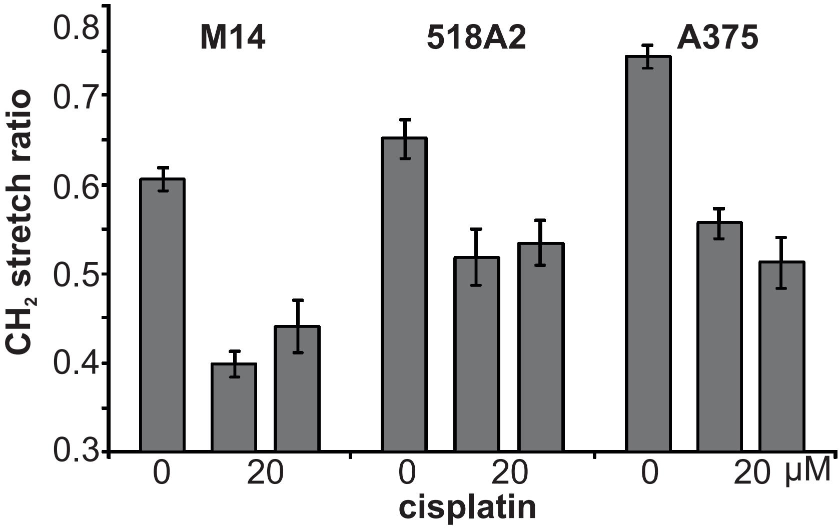

Figure 4.9: Sensor CH$_2$-stretch ratio measurement of M14 (mean ± standard deviation, untreated and exposed, 0.61 ± 0.01, 0.40 ± 0.01, 0.44 ± 0.03), 518A2 (0.65 ± 0.02, 0.52 ± 0.03, 0.53 ± 0.02), and A375 (0.74 ± 0.01, 0.56 ± 0.02, 0.51 ± 0.03) melanoma cells incubated for 16 hours with and without (as control) 20 µM cisplatin. To test the reproducibility of the measurement, the influence of cisplatin to the CH$_2$-stretch ratio of the three cell lines was conducted twice per cell line (on a different cell passage). There is a significant decrease in CH$_2$-stretch ratio of cisplatin exposed melanoma cells. Bars represent means ± standard deviation per cell line, untreated and exposed to cisplatin (each bar comprises the average CH$_2$-stretch ratio of 4 spots with 1250 - 2500 measurements per spot).

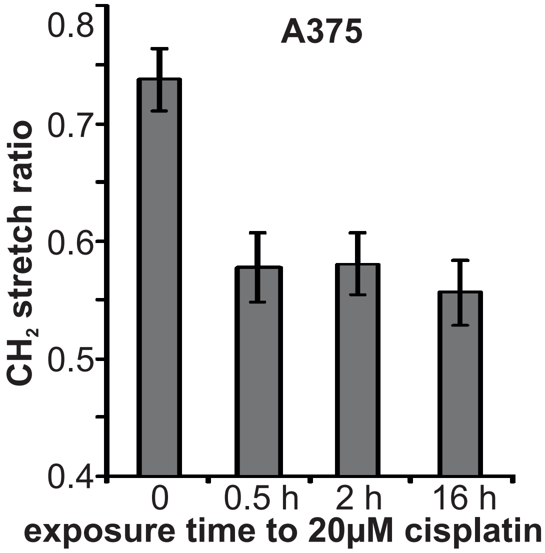

Figure 4.10: A375 melanoma cells exposed to 20 µM cisplatin for 0 (mean ± standard deviation, 0.74 ± 0.03), 0.5 hour (0.58 ± 0.03), 2 hours (0.58 ± 0.03), and 16 hours (0.56 ± 0.03). CH_2-stretch ratio measurements conducted after multiple time intervals show that cisplatin affects the cell membrane even after 0.5 hour of exposure (at a cisplatin concentration of 20 µM). Bars represent means ± standard deviation per exposure time (each bar represents the average CH_2-stretch ratio of 4 spots with 1250 - 2500 measurements per spot).

4.4 Discussion

The evaluated IR spectra of clinical samples published in literature and presented cell line measurement results of epithelial kidney carcinoma (Fig. 4.5) and melanoma (Fig. 4.6) all show a significant and reproducible higher CH_2-stretch ratio compared to normal or benign cell types. The similar measurement results obtained from the samples prepared from different cell passages and the low standard deviations of the measurement values show the reliability of the sensing method. The difference detected between the two human epithelial kidney carcinoma cells (0.59 for A498 and 0.70 for Caki-1) is likely due to the presence of lipid droplets in Caki-1 cells [113] containing relaxed/disordered lipids present in the metastatic Caki-1 cells. The variation between CH_2-stretch ratios found among the three melanoma cell lines could indicate that there is a difference in membrane lipid disorder, which is most likely due to differences in overall cholesterol concentration. As is shown in Fig. 4.7, a distinction in CH_2-ratio between the different Caki-1 / MDCK mixtures was measured. The higher standard deviation of the 80/20 and 20/80 mix ratio measurement results is due to non-uniform distribution of the cell types on the sample slides (see Fig. 4.2). By comparing a ratio, differences in sample thickness, and cell distribution per area that can lead to absolute IR absorbance differences between spots, the outcome will not be influenced. Our measurements show very small deviations of the CH_2-stretch ratio between spots. The LEDs and photodiode were operated at a frequency of 2 kHz and, therefore, it is easy to obtain multiple recordings of the same spot, allowing averaging to obtain more accurate CH_2-stretch ratios. In the temperature range up to 37°C the specific absorbance wavelengths of the CH_2-symmetric and CH_2-antisymmetric stretch band remain unaffected [114–116]. Slight temperature changes in the samples will therefore not affect the measurement results. The LEDs and photodiode were tunable in wavelength by changing their temperature. By stabilizing the temperature (fixed at a temperature between 5 and 20°C) by thermocoolers, which were built into the LED and photodiode housings, peak wavelength shifts were prevented. An increase in CH_2-stretch ratio arises when there is a decrease in, or redistribution of, membrane stabilizing agents, such as cholesterol, and the presence of lipid droplets containing relaxed / less stretched carbon-carbon chains. Swinnen et al. described that enhanced lipogenic enzymes expression and activity in tumour cells results in increased amounts of phospholipids, the building blocks of membranes required for rapidly dividing cells [117]. This could yield more disordered lipid membranes and an increase in CH_2-symmetric stretch. Cai et al. showed that doxorubicin sensitive and doxorubicin resistant Hs578T breast cancer cells, overexpressing caveolin-1, have a (12 and 30%, respectivily) decreased plasma membrane cholesterol level [78]. Schroeder et al. showed that in low and high metastatic mouse melanoma cells there is a significant difference in molar ratio cholesterol per phospholipid in both plasma membrane and microsomes (a lower molar cholesterol per phospholipid ratio in high compared to low metastatic melanoma cells) [25]. Besides a reduction, the redistribution of cholesterol in the plasma membrane also influences the CH_2-stretch ratio. When cholesterol is redistributed, resulting in rafts, lipid regions containing more than 45% cholesterol, the average plasma membrane stabilizing cholesterol concentration per area decreases, leading to more disordered phospholipids [23]. This suggests that the membrane of severe, highly metastatic, melanoma cells is more disordered than that of less dangerous melanomas. The CH_2-stretch ratio variations measured between the five individual 1.5 mm diameter spots on the 15 min cisplatin exposed sample slide could be related to the initial uptake of cisplatin in the cell membrane. After 30 min exposure there was no significant CH_2-stretch ratio difference measured between the spots. A decreased CH_2-stretch ratio arises when the membrane lipids are more ordered. This is the case when there is an increase in membrane stabilizing agents stretching the carbon-carbon chain and/or the presence of tightly packed lipid rafts [118].

4.5 Conclusions

In conclusion, a measuring method to distinguish between normal and malignant cell types without the use of elaborate, time consuming, labelling and staining techniques has been presented. This method comprises of a four-wavelength mid-infrared absorbance measurement with which the CH_2-stretch ratio of biological cells can be derived.

The CH_2-stretch ratio based cell discrimination method as additional tool for the diagnoses of suspicious tissues could improve the accuracy of the staging of these tissues. The CH_2-stretch ratio measured from defined cell lines and derived from published IR absorption spectra of clinical human samples show statistical significant and well detectable differences for tumorous compared to normal tissues.

Measurement results of normal epithelial kidney cells exposed to MβCD indicate that an increase in CH_2-stretch ratio arises when there is a decrease in, or redistribution of, the membrane stabilizing agent cholesterol. From the measurement results of Zwielly et al. it can be concluded that cisplatin resistant GA melanoma cells have a higher CH_2-stretch ratio compared to non-resistant GA melanoma cells [73]. This suggests that CH_2-stretch ratio as indicator for tumour cells can also be used to distinguish certain drug resistant and non-resistant tumour cells. The presented measurement results of cisplatin exposed melanoma cells showed a significant decrease in CH_2-stretch ratio of three different melanoma cell lines exposed to cisplatin. This decrease in CH_2-stretch ratio arises due to tightly packed inner-membrane lipid regions to form pores when cells are in apoptosis. This means that CH_2-stretch ratio as indicator for tumour cells can also be used to distinguish certain drug resistant and non-resistant tumour cells.

Chapter 5

The CH_2-stretch ratio of Suspended Mammalian Cells

Instead of determining the CH_2-stretch ratio of dried cells on IR transparent CaF_2 (calcium-fluoride) slides, in this chapter, a method is investigated that allows measurements of cells suspended in PBS (phosphate-buffered-saline). This method reduces the sample preparation time from 7 - 9 hours to only 30 min and allows at-line measurements, keeping the cells alive. Also, it will be investigated whether the CH_2-stretch ratio of suspended cell samples differ compared to that of dried cell samples.

5.1 Introduction

In the previous chapter (CH 4), the potential of the CH_2-stretch ratio to distinguish tumour cells from normal cells has been shown. The removal of the membrane stabilizing agent cholesterol and the influence of tightly packed lipid regions in the inner cell membrane yielded significant CH_2-stretch ratio changes. The preparation time of the sample slides to obtain a cell monolayer attached to infrared transparent calcium-fluoride slides took approximately 7 to 9 hours. The slides also had to be dried to prevent the strong influence of water on the infrared light absorbance signal. In this section a different approach will be investigated to discriminate cell types. Instead of measuring the CH_2-stretch ratio of dried samples, a faster method allowing the measurement of living suspended mammalian cells in microfluidic chips has been designed and realised.

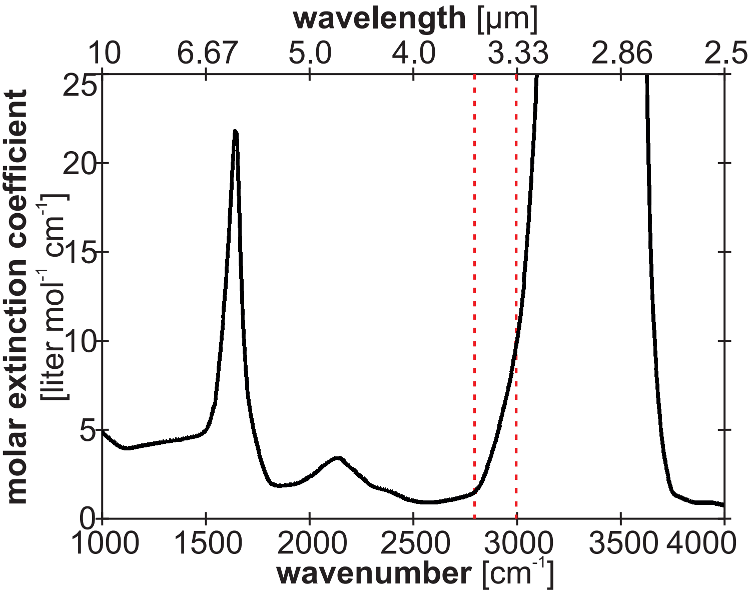

Figure 5.1: The molar absorptivity of water in the spectral range 1000 - 4000 cm^{-1} at 25°C [119]. The region of interest, required for the determination of the CH_2-stretch ratio, is located between the two dashed lines. In this region, the highest extinction takes place at the wavenumber 3000 cm^{-1}.

5.2 Chip design and fabrication

5.2.1 Optimal chip height

While for CH_2-stretch measurements of dried cells an empty CaF_2 slide was used as reference, for suspended cell measurements the reference was a sample chamber filled with PBS. In suspension, epithelial kidney and melanoma cells have a diameter of about 15 µm. Therefore, a chamber height of about 20 µm was chosen. In a lower chamber cells could easily clog, preventing an even distribution throughout the sample chamber. A larger chamber height results in a transmittance signal too low to detect due to strong IR absorbance of water. In order to determine if the height of 20 µm still allows to conduct valid IR transmittance measurements, the absorbance of water is considered. The molar extinction coefficient of water in the wavelength range between 2.5 and 10 µm (Fig. 5.1) has been used to calculate (Eq. 2.2) the % IR transmittance at different optical path lengths (depicted in Fig. 5.2) [119].

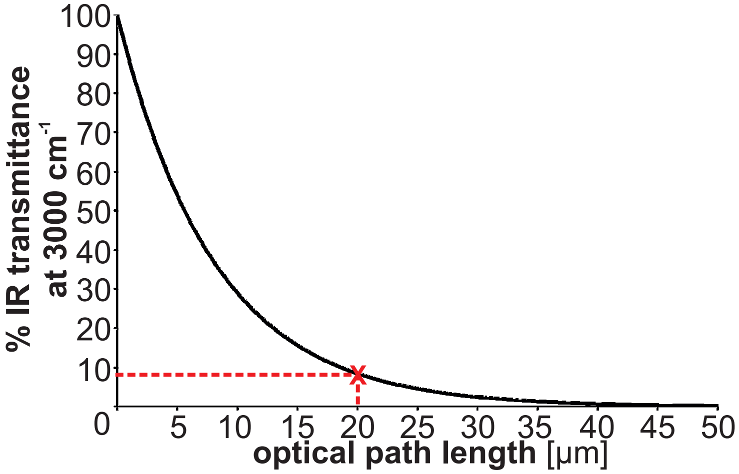

Figure 5.2: The optical path length and % IR transmittance of water at 3000 cm^{-1}. At an inner chamber height of 20 µm, there is still enough transmitted IR light (almost 10%) to conduct valid IR absorbance measurements on suspended cells with a diameter of approximately 15 µm.

As can be seen in Fig. 5.2, a sample chip with an inner chamber height of approximately 20 µm allows a 10% IR transmittance through a pure water layer. In order to test the feasibility of suspended cell measurements, experiments with test chambers have been carried out. These chambers were composed of two 22 x 22 x 0.14 mm^3 borosilicate glass microscope cover slides and 75 µm Teflon or 58 µm Scotch tape spacers. The two sandwiched SiO_2 slides were glued together, filled with H_2O, and sealed.

For both the 58 and 75 µm inner height chambers, the IR transmittance at the wavelength of 3.33 µm was too low to detect by the photodiode. Therefore, a test chip with a gradually increasing thickness was fabricated by sandwiching two glass slides with a strip of tape placed at only one side. The maximum water layer thickness transmitting sufficient IR light emitted by the LEDs to be detected by the photodiode was found by determining the chip position along the gradually increasing thickness. This position is where a minimum current-to-voltage amplified photodiode signal of 150 mV was measured. This minimum voltage was acquired for a 21 µm water layer at the 3.33 µm wavelength. The transmittance values at the specific functional spectral points in the 3.33 - 3.57 µm wavelength region are given in Table 5.1.

From the previously reasoned, calculated, and measured inner cham-

Table 5.1: IR transmittance through a 21 µm thick water layer at specific functional spectral points in the 3.33 - 3.57 µm wavelength region.

Functional group	Wavenumber [cm^{-1}]	Wavelength [µm]	Transmittance [%]
Base point	3000	3.335	7
CH_3 antisymmetric	2958	3.385	17
CH_2 antisymmetric	2923	3.415	24
CH_3 symmetric	2871	3.485	45
CH_2 symmetric	2852	3.510	50
Base point	2800	3.565	65

ber heights allowing IR absorbance measurements of suspended biological cells, the optimal chamber height was found to be 20 µm.

5.2.2 Chip layout and material

The sample chip consists of two sandwiched, 1 mm thick, infrared transparent CaF_2 wafers with in between a fluidic chamber structure made out of the negative photoresist SU-8. CaF_2 was selected as base material because of its high (over 95%) transmittance properties in the IR wavelength region of 3.3 to 3.6 µm [120]. The fabrication process of chips consisting of CaF_2 as a substrate and SU-8 fluidic structures was already developed and utilized in-house [121–123]. The chamber layout was designed in such a way that the dead volume when filling the chip was kept to a minimum. A single chip consists of three equal sample chambers with an optical window of 3.5 mm in diameter, large enough to allow measurements at multiple different 1.5 mm diameter sample spots. In order to prevent the water fraction of the cell suspension to evaporate during measurements, the 600 µm in diameter inlet and outlet holes were sealed with PDMS (polydimethylsiloxane) strips. With a diameter of 3.5 mm and an inner height of 20 µm, the obtained chamber volume was approximately 0.3 µL. A layout of the chip is depicted in Fig. 5.3.

5.2.3 Chip fabrication

The fabrication of the infrared transparent CaF_2 sample chip consists of multiple steps (see Fig. 5.4):

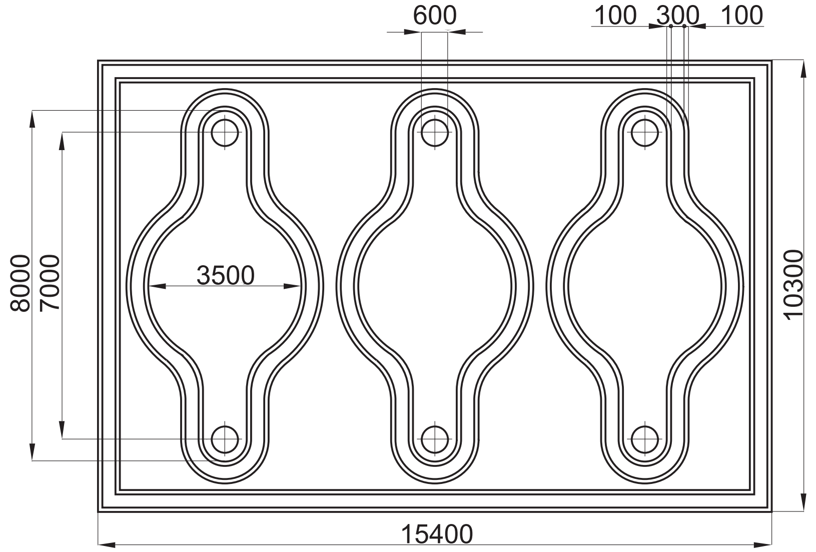

Figure 5.3: Schematic representation of the 15.4 x 10.3 mm^2 IR transparent sample chip. A single chip comprises of three identical chambers, with an optical window of 3.5 mm in diameter and 20 µm chamber height. It allows measurements at four different 1.5 mm diameter sample spots in each chamber.

The surface of the wafers was cleaned by immersion in 10% RBS-50 (a non-foaming liquid cleaning agent containing alkaline) in an ultrasound bath.

Top wafer, SU-8 deposition and patterning: On the top CaF_2 wafer the SU-8 channel structure was created by spinning SU-8 photo resist in three consecutive steps: 200 rpm for 8 s, 1000 rpm for 10 s, and 4700 rpm for 50 s. A soft-bake step at 95°C for 30 min, a 50 s UV-exposure through a mask (a Suess MA 150 was used to align the mask on the wafer), followed by a 90°C, 10 min post-exposure-bake step, yielded a structure of approximately 18 µm in height on top of the wafer, consisting of unexposed SU-8 enclosed by UV-exposed SU-8 side walls (Fig. 5.4a and b).

Bottom wafer, SU-8 deposition and patterning: The channel on the bottom wafer was structured by spinning SU-8 resist, diluted 1.5 : 1 with gammabutyrolactone, at 4500 rpm for 40 s. A soft-bake step at 95°C for 20 min, a 20 s UV mask exposure, and a post-exposure step at 90°C for 10 min, yielded a 5 µm high structure. By developing the SU-8 with PGMEA for 60 s, the unexposed SU-8 was removed and yielded a structure height of 3.4 - 3.6 µm for the exposed SU-8 walls. Afterwards, the wafer was cleaned by rinsing with isopropanol (Fig. 5.4a and b).

Metal deposition and patterning: A 1.2 µm thick Cu (copper) layer was vapour deposited on the post-exposed SU-8 layer of the top CaF_2 wafer by utilizing a Balzers BAK-550 evaporation unit. On top of the Cu layer AZ4512, a positive photo-resist was deposited by spinning at 4000 rpm for 40 s by being soft-baked at 60°C for 5 min (Fig. 5.4c).

The final photolithography step to expose the photo-resist layer on top of the Cu layer took 6 s. Afterwards, a spray-development for 15 s with AZ826 MIF was performed in order to remove only the exposed AZ4512 photo-resist. The Cu layer was patterned by a 3 min etching step in 20 % potassium peroxydisulfate ($K_2S_2O_8$). The photo-resist layer was removed with a 5 % potassium hydroxide (KOH) solution (Fig. 5.4d). The final development step of the SU-8 channel structure was done by immersion in propylene glycol monomethyl-ether-acetate (PGMEA) for 2.5 min, followed by rinsing with isopropanol (Fig. 5.4e).

After optical inspection of the channel structure, the remaining Cu was removed by rinsing in a 20 % $K_2S_2O_8$ solution for 5 min, followed by rinsing with deionized H_2O (Fig. 5.4f).

Inlets and outlets drilling: The inlets and outlets of the chips, 600 µm in diameter, are located on the bottom wafer. To prevent CaF_2 fragments entering the chip during the drilling, a protective AZ4512 layer was deposited by spin coating at 3000 rpm for 40 s and baking at 60°C for 10 min. After drilling, the photo-resist layer was removed by rinsing with a 5 % KOH solution.

Wafer bonding: The top and bottom wafers were aligned and bonded using an EVG501 wafer bonder. The chamber was evacuated and the wafers were bonded by applying a force of 500 N while exposed to a variable temperature regime. The soft SU-8 (a thermoplast) from the top wafer filled the gaps by capillary forces when heated during wafer bonding [124]. At 150 - 200°C, unexposed SU-8 is thermally cross-linked, serving as an adhesive layer between the wafers (Fig. 5.4g and h).

Wafer dicing: The individual chips were cut from the bonded wafers by applying a DAD3220 dicing saw with a 200 µm thick diamond blade. By placing the bonded wafers with the side of the drilled inlets on an adhesive tape, CaF_2 splinters were prevented to enter the channel structure via the drilled inlets.

The inner height of the individual chambers were measured optically by using a Filmetrics F20-UVX thin film analyser. The obtained chamber

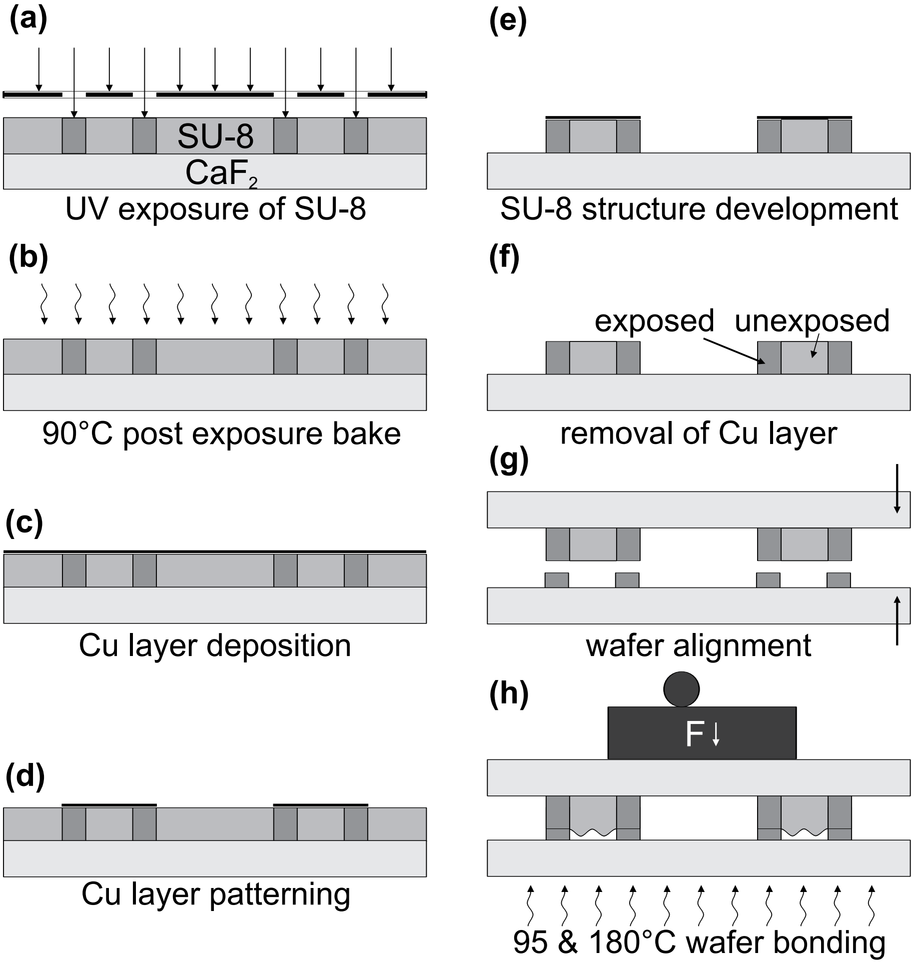

Figure 5.4: Fabrication process of the infrared transparent sample chip.

height, varying between chips, was 19.1 to 22.6 µm. Depending on the position of the wafer, the inner height varied. The chamber height was larger near the the centre compared to the edge of the wafer, which was caused by variances in thickness of the spin-coated photo-resist. In Fig. 5.5, a finalized chip is depicted.

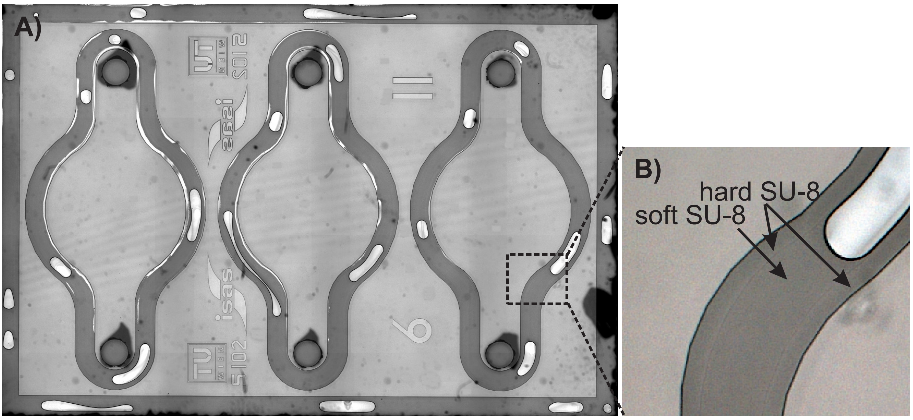

Figure 5.5: Photograph of the 11 x 15 x 2 mm^3 microfluidic sample chip consisting of two bonded infrared transparent calcium-fluoride wafers with in between a 20 µm high SU-8 channel structure. Each chip consists of three sample chambers with a 3.5 mm diameter measurement window. The exposed (hard) SU-8 is used to structure the chamber, the unexposed (soft) SU-8 to improve the wafer bonding process.

5.3 Materials and methods

5.3.1 Cell lines and sample preparation

The epithelial kidney cell lines MDCK and Caki-1 were cultivated in DMEM supplemented with 2 mM L-glutamine, 10% FCS, and antibiotics (100 units/mL penicillin, 100 µg/mL streptomycin, and 0.25 µg/mL Amphotericin B), which were all obtained from Lonza Bioscience, Germany. The human melanoma cell lines 518A2 (a gift from Dr. Peter Schrier, LUMC, Leiden, Netherlands), M14 (a gift from Dr. Soldano Ferrone; Dept. of Immunology, University of Pittsburgh, and A375 were maintained in RPMI 1640 medium (Biochrom AG, Germany). Media were supplemented with 10% fetal calf serum and 1% antibiotics. All cell lines were cultured in a humidified atmosphere containing 5% CO_2 and 95% ambient air at 37°C. The cell cultures were free of mycoplasma and pathogenic viruses. For the preparation of cell suspensions, the epithelial kidney cells were trypsinized for 10 and 2 min at 37°C for respectively MDCK and Caki-1 cells and washed in PBS. The melanoma cells were detached from the cell culture flask by utilizing a cell scraper. When required, the cell suspension concentration was lowered by dilution in PBS or increased by a centrifugation.

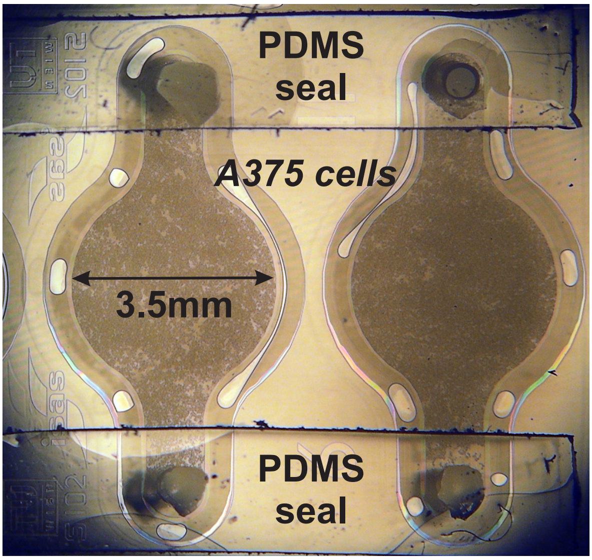

Figure 5.6: Two chambers containing A375 melanoma cells suspended in PBS, with the inlets and outlets sealed with PDMS strips.

The sample was loaded into 0.3 μL chambers by pipetting 1 - 2 μL cell suspension onto the inlets. By applying a vacuum at the outlet, the sample was forced into the chamber.

5.3.2 Sensor adjustments

Dried sample slides can easily be positioned vertically in the sensor system. For suspended cells, this will result in cell sedimentation, changing the amount of cells per area when measuring their IR absorbance. The easiest way to prevent this cell sedimentation is by positioning the sample chip horizontally on top of the 1.5 mm diameter aperture. This was realised by changing the optical pathway by placing an IR turning mirror between the IR beam splitter and IR beam focus lens (see Fig. 5.7).

5.3.3 Sensor Settings

The LEDs were set to pulsate for 12 μs at a repetition rate of 2 kHz, 2.4 % duty cycle. Of each cell sample, the CH_2-stretch ratio of five 1.5 mm diameter spots were averaged. Each of the five spots were measured 500 - 1250 times. The specific settings are depicted in Table 5.2.

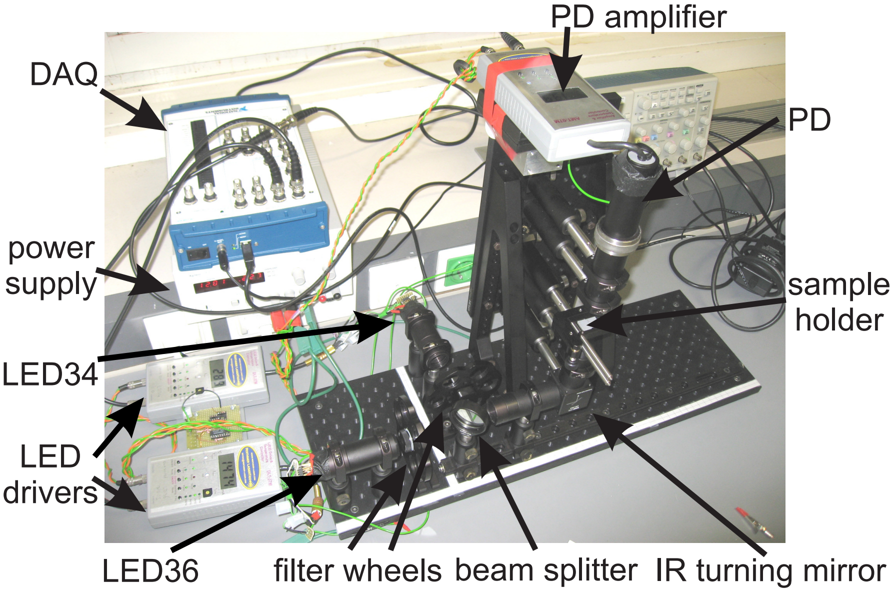

Figure 5.7: Adjusted sensor system. Compared to the previous setup, the optical path is now shifted 90°upwards by an IR turning mirror, allowing the sample to be positioned horizontally instead of vertically.

Table 5.2: LED and photodiode settings.

	LED 3.4 µm	LED 3.6 µm	Photodiode 3.4 µm	
current	1070	1470	-	mA
temperature	10.4	10.7	20.7	°C

5.3.4 Measurement protocol

The currents of the LED drivers were set in such a way that at the 3.33 µm wavelength, where water has the highest IR absorbance (in the 3.33 - 3.57 µm region, see Fig. 5.1), the photodiode current-to-voltage amplified output signal was about 4 V for an empty CaF_2 sample chip. This voltage is just beneath the clipping voltage of the photodiode, while for a chip filled with H_2O the attenuated signal was approximately 0.4 V. As reference, the chambers of a sample chip were filled with PBS and their IR absorbance was recorded. Consequently, PBS was removed and the chambers were filled with cell suspension. Of each sample the IR absorbance to derive the CH_2-stretch ratio of five spots were measured. Since the inner height of the three chambers on a single chip varied slightly (less than 0.5 µm), the IR absorbance of the reference and sample were measured in the same chamber. After the absorbance measurements, the cells were removed from the chip by applying a vacuum and rinsing with a cleaning solution containing sodiumhypochloride to dissolve the remaining biological sample fraction.

5.3.5 Statistical analysis

Mann - Whitney tests were performed to test for statistically significant differences between the CH_2-stretch ratios of the measured cell types. These statistical tests allow the comparison of non-normal distributed ratio values by ranking the individual measurement results from low to high values [125]. The null hypothesis states that there is no significant difference between the groups, and is certainly sufficient to accept for $p \geq 0.05$.

5.4 Results and discussion

5.4.1 Epithelial kidney cells

Two MDCK and three Caki-1 cell samples were prepared and their IR absorption measured in order to derive and compare their CH_2-stretch ratios. Of each cell line, samples were prepared from the same culture, but of different cell passages (1 - 2 weeks in between). Per sample five spots were measured. The two MDCK cell samples yielded a CH_2-stretch ratio of 0.45 ± 0.01 and 0.44 ± 0.01, respectively. Malignant Caki-1 measurements yielded CH_2-stretch ratios of 0.49 ± 0.01, 0.48 ± 0.01, and 0.48 ± 0.02 (see

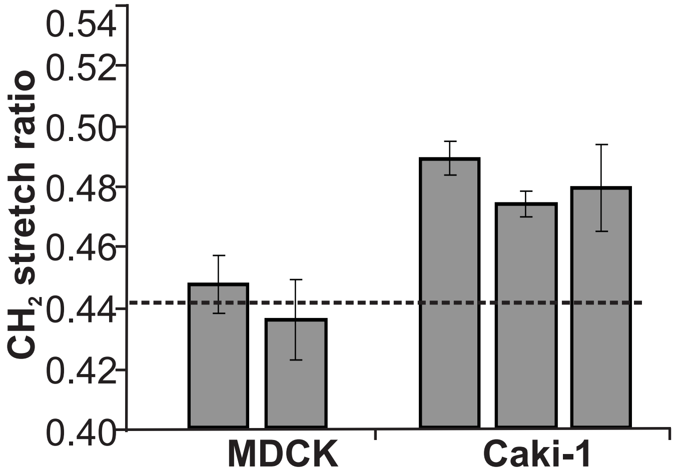

Figure 5.8: Sensor CH_2-stretch ratio measurement of normal MDCK (mean ± standard deviation, 0.45 ± 0.01, and 0.44 ± 0.01) and malignant Caki-1 (0.49 ± 0.01, 0.48 ± 0.01, and 0.48 ± 0.02) epithelial kidney cells suspended in phosphate-buffered-saline. Bars represent means ± standard deviation per cell passage (each bar comprises the average CH_2-stretch ratio of 5 spots with 500 - 1250 measurements per spot).

Fig. 5.8). The CH_2-stretch ratio difference measured between the two cell lines might be lower than that for the dried measurements, but is still statistical significant. A statistical analysis, to determine if there is a significant difference between the CH_2-stretch ratio of the individual cell lines, has been made by performing a Mann - Whitney test for non-normal distributed datasets. The null hypothesis is that both groups have the same CH_2-stretch ratio. The test yielded a probability $P = 2.8 \times 10^{-6}$, indicating that the CH_2-stretch ratio of the individual cell lines have a statistical significant difference.

5.4.2 Melanoma cells

The CH_2-stretch ratio measurement results of three in PBS suspended melanoma cell lines are depicted in Fig. 5.9. Of each cell line different cell passages (1 - 2 week in between) yielded the same CH_2-stretch ratio. This shows the reproducibility of the measurement method. Between the melanoma cell lines small statistical significant CH_2-stretch ratio differences have been measured. Statistical analysis results of Mann - Whitney

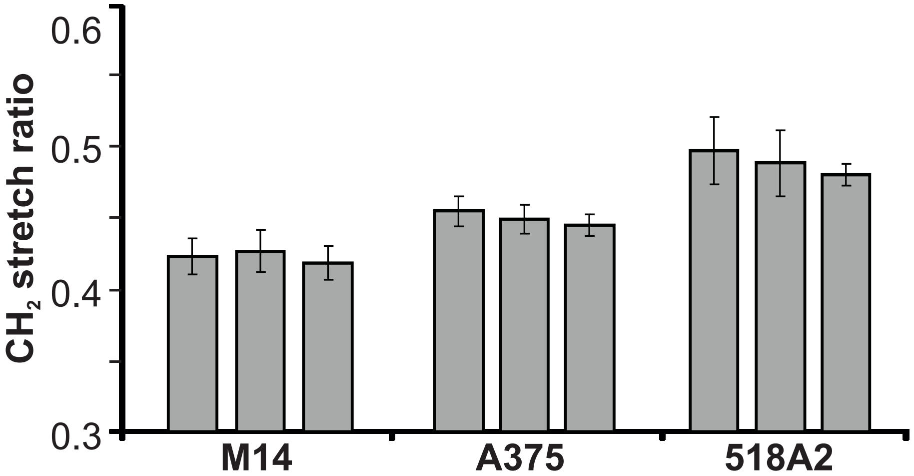

Figure 5.9: Sensor CH_2-stretch ratio measurement of three melanoma cell lines, M14 (mean ± standard deviation, 0.42 ± 0.01, 0.43 ± 0.02, and 0.42 ± 0.01), A375 (0.45 ± 0.01, 0.45 ± 0.01, and 0.45 ± 0.01), and 518A2 (0.50 ± 0.02, 0.49 ± 0.02, and 0.48 ± 0.01), suspended in phosphate-buffered-saline. Bars represent means ± standard deviation per cell passage (each bar comprises the average CH_2-stretch ratio of 5 spots with 500 - 1250 measurements per spot).

tests between the individual cell lines were significant $P \leq 5.0 \times 10^{-7}$; indicating that the CH_2-stretch ratio differences between the individual cell lines were statistical significant.

Compared to previously conducted CH_2-stretch ratio measurements on dried samples, suspended cell measurements all yielded lower stretch ratio values. Suspended in an aqueous solution, hydrogen bonds between the cell membrane proteins at amino acid-containing OH side groups stabilize the membrane lipid structure [126]. Therefore, the difference in CH_2-stretch ratio between dried and suspended cells is most likely due to changes in the hydration level of proteins. Pevsner et al. have shown that peak shifts in CH_2-symmetric and antisymmetric stretches due hydration level do no occur [127]. IR absorbance spectra of dried and suspended M1 rat fibroblast cells presented by Mourant et al. showed that the CH_2-stretch ratio (functional absorbance at 3.51 / 3.42 µm) of suspended M1 cells is lower compared to that of dried cells (0.45 and 0.51, respectively) [128].

5.5 Conclusions

The 7 to 9 h cell preparation step was avoided by suspending the cells in PBS and directly filling them into a sample chip, allowing at-line measuring of the CH_2-stretch ratio of viable mammalian cells. Overall preparation times were reduced to about 30 min. Measurements of cell samples with different cell passage numbers, as well as measurements with different chips (hence varying chamber heights) yielded similar results. Significant differences in CH_2-stretch ratio between dried and suspended cell samples have been detected. For Caki-1 cells the measured CH_2-stretch ratio was 0.73 for dried cells and 0.48 for cells suspended in PBS (for MDCK cells the CH_2-stretch ratio values measured were 0.47 and 0.44, respectively).

The CH_2-stretch ratio differences measured for normal versus carcinoma epithelial kidney cell lines and between three melanoma cell lines were statistical significant, indicating that it is feasible to distinguish suspended cell lines based on their CH_2-stretch ratio.

Chapter 6

Label-Free Cell Separation Devices

In previous chapters the research was focussed on a label-free identification method for primary "solid" tumours. During tumour progression, there is the chance that tumour cells develop the ability to metastasise, invading other organs or other regions of the body by moving through the blood stream or lymph system. To allow IR absorbance measurements on cells suspended in blood or lymph fluid, the suspicious cells should first be separated and harvested from body fluids containing contaminants, such as non-viable cells, cell debris, and bacteria. The research described in this chapter is focussed on the label-free separation of mixtures of different cells, in specific the separation of viable mammalian cells from non-viable cells, cell debris, and bacteria.

The separation principle is based on travelling wave dielectrophoresis (twDEP), which, compared to the other principles, allows higher electric field strengths, and the use of a travelling electric field instead of a static electric field. The sample mix introduced at one side of the channel is exposed to a travelling electric field created by exciting the electrodes positioned along the microchannel to phase-shifted AC voltages (section 6.5).

In the next sections an overview of commonly used and state of the art cell separation techniques are described. This is followed by a self-designed and realised dielectrophoretic based cell separator.

6.1 Introduction

Viable biological cells grown attached to a surface can easily be separated from cell culture debris and bacterial contamination by washing with PBS (phosphate buffered saline) and changing the culture medium. For suspended cells however, this is not an option. All suspended cells should than be identified and separated on a single cell basis. Common techniques to separate suspended viable cells are for example by Fluorescent Activated Cell Sorting (FACS) [56, 129–131] or Magnetic Activated Cell Sorting (MACS) [132, 133]. FACS and MACS both require elaborate labelling steps. Specific antibodies are used to label the cell of interest with a fluorescent tag or a magnetic bead, respectively.

Promising cell separation techniques that do not require labelling are Field Flow Fractionating (FFF), Cellular sieving, and Pinched-Flow Fractionation (PFF). An overview of different continues separation techniques can be found in reference [134]. FFF is based on the combined influence of a laminar flow that transports the sample along a channel and a field orthogonal to the flow. An important factor for a successful gravity based FFF separation is that the particle of interest has to have a density that differs from the other particles and suspending medium [135, 136]. Instead of a gravitation field it is also possible to use an optical field (optical lattice). Here, next to size, the separation is also based on the refractive index of the sample. The interaction between optical lattice and matter depends on a relative polarizability that increases with particle size. By introducing a 3D optical lattice into the fractionation chamber, one type of particle is selectively pushed into the upper flow field [137]. Cellular sieving is based on size, morphology, and deformability differences of cells (ability of a cell to squeeze itself through a hole, e.g. white blood cell moving out of a vein) [138]. PFF is a method for continuous separation of particles and cells based on size differences [139, 140]. A laminar sample and buffer stream are pumped through a narrow "pinched" channel section before entering a broadened section. Due to a higher flow rate of the buffer stream from that of the sample stream particles and cells are pushed against the channel wall in the narrow pinched segment. The larger the particle, the further away its centre of gravity will be from the channel wall, resulting in a particle size gradient that will be expanded in the broadened channel section. When different outlets are placed in the broadened section, size sorted particles can be collected [141]. With this technique it should theoretically be possible to separate red blood cells from whole blood, but, so far, no real biological cell applications have been presented in literature.

All these label-free separation techniques depend on differences in cell size and are, unfortunately, not optimized to be utilized for the separation of different cells, e.g. viable from non-viable cells or suspended-grown cells from bacteria. A phenomenon that does not require elaborate labelling steps or a difference in particle density for separation is dielectrophoresis, defined as a motion of polarizable particles exposed to a non-uniform electric field [142, 143]. Many dielectrophoretic separation devices require accurate hydrodynamic focusing [144, 145] or multiple frequencies [146–148] to position the sample into the separation section of the microchannel. A planar interdigitated electrode array placed at an angle of 11° to the direction of flow has been utilized to separate red and white blood cells [149]. This separation method is based on lateral negative DEP forces acting on the blood cells. The use of electrode pairs positioned on the top and bottom of the microfluidic channel have been shown, which require highly accurate alignment steps during the fabrication process [150, 151]. Also, a non-continuous sample separation device based on travelling wave dielectrophoresis (twDEP) has been shown where the electrodes were positioned perpendicular in the microfluidic channel [152]. Another technique, deterministic lateral displacement, has been shown for different micrometer sized polystyrene particles and fungal spores [153]. Also, the combination of deterministic lateral displacement and dielectrophoresis has been presented for 2 - 6 µm polystyrene particles [154]. This separation method is based on fluid flow through a periodic array of obstacles. By varying the gap or the tilt angle and placing multiple obstacles arrays in sequence, particle separation based on size can be achieved.

In previous work conducted at the ISAS institute a continuous separation method and device has been realised, which is based on positive and negative DEP without the need of accurate sample prefocusing [155–157]. Viable Jurkat cells experiencing positive dielectrophoresis (pDEP) were separated from a mix containing also cell debris and non-viable cells. The viable cells were being guided towards and dragged along the edge of a planar electrode.

The research described in this chapter is focussed on the label-free separation of mixtures of different cells, e.g. the separation of viable mammalian cells from non-viable cells and bacteria. To realise this, a dielectrophoretic separator has been designed and realised.

6.2 Dielectrophoresis theory

Dielectrophoresis, the motion of polarizable particles exposed to a non-uniform electric field, first described by Pohl in 1951 [142], depends on the permittivity and conductivity of the particle and surrounding medium. If the

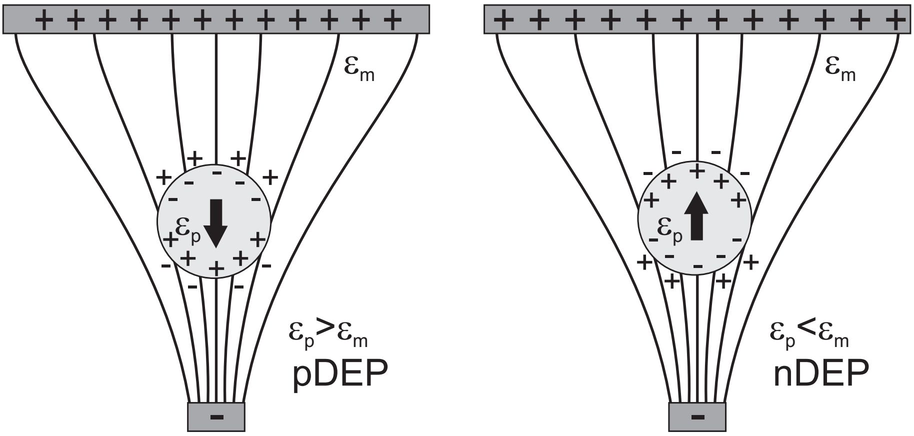

Figure 6.1: When a particle is exposed to an inhomogeneous electric field, a dipole can be induced. The direction depends on the electrical polarizability of the particle and that of the surrounding medium. The particle moves towards the higher field region when its polarizability is higher than that of the surrounding medium: positive DEP. The particle is repelled from the high intensity field moving to the lower field region when its polarizability is lower than that of the surrounding medium: negative DEP.

electrical polarizability of the particle is larger than that of the surrounding medium, the particle moves towards the higher field region, which is called positive DEP (pDEP). When the polarizability of a particle is lower than that of the surrounding medium, the particle is repelled from the high intensity field moving to the lower field region, which is called negative DEP (nDEP) (see Fig. 6.1).

The dielectric motion is determined by the magnitude and polarity of the charges induced in a particle by the applied field. The polarizability parameter as a function of the frequency of the applied field depending on dielectric properties of the particle and surrounding medium is called the Clausius-Mossotti factor f_{cm}. The basic dielectrophoresis equation approximation for first order dipoles is as follows:

$$\vec{F}_{DEP} = 2\pi r^3 \varepsilon_m \Re_e \left| f_{cm}(\omega) \right| \vec{\nabla} E_{rms}^2 \tag{6.1}$$

The DEP force vector is directed along the gradient of the electric field intensity and the DEP force depends on the magnitude of the Clausius-

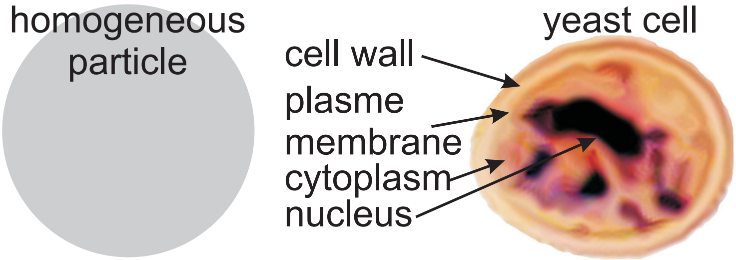

Figure 6.2: Homogeneous particles have a constant Clausius-Mossotti factor (real part) over a broad frequency range. This is not the case for biological cells consisting of multiple compartments.

Mossotti factor:

$$f_{cm} = \frac{\varepsilon_p - \varepsilon_m}{\varepsilon_p + 2\varepsilon_m} \tag{6.2}$$

where ε is the permittivity of particle p and medium m, r the particle radius, and $\vec{\nabla}\mathrm{E}^2$ the gradient of the squared electric field with angular frequency ω.

Homogeneous dielectric particles have a constant Clausius-Mossotti factor over frequency. For a homogeneous polystyrene particle p suspended in deionized water m with relative permittivity ε_{r} of respectively $\varepsilon_{\mathrm{r,p}} = 2.55$ and $\varepsilon_{\mathrm{r,m}} = 78$ the Clausius-Mossotti factor is calculated as follows:

$$f_{cm} = \frac{2.55\ -\ 78}{2.55\ +\ 2\ \times\ 78} = -0.48 \tag{6.3}$$

yielding a DEP force vector pointing towards the lower field gradient direction when being exposed to an inhomogeneous electric field. Biological cells however are inhomogeneous, not perfect spherical, and consisting of different compartments and layers each with different electrical properties. This makes the DEP force equation more complex, but as a separation technique very interesting. In the case of yeast cells for example, all the layers and compartments such as cell wall, plasma membrane cytoplasm, and nucleus should be taken into account (see Fig 6.2).

A way to approximate the dielectric behaviour of cells is by using the layered dielectric shell model. With this model an equivalent dielectric permittivity for multi-layered particles can be calculated. An example of how to calculate this equivalent factor for a three layered particle is described by Eq. 6.4 and depicted in Fig. 6.3.

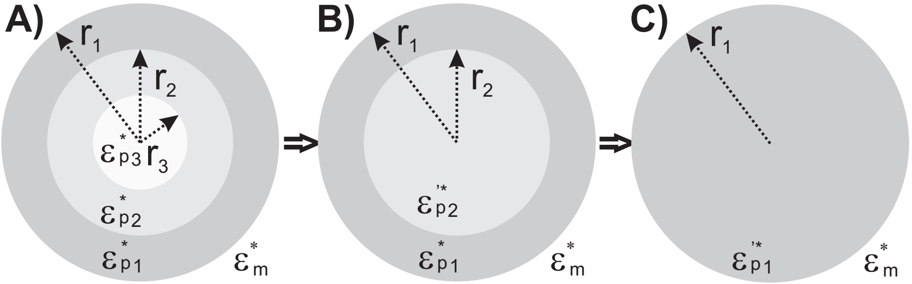

Figure 6.3: Multi-shell model. A particle consisting of three dielectric shells can by repeated simplification be replaced by an equivalent homogeneous particle of radius r_1 and permittivity $\varepsilon_{p1}^{'*}$.

$$\varepsilon_{p2}^{'} = \varepsilon_{p2}\left\{\frac{a^3 + 2\left(\frac{\varepsilon_{p3}-\varepsilon_{p2}}{\varepsilon_{p3}+2\varepsilon_{p2}}\right)}{a^3 - \left(\frac{\varepsilon_{p3}-\varepsilon_{p2}}{\varepsilon_{p3}+2\varepsilon_{p2}}\right)}\right\} \quad \text{, with} \quad a = \frac{r_2}{r_3} \tag{6.4}$$

$$\varepsilon_{p1}^{'} = \varepsilon_{p1}\left\{\frac{b^3 + 2\left(\frac{\varepsilon_{p2}^{'}-\varepsilon_{p1}}{\varepsilon_{p2}^{'}+2\varepsilon_{p1}}\right)}{b^3 - \left(\frac{\varepsilon_{p2}^{'}-\varepsilon_{p1}}{\varepsilon_{p2}^{'}+2\varepsilon_{p1}}\right)}\right\} \quad \text{, with} \quad b = \frac{r_1}{r_2} \tag{6.5}$$

Biological cells are able to transport ions actively and passively over the cell membrane through specialized protein “pores” functioning as ion-channels located in the phospholipid comprising cell membrane [158, 159]. This ionic charge redistribution causes changes in the different cell compartments resulting in electric loss [160].

In the previously described multilayer simplification equation (Eq. 6.4) electric loss is not taken into account. Factors controlling the polarizability of cells with electric loss occurring in the cell interior include conductivity and permittivity of cell walls and membranes, electric double layers associated with surface charges, cell morphologies, and internal structures. Mammalian cells do not contain a cell wall, instead they are surrounded by a thin phospholipid membrane of about 7.5 - 10 nm [161]. This allows the use of the simplified thin-shell model (see Fig. 6.4) where the lipid membrane thickness $\delta = r_1 - r_2 << r_1$. In this case the simplified dielectric model

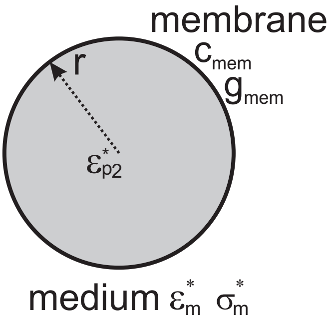

Figure 6.4: Dielectric thin-shell model of a cell surrounded by a thin phospholipid bilayer.

for the effective permittivity can be described by Eq. 6.7:

$$\varepsilon_p^* = \frac{c_m^* r \varepsilon_{p2}^*}{c_m^* r + \varepsilon_{p2}^*} \tag{6.6}$$

and

$$c_m^* = c_m + g_m / j\omega \tag{6.7}$$

where $c_m = \varepsilon_{p1} / \delta$ is the membrane capacitance and $g_m = \sigma_{p1} / \delta$ the membrane transconductance with σ the conductivity (typical membrane capacitance and transconductance values are respectively 10 mF/m^2 and 10 S/m^2 or higher [162]).

The Clausius-Mossotti factor varies as a function of frequency of the applied field and depends on the differences in permittivity and conductivity of the cell compartments. Electric loss of particles can be taken into account by replacing the permittivities described in Eq. 6.2 with their complex counterparts resulting in a frequency depended Clausius-Mossotti factor:

$$\begin{aligned} f_{cm} &= \frac{\varepsilon_p{}^* - \varepsilon_m{}^*}{\varepsilon_p{}^* + 2\varepsilon_m{}^*} \quad \text{, with} \quad \varepsilon^* = \varepsilon - j\left(\frac{\sigma}{\omega}\right) \qquad (6.8) \\ &= \frac{\varepsilon_p - j\left(\frac{\sigma_p}{\omega}\right) - \varepsilon_m + j\left(\frac{\sigma_m}{\omega}\right)}{\varepsilon_p - j\left(\frac{\sigma_p}{\omega}\right) + 2\varepsilon_m - j\left(\frac{2\sigma_m}{\omega}\right)} \\ &= \frac{(\varepsilon_p - \varepsilon_m)(\varepsilon_p + 2\varepsilon_m) + (\varepsilon_p - \varepsilon_m) j \left(\frac{\sigma_p + 2\sigma_m}{\omega}\right)}{(\varepsilon_p + 2\varepsilon_m)^2 + \left(\frac{\sigma_p + 2\sigma_m}{\omega}\right)^2} \\ &\quad + \frac{-(\varepsilon_p + 2\varepsilon_m) j \left(\frac{\sigma_p - \sigma_m}{\omega}\right) + \left(\frac{\sigma_p - \sigma_m}{\omega}\right)\left(\frac{\sigma_p + 2\sigma_m}{\omega}\right)}{(\varepsilon_p + 2\varepsilon_m)^2 + \left(\frac{\sigma_p + 2\sigma_m}{\omega}\right)^2} \end{aligned}$$

In the following section the imaginary part (section 6.5) of the Clausius-Mossotti factor will be investigated for continuous separation purposes. Before the separation experiments could be conducted the rotational and DEP spectra of the to be investigated cell types have been recorded. The cell characterization method is described in section 6.3.

6.3 Cell characterization: DEP and ROT Spectra

Dielectric characterization of individual biological cells can be studied by means of electrorotation (ROT). ROT spectra, rotation speed versus electrical frequency at fixed voltage, can be analysed to estimate fundamental cell properties such as membrane capacitance and conductance. A basic electrorotation chamber consists of a set of miniaturised electrodes driven by polyphase AC voltage waveforms to create a uniform rotating electric field at the centre of the chamber. For typical biological cells in the order of 5 µm in diameter, electric field strengths of 20 V/cm, and frequency range between 100 Hz - 100 MHz, the rotation speeds are in the order of a few revolutions per second [143].

The ROT spectra of cells were obtained by exposing the cells to a rotating electric field (Fig. 6.5) and grabbing frames from captured video files. The cell rotations per time unit were extracted by comparing these video images. Only cells located near the centre of the electrodes and at least four

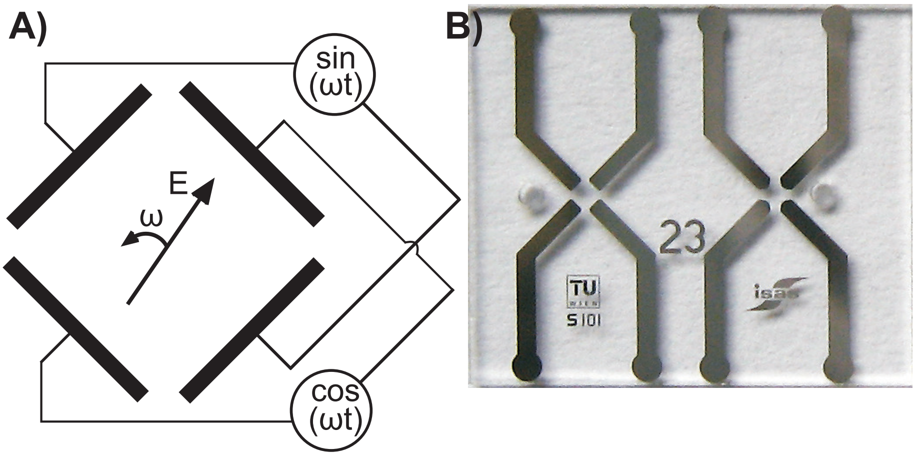

Figure 6.5: **A)** Excitation voltage to create a rotating electric field. **B)** Photograph of a 11 x 13 mm^2 cell characterization chip comprising two quadruple electrode geometries.

cell diameters away from each other were used to avoid the influence of a dipolar field of neighbouring cells [163–165].

ROT spectra f_{ROT}, in revolutions per second, are complex, non-linear functions of the cell and surrounding medium dielectric parameters given by

$$f_{\mathrm{ROT}}(\omega) = -\frac{\varepsilon_{\mathrm{m}} \Im m[f_{\mathrm{cm}}(\omega)] E_0^2}{2\eta} \tag{6.9}$$

where $\varepsilon_m E_0^2 / 2\eta$ is also known as the scaling factor χ. This factor is usually unknown due to uncertain frictional forces and local electric field strength. Unknown parameters are derived by an iterative optimization procedure. This procedure uses the Nelder-Mead simplex optimization provided by Mathworks Matlab to minimize the residual error:

$$Min_{\mathrm{parameters}} \left\{ \sum_i [f_{ROTexp}(i) - f_{model}(i)]^2 \right\} \tag{6.10}$$

where i is a frequency point.

Mammalian cells comprising a phospholipid bilayer membrane can be modelled as a thin-shelled sphere resulting in a ROT spectrum function with five unknown parameters: c_m, g_m, ε_{p2}, σ_{p2}, and the scaling factor χ. Each of the ROT peaks is determined independently by two variables, g_{m} and c_{m} for the low-frequency peak, and σ_{p2} and $\varepsilon_{\mathrm{p2}}$ for the high-frequency peak. Therefore, a complete ROT spectrum can be derived by four and only four parameters. Since the maximum allowed frequency f_{max} of our ROT measurement setup was approximately 4 MHz, the rotation peak in 0° - 90° - 180° - 270°direction was not detectable. Thus, the sensitivity of the ROT spectrum towards $\varepsilon_{\mathrm{p2}}$ and σ_{p2} is very low and their estimation is uncertain [163]. For this reason, the cytoplasmic properties $\varepsilon_{\mathrm{p2}}$ and σ_{p2} were fixed to respectively $90\,\varepsilon_0$ and 0.7 S/m [166] in the optimization step and only c_m, g_m, and χ had to be estimated. By measuring the cross-over frequency f_{co}, an accurate estimation of the three remaining parameters can be made. In this case, the fitting procedure to minimize the error function is:

$$Min_{\text{parameters}}\left\{\sum_i [f_{ROTexp}(i) - f_{\text{cm}_{\text{model}}}(i)]^2 + W\chi\Re_e[\underline{K}_{model}(f_{co})]^2\right\} \tag{6.11}$$

where W is the dimensionless weighting factor which determines the relative emphasis placed on ROT and f_{co} data.
Following the above described protocol different biological cells have been characterized.

Jurkat cells, T-lymphocyte (acute leukaemia) with a diameter of 12 µm, suspended in a 40 mS/m buffer, yielded the following parameters: f_{co} = 130 kHz, c_m = 11 mF/m^2, g_m = 1910 S/m^2, and χ = 0.65.

Nannochloropsis sp., marine algae with a diameter of 2.7 µm, suspended in a 10 mS/m medium, yielded: f_{co} = 350 kHz, c_m = 3.5 mF/m^2, g_m = 4020 S/m^2, and χ = 0.61.

Compared to mammalian cells, yeast cells and bacteria have a much thicker cell wall built of polysaccharides. Therefore, a two-shell model is required, introducing the additional cell wall dielectric properties ε_{p1}, σ_{p1}, and thickness δ.

For yeast cells 4.7 µm in diameter with a cell wall thickness of 150 nm, suspended in a 40 mS/m medium, g_m = 33 mS/m^2, and $\varepsilon_{\mathrm{p1}} = 60\,\varepsilon_0$ (obtained from literature [143, 167, 168]), the derived parameters are: f_{co} = 400 kHz, c_m = 10 mF/m^2, σ_{p1} = 9.1 mS/m, and χ = 0.84.

L. casei, a bacteria from the Lactobacillus genus commonly found diary products are rod-shaped. For simplification, they were assumed to be spherical, 1.2 µm in diameter. When suspended in a 2.3 mS/m medium, a cell wall thickness of 20 nm, g_m = 100 mS/m^2, and $\varepsilon_{\mathrm{p1}} = 60\,\varepsilon_0$ (obtained from literature [143, 167, 169]), the derived parameters are: f_{co} = 250 kHz, c_m = 2.7 mF/m^2, σ_{p1} = 17.8 mS/m, and χ = 1.21.

The DEP and ROT spectra of Jurkat cells at different medium conductivities σ_m are depicted in Fig. 6.6.

As can be seen, the cross-over frequency is shifted linearly towards higher frequencies when increasing the medium conductivity. The peaks depicted in the normalized ROT spectra plots correspond with the maximum rate of variation of the normalized DEP spectra, e.g. of the four different media conductivities, Jurkat cells suspended in medium with conductivity of σ_m 40 mS/m yielded the largest difference (y-axis).

6.4 Chip fabrication

The Silicon - SU-8 - Glass chips described by Kostner et al. [155] are bonded and, therefore, cannot be cleaned properly by removing the cover slide. Especially when using dense concentrations of biological samples suspended in a sugar based medium, channel clogging could not be prevented. Hence, a chip design allowing easy cleaning by the removal of the cover slide was designed.

The fabrication of DEP characterization device and travelling wave DEP separator (Section 6.5) built out of glass - PDMS, consist of multiple steps: The bottom layer of the DEP device was made from a 4-inch, 500 µm thick glass wafer. The electrodes were structured using a lift-off process comprising the following steps (see Fig. 6.7 left column): AZ5214, an image reversal photoresist, was spin-coated on the glass wafer and pre-baked at 107°C for 5 min. The photoresist layer was exposed to UV through a mask containing the electrode pattern. A 120°C at 2 min post-bake step and flood exposure yielded an inversed electrode pattern made out of photoresist. A 50 nm under coating titanium layer and 100 nm platinum layer were vapour deposited. The glass wafer comprising the electrode structure was obtained by the removal of the photoresist covered by the metal layer. After drilling 0.6 mm diameter inlets, the fabricated glass wafer was cut to obtain the single devices (see Fig. 6.13).

The fabrication steps of the PDMS top layer with integrated channel structure are depicted in Fig. 6.7 (right column). A silicon wafer was used as base material. On this wafer a photoresist SU-8 was spin-coated with an undercoating titanium layer (at 500 rpm for 16 s, at 2000 rpm for 15 s, and at 3200 rpm for 40 s). The achieved thickness of the SU-8 layer was approx-

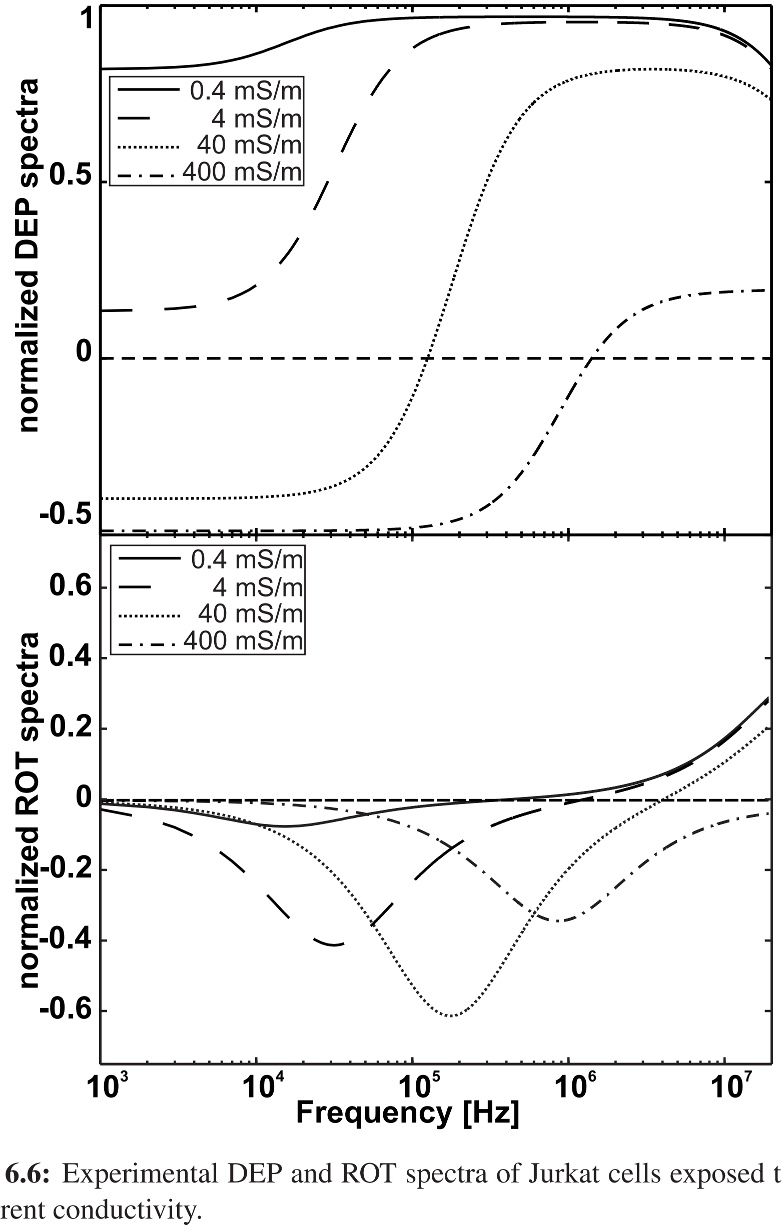

Figure 6.6: Experimental DEP and ROT spectra of Jurkat cells exposed to media of different conductivity.

imately 30 µm. This layer was soft-baked at 95°C for 45 min on a heated plate. The photoresist layer was exposed to UV through a mask, containing the channel pattern. A 90°C post-bake exposure for 30 min was applied to cross-link the UV irradiated SU-8. By dissolving the UV unexposed photoresist with the solvent PGMEA and a 200°C hard-bake step for 1 h, the mould was finalised.

The top layer with channel structure was obtained by pouring vacuum outgassed PDMS (Sylgard 184) on the silicon-SU-8 mould. The PDMS layer was cured at 70°C for 1 h. A clamped foil was used to flatten the top surface. The single PDMS devices were cut out of the wafer with a scalpel.

After cleaning both the electrode containing glass chip and the PDMS layers with ethanol and deionized water, the microchannel and electrodes were aligned (for proper alignment marks were provided on the glass and PDMS cover layer). The PDMS layer adhered to the glass surface without any need of additional fixation.

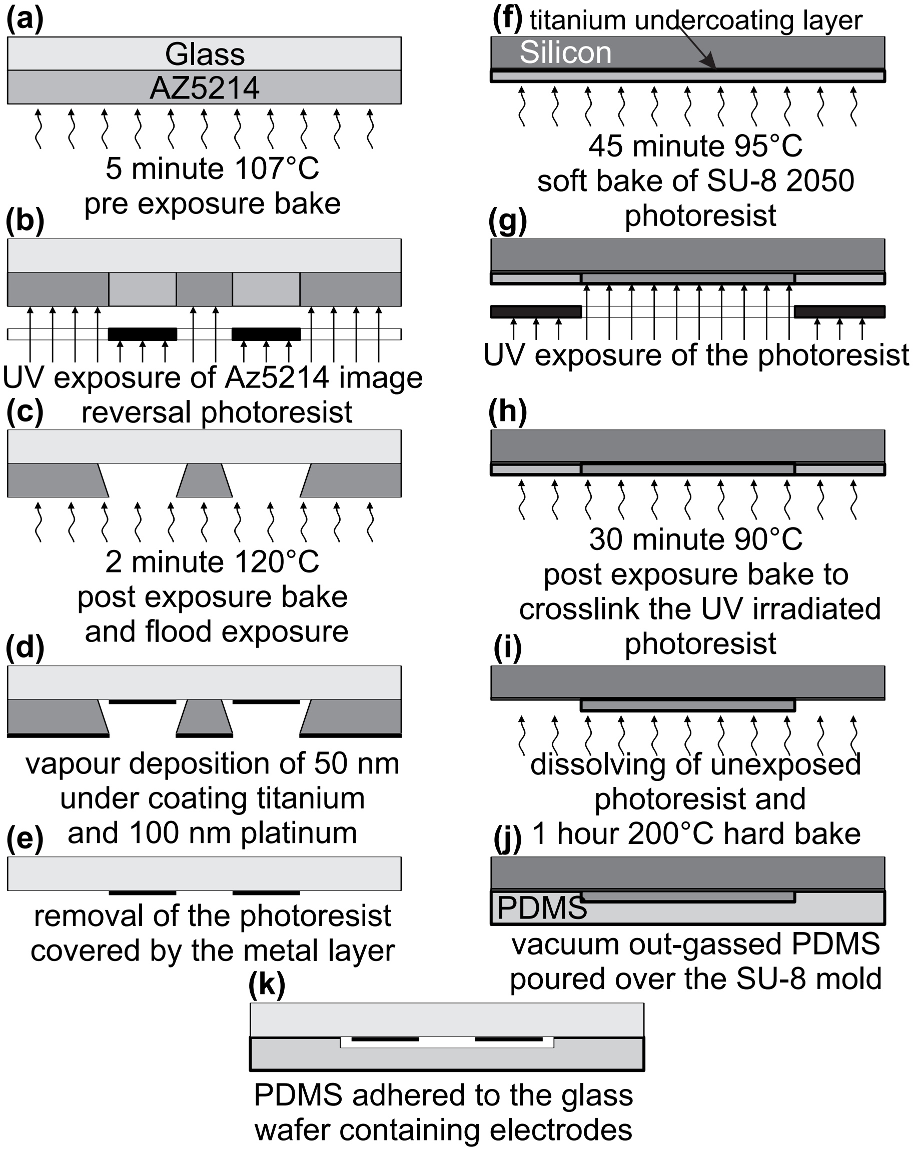

Figure 6.7: Fabrication process of the cell characterization and travelling wave dielectrophoresis separation microfluidic chip. **a-e**) The fabrication steps of the parallel platinum electrodes vapour deposited on a glass wafer. **f-j**) Fabrication steps of the silicon SU-8 mould on which vacuum out-gassed PDMS was poured to obtain the top layer of the chip with integrated channel structure. **k**) Aligning and combining the two layers yields the finalised DEP device.

6.5 Travelling Wave Dielectrophoresis

In this section a new design is presented based on twDEP to separate suspended-grown biological cell mixtures. TwDEP allows higher electric field strengths and uses a travelling electric field instead of a static electric field (see section 6.5.1) [170, 171].

Next to the in-phase component of the dipole moment, describing negative and positive DEP (real part of the Clausius-Mossotti factor, f_{CM}) in which the particles are repelled from or attracted towards the high electric field gradient respectively, the proposed separation method is mainly based on the imaginary f_{CM} out-of-phase component allowing twDEP.

A separation based on twDEP depends on differences in relaxation time and/or size differences between particles and medium in which they are suspended. A positive out-of-phase component indicates that the dipole lags behind the travelling electric field. A positive $\Im_m(f_{CM})$ yields a net force against the direction of field travel; a negative $\Im_m(f_{CM})$ to particle movement along the direction of field travel [143, 172–174]. Simulation results have been published showing the potential of applying twDEP for separation or concentration of bioparticles [175]. To proof the cell from cell separation principle simulations and experiments were conducted on the exposure of bacteria contaminated sample mixes containing *Saccharomyces cerevisiae* or Jurkat cells to a travelling electric field. Jurkat cells are derived from white blood cells (T-cell leukaemia) commonly used in laboratories for cell experiments. *S. cerevisiae* (yeast) and *Lactobacillus casei* (bacteria species commonly found in the human intestine and mouth) are convenient and safe to use cell models, which are comparable with severe pathogens. The mixture of those cells has, in principle, no clinical value, but is a useful set to test the performance of the separator.

6.5.1 Separation principle

The presented continuous separation principle is based on travelling wave dielectrophoresis. When a sample mix is introduced by a pressure driven flow at one inlet, roughly focused towards one side of the channel by an additional sheath flow, and exposed to a non-uniform phase-shifted travelling electric field generated by parallel electrodes positioned along the microfluidic channel, particles can be separated from the mix depending on their dielectrophoretic response (see Fig. 6.8 for a schematic representation of the

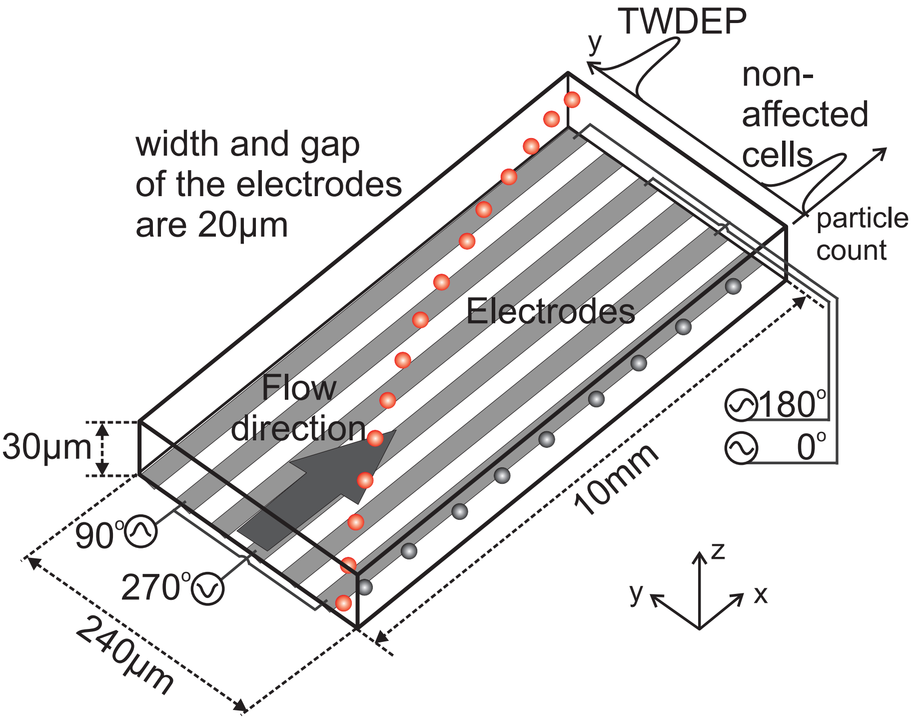

Figure 6.8: Separation based on travelling-wave dielectrophoresis. The sample is injected at the right side of the channel and is dragged through the channel by a pressure driven flow. Cells exposed to a non-uniform phase-shifted electric field experiencing twDEP move against the direction of field travel (cells move in the 0° - 270° - 180° - 90° direction) leaving the channel at the opposite side.

separation principle). The non-uniform travelling AC electric field is created by applying 90° phase-shifted voltages on the parallel electrodes (the distance between four electrodes, 0°, 270°, 180°, and 90° phase-shifted, corresponds with the wavelength of the travelling field).

The amplitude of the twDEP force depends mainly on the non-uniformity degree of the electric field and polarizability differences of the particles and surrounding medium in which the particles are suspended. The twDEP force vector is directed along the gradient of the electric field intensity and depends on the magnitude of the imaginary ($\Im_m \left| f_{cm} \right|$ out-of-phase) part of the Clausius-Mossotti factor:

$$\begin{aligned}\Im_m[f_{cm}] &= \frac{(\varepsilon_p-\varepsilon_m)\left(\frac{\sigma_p+2\sigma_m}{\omega}\right)-(\varepsilon_p+2\varepsilon_m)\left(\frac{\sigma_p-\sigma_m}{\omega}\right)}{(\varepsilon_p+2\varepsilon_m)^2+\left(\frac{\sigma_p+2\sigma_m}{\omega}\right)^2} \qquad (6.12)\\ \text{with} \qquad & \Im_m\left|f_{cm}\right| \in [-0.75...0.75]\end{aligned}$$

In steady-state condition the separation velocity of a particle exposed to a non-uniform electric travelling field can be obtained from the force equilibrium between the twDEP force and the counterbalanced hydrodynamic drag force (Eq. 6.13):

$$\vec{F}_{drag}+\vec{F}_{twDEP}=0 \qquad (6.13)$$

with

$$\vec{F}_{drag}=6\pi\eta r(\vec{v}_l-\vec{v}_p) \qquad (6.14)$$

and

$$\vec{F}_{twDEP}=-\frac{4\pi^2r^3\varepsilon_m}{\lambda}\Im_m\left|f_{cm}(\omega)\right|E_{rms}^2 \qquad (6.15)$$

which yields the particle velocity vector $\vec{v}_p$:

$$\vec{v}_p=-\frac{2\pi r^2\varepsilon_m}{3\eta\lambda}\Im_m\left|f_{cm}(\omega)\right|E_{rms}^2+\vec{v}_l \qquad (6.16)$$

where η is the viscosity, r the particle radius, $\vec{v}_l$ the liquid velocity vector, E_{rms}^2 the squared electric field, and λ the wavelength of the travelling field (the distance covered by four electrodes when a 0°, 90°, 180°, and 270° phase-shift is used).

The separation conditions were selected in such a way that the particles to be separated from the mix experienced a twDEP force against the direction of field travel (cells move in the 0°-270°-180°-90° direction; $\Im_m\left|f_{cm}\right|>0$) and a small nDEP force ($\Re_e\left|f_{cm}\right|<0$) directed away from the electrodes to prevent the particles from sedimentation or getting trapped (example given in section 6.5.4).

6.5.2 Trajectory simulation

Particle trajectories were simulated using Finite Element Analysis Software (COMSOL Multiphysics 3.5 and Matlab). Stationary 3-dimensional

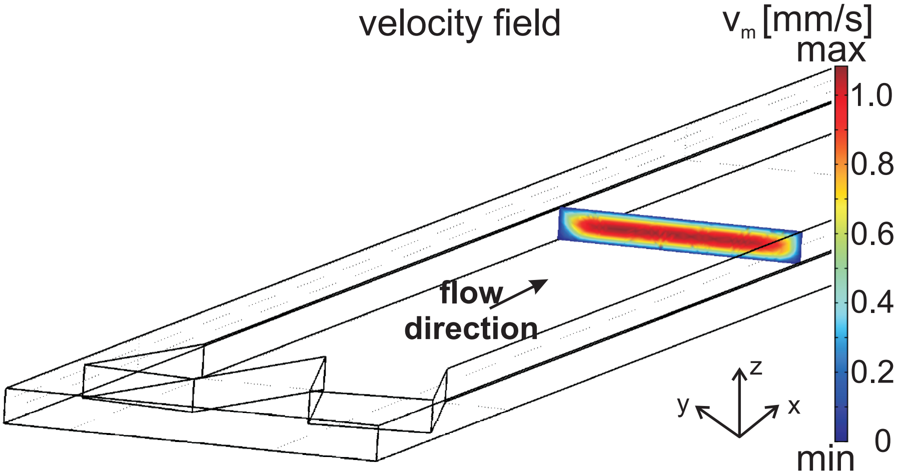

Figure 6.9: Simulation results of the fluid velocity through the microfluidic channel. The simulation conditions were set to: sample flow = 0.10 µL/min., sheath flow = 0.15 µL/min., liquid density = 1.05 kg/m^3, dynamic viscosity = 1.43 mPa.m. The channel section slice shows the parabolic flow profile due to a pressure driven flow. The channel dimensions are 13500 x 200 x 30 µm^3 (respectively x, y, and z).

fluid velocity was evaluated throughout a 10000 x 200 x 30 µm^3 channel (l x w x h); a 2D time-dependent electric field simulation was performed to understand the dynamic electric field strength with travelling wave motion. Because the electrodes are homogeneous in the depth of the channel, a 2D simulation is sufficient - see Fig. 6.10 for periodic images of simulated field results.

Simulation results were used in a particle trajectory calculation script, which evaluated the time-averaged DEP (lateral twDEP and the horizontal (y) and vertical (z) components of negative DEP) and drag forces on a particle at discrete time steps and they also calculated the resulting particle motion. An example of Jurkat cells from *L. casei* bacteria separation is depicted in Fig. 6.11.

The flow velocity in the separation section of the channel was 0.7 mm/s. The average lateral displacement velocity of Jurkat cells, exposed to a travelling electric field of 3.5 V$_{rms}$ at 100 kHz, obtained by simulations was 0.25 mm/s.

The bacteria are directed towards the lower electric field gradient regions located above the electrodes and channel wall (see the electric field stream lines depicted in Fig. 6.10). Due to the relative large width of the electrodes

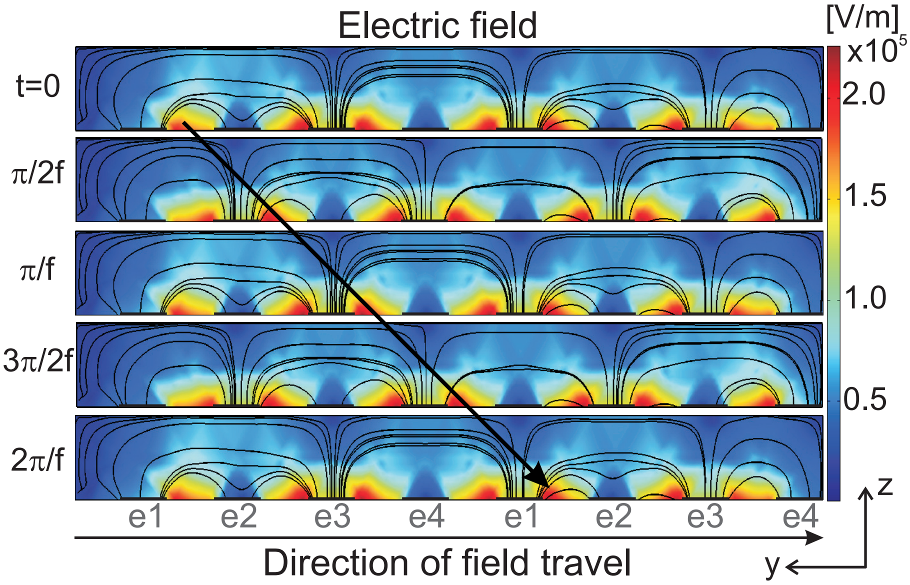

Figure 6.10: The image shows five 'snapshots' of the travelling field in progress, moving from left to right, with a colour map of electric field strength (V/m). Snapshots are taken (from top to bottom) at $t = 0$, $t = \pi/2f$, $t = \pi/f$, $t = 3\pi/2f$, $t = 2\pi/f$, where $f = 100\,\mathrm{kHz}$ and the applied voltage v_0 set to $3.5\,\mathrm{V_{rms}}$, for a complete cycle of the wave motion. The electrodes e1 - e4 were excited with a respectively 0°, 90°, 180°, and 270°phase shifted voltage. The diagonal arrow points out the field of travel direction between the different time frames. The stream lines represent the electric field gradient distribution above the electrodes.

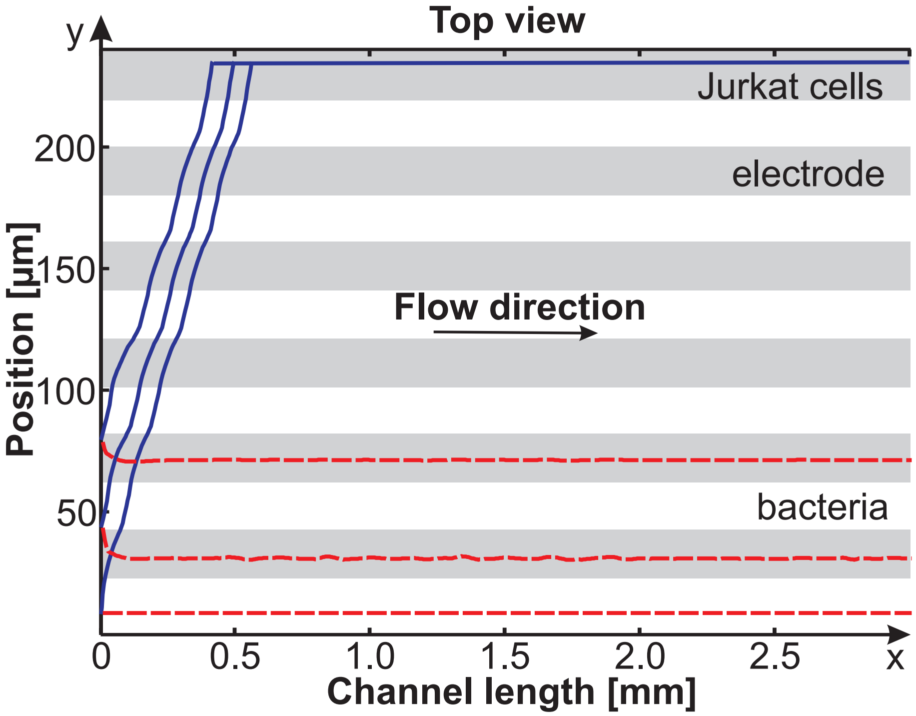

Figure 6.11: Simulation results. Particle trajectories of Jurkat cells (12 µm diameter, $\Im_m(f_{CM}) = 0.52$, and $\Re_e(f_{CM}) = \text{-}0.1$) and *L. casei* bacteria (1.6 µm diameter, $\Im_m(f_{CM}) = 0.01$ and $\Re_e(f_{CM}) = \text{-}0.5$) exposed to a 100 kHz, 3.5 V travelling electric field. The Clausius-Mossotti factors of the cells were derived by recording their rotational spectra. Varying starting points were selected along the y-axis (with z = 15µm). Fluid Flow: Sample (0 - 120 µm) 0.1 µL/min, Sheath: 0.15 µL/min, Electrode spacing 20 µm. Here, the travelling wave field moves against the y-direction across the channel. twDEP experiencing Jurkat cells are pushed towards the channel wall (solid lines), the bacteria (dashed lines) left the channel at distinct positions in the same y-region as they were introduced. (x and y not to scale).

(20 µm) the small bacteria (1.6 µm) cannot cross this barrier. They will follow this electric field gradient minimum when being dragged through the channel towards the outlet by an applied pressure driven flow (see bacteria trajectories in Fig. 6.11).

6.5.3 Material and methods

Sample preparation

Jurkat cells (a suspended-grown acute T-cell leukaemia cell line) were cultivated in culture flasks at 37°C and 5% CO_2. As growth medium, Dulbecco's modified eagle medium containing 4.5 g/L glucose, 10% fetal calf serum, 2 mM L-glutamine, and antibiotics(100 units/ml penicillin, 100 µg/ml streptomycin, and 0.25 µg/ml Amphotericin B) were used (all obtained from Lonza Bioscience).

S. cerevisiae (yeast) cells were obtained fresh from a local supermarket. Bacteria contaminated cell mixtures were made by adding *Lactobacillus casei* bacteria (DSM 20011) to the Jurkat and *S. cerevisiae* cultures. In Fig. 6.12 a photograph of the three cell types is shown. The strong influence of the culture medium and phosphate-buffered-saline (PBS) on the DEP phenomena (due to their high conductivity) was prevented by washing the cell mix twice in 5 mL low conductivity DEP medium. This medium consisted of 10% (w/w) sucrose (Sigma S9378), 2% (w/w) dextrose (Sigma D9559), and deionized water. Besides preventing the cells to sediment due to gravity, the density matched medium (density of 1.05 g/mL [176]) also compensates for the osmotic pressure on the cells. By adding PBS (pH 7.2) the final DEP medium conductivity was set to 40 mS/m (measured with HANNA HI9835). The final concentration of Jurkat cells was approximately 1 x 10^6 cells/mL and that of the *S. cerevisiae* approximately 1 x 10^7 cells/mL.

Separation device

Experimental setup

The glass chip comprising the electrode structure and inlets is glued on a printed circuit board (PCB) containing a rectangular opening to access the inlets of the chip. The electrodes of the chip are connected to the bonding pads of the PCB by thin copper wires. Two sine wave generators (Agilent

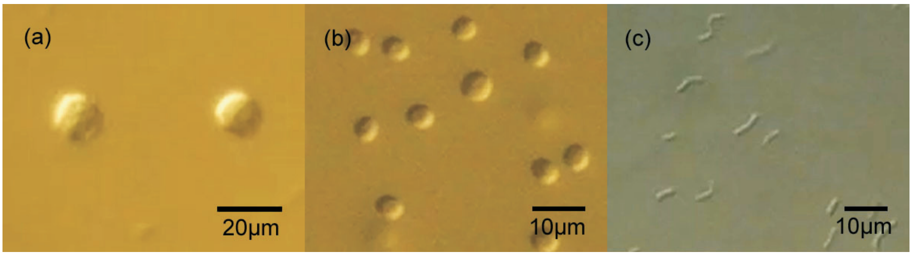

Figure 6.12: **A)** *Jurkat* cells, **B)** *S. cerevisiae*, and **C)** *L. casei* bacteria.

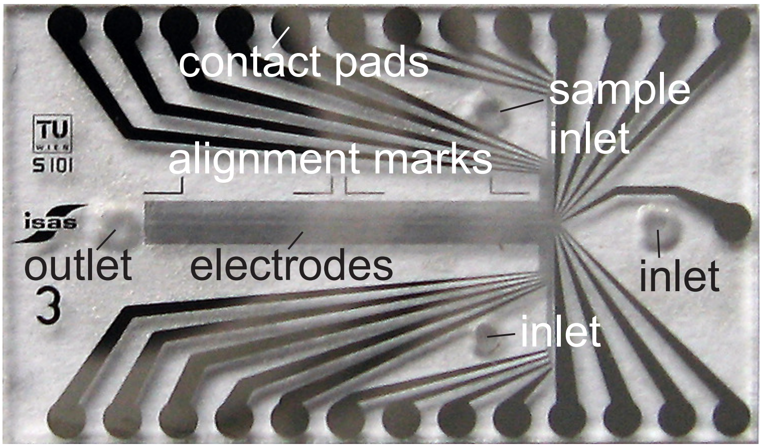

Figure 6.13: Photograph of the 19 x 11 mm^2 travelling wave DEP separation device. The chip contains 27 parallel electrodes, 20 µm in width and 1 cm in length with a gap size of 20 µm, each phase-shifted 90° to obtain a travelling electric field.

33220A), 90° phase-shifted and decoupled by two broadband transducers, are used to excite the DEP electrodes.

Cell characterization experiments to measure the crossover frequencies and ROT spectra of cells (rotational velocity, see section 6.5.4) are performed without an external pressure driven flow. To avoid flow disturbance during the measurements, the inlets are sealed with PDMS.

For continuous separation experiments, the sample is pumped through the device by a syringe pump (KD Scientific 210P). Additionally, a s pump is used to introduce a sheath flow (DEP medium) to roughly focus the sample stream.

Before attaching the chip to the holder, the tubes of the device holder are connected to the syringes and filled with DEP medium. 50 µL of sample suspension is introduced directly into the inlet-tube via the rubber O-ring on top of the holder while the syringe pump is operated in withdrawal mode.

The chip is prepared by pipetting a droplet of ethanol on top of the inlets which then fills the channel by capillary forces. Afterwards, the chip is rinsed with DEP medium without introducing air bubbles.

The final preparation step is attaching the PCB comprising the DEP chip on top of the holder. The measurement results are captured by a high definition camera (Samsung VP-HMX20C) mounted to an optical light microscope (Zeiss Axiotron). The overall measurement setup is depicted in Fig. 6.14.

The separation process has been characterized by processing the acquired video files by a custom build software program (described previously by *Kostner et al.* [155]). When Jurkat or *S. cerevisiae* cells are passing the detection window near the outlet the cell position is stored in a file.

6.5.4 Results and discussion

Cell characterization

Before introducing the sample mix into the twDEP separation device, the individual cell types, Jurkat, *S. cerevisiae*, and *L. casei*, have been characterized by recording their DEP and ROT spectra with a quadrupole electrode design (Fig. 6.15). The DEP and ROT spectra of cells are obtained by exposing the cells to a rotating electric field and grabbing frames from captured video files. The cell rotations per time unit are extracted by comparing these video images. Only cells located near the centre of the quadrupole electrode and at least four cell diameters away from each other are taken into account. This way the influence of the dipolar field of neighbouring

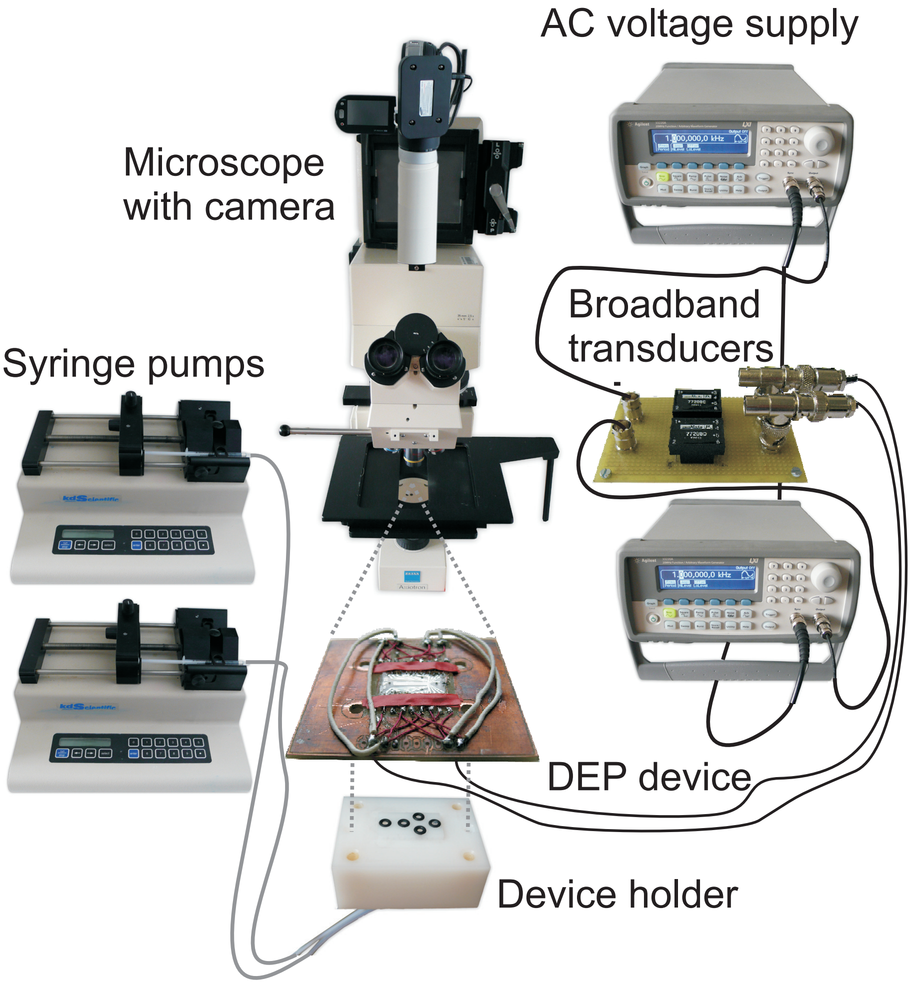

Figure 6.14: Measurement setup. Two syringe pumps are used to roughly position the sample mix to one side of the channel. Two sine wave generators, connected to broadband transducers to obtain 0°-90°-180°-270° phase-shifted voltages, are used to excite the DEP electrodes.

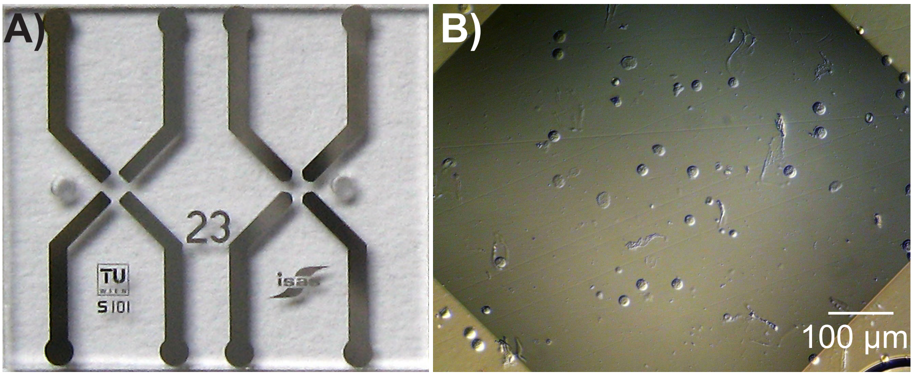

Figure 6.15: **A)** Photograph of the 13 x,11 mm^2 cell characterization device. The chip contains two quadrupole electrodes, with an inner diameter of respectively 720 and 600 µm. **B)** Jurkat cells loaded into the cell characterization device.

cells is avoided [143, 163, 164].

To obtain the DEP and ROT spectra, the same procedure was used as described by Gascoyne et al [163]. An overview is described in section 6.3. Jurkat cells, comprising a phospholipid bilayer membrane, were modelled as a thin-shelled sphere. *S. cerevisiae* cells and bacteria have an additional cell wall build from polysaccharides and, therefore, a two-shell model was required, introducing the additional cell wall with dielectric properties ε_{p1}, σ_{p1}, and thickness δ. The obtained DEP and ROT spectra were required to get an estimation of the feasibility of the proposed separation method. Besides the difference in size and shape (Jurkat and *S. cerevisiae* spherical of respectively approximately 12 and 5 µm diameter and *L. casei* rod shaped and approximately 1 x 2 µm^2) there is also a clear difference in their DEP and ROT spectra (Fig. 6.16).

Continuous separation experiments

For continuous separation experiments, a microfluidic chip was used comprising a 200 µm wide channel structured in PDMS. From the lower y-region inlet (see Fig. 6.17a) the sample mix was introduced at a flow-rate of 0.10 µL/min. A sheath liquid, DEP medium without cells, at 0.15 µL/min was utilized to focus the cell mix roughly at the 0 - 60 µm y-region of the separation channel.

The flow-velocity was optimized to allow reliable particle position detection based on a software program that detects differences between the

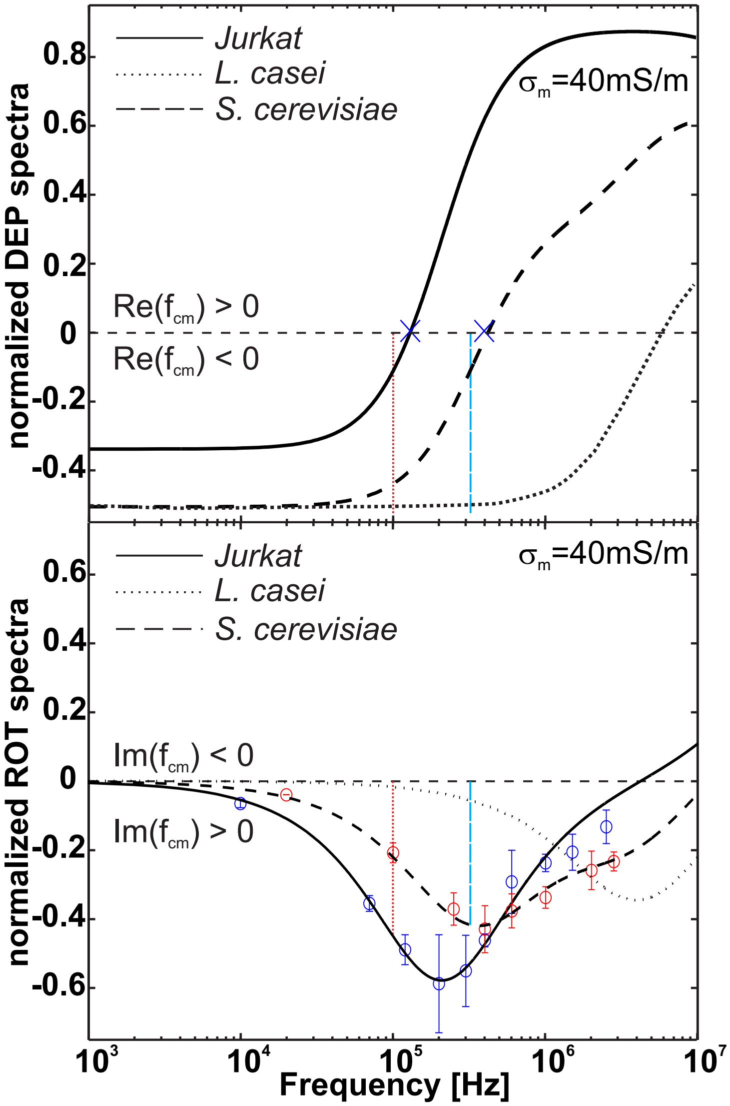

Figure 6.16: DEP and ROT spectra of Jurkat cells, *S. cerevisiae*, and *L. casei* bacteria, resuspended in a low conductivity buffer of $\sigma_m = 40$ mS/m. The imaginary values of the Clausius-Mossotti factor of all cells were measured. For Jurkat and *S. cerevisiae* cells at a medium conductivity of 40 mS/m and at 2.3 mS/m for *L. casei* bacteria. By calculation, the values of the Clausius-Mossotti factor of *L. casei* bacteria at 40 mS/m were derived by calculation. At a travelling wave electric field frequency of 100 kHz (dotted line), Jurkat cells experience a force against the direction of field travel, while *L. casei* bacteria are hardly influenced. At a frequency of 350 kHz (dashed line), *S. cerevisiae* cells can be separated from *L. casei* bacteria.

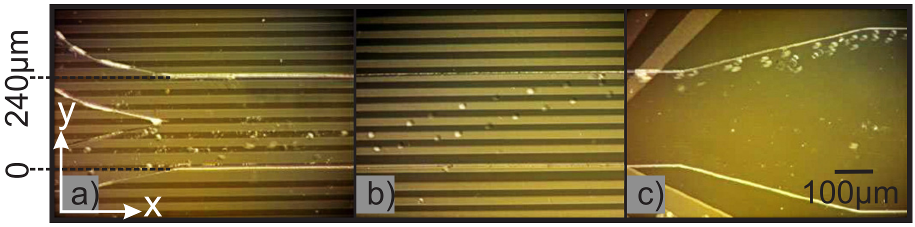

Figure 6.17: Separation of Jurkat cells by a travelling electric AC field. **a)** Cells enter the device on one side of the channel. **b)** The targeted cells are moving against the field of travel towards the other side of the channel. **c)** Separated cells leaving the channel.

actual frame and a background calculated from two preceding frames. Directly after the separation section the channel widens from 200 to 400 µm. This way the flow-velocity is decreased from 0.69 to 0.35 mm/s (when applying a total flow-rate of 0.25 µL/min). By focusing a high definition camera attached to a microscope in this widened channel section, particles were identified and their position was stored when passing by. To cover the whole width of the channel a field of view of about 460 x 810 μm^2 was chosen. With a camera capture frame rate of 25 frames per s and a flow-velocity of 0.35 mm/s, 19 frames per cell (cells passing 14 µm from frame to frame) were obtained in the widened section, which was sufficient to detect single Jurkat and *S. cerevisiae* cells, but, unfortunately, not for the much smaller *L. casei* bacteria.

In Fig. 6.17b cells can be seen which are experiencing a perpendicular twDEP force directed away from the field of travel when being dragged through the channel by a pressure driven flow in x-direction. In the last frame (Fig. 6.17c) the outlet is depicted showing that Jurkat cells leave the channel at the opposite channel wall.

The first sample which has been investigated was a mix of *S. cerevisiae* and *L. casei* with concentrations of approximate 1 x 10^7 and 1 x 10^8 cells/mL respectively. Without an applied DEP voltage (DEP off) the cells left the channel in the y-region between 0 - 60 µm, the same y-region at which they entered the separation channel. After switching on the DEP voltage (DEP on, 5 V_{rms} at 350 kHz), the electrodes were excited, creating a travelling electric wave directed against the y-direction (Fig. 6.18). Under the set conditions, 92% of the *S. cerevisiae* cells were leaving the separation channel at another y-region from where they initiated. Specifically, 87% of the cells left channel in the 185 to 200 µm y-region. Unaffected *S. cerevisiae*

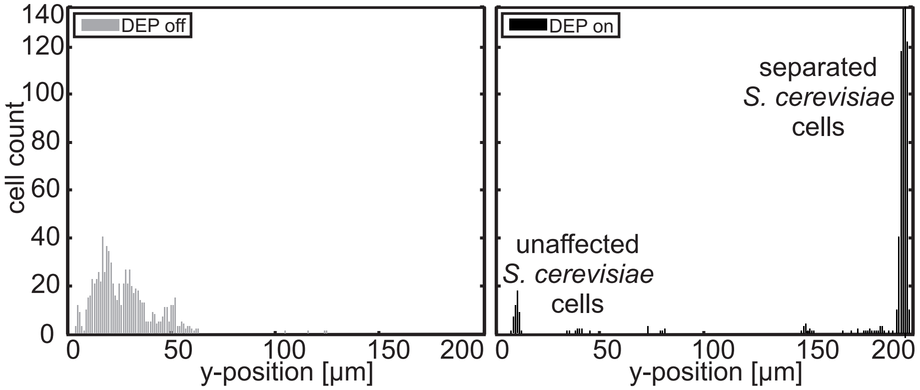

Figure 6.18: *S. cerevisiae* cells separated from cell culture debris containing non-viable cells and *L. casei* bacteria. The sample stream (0.1 µL/min) was introduced in the y-region of 0 to 60 µm by a sheath flow of 0.15 µL/min (DEP off). By applying a phase-shifted voltage of 5 V_{rms} at 350 kHz, a travelling electric field was obtained (DEP on). The viable *S. cerevisiae* cells were directed away from the field of travel (cells move in the 0° - 270° - 180° - 90° direction) towards the other side of the channel (y-region of 185 to 200 µm).

cells (8%) and culture debris were not influenced by the applied electric field and, therefore, left the channel in the same y-region (0 - 60 µm) as they were introduced. The *L. casei* bacteria left the separation channel at distinct positions (y = 0, 35, and 75 µm) of the 0 to 60 µm y-region (guided by the electric field gradient minima above the electrodes and channel wall). These positions were visually verified and correspond with the simulated trajectories depicted in Fig. 6.11.

The second sample mix consisted of suspended-grown Jurkat cells contaminated with *L. casei* bacteria, cell culture debris, and non-viable cells (approximate Jurkat and *L. casei* concentrations were respectively 1 x 10^6 and 1 x 10^8 cells/mL). The optimum separation conditions for viable Jurkat cells from the sample mix, suspended in DEP medium with a conductivity of 40 mS/m, were selected by applying cell characterization experiments (results shown in section 6.5.4, Fig. 6.16). At a phase-shifted voltage of 3.5 V_{rms} at 100 kHz, the excited electrodes created a travelling electric field optimized for deflecting the viable Jurkat cells: a small nDEP force ($\Re_e\,|f_{cm}| < 0$) to repel the cells from the electrodes and a maximum twDEP force ($\Im_m\,|f_{cm}| > 0$) to separate the viable cells from the mix. Successful separation of the viable Jurkat cells from the mix is depicted in Fig. 6.19. The sample and sheath flow-rates were set to respectively 0.10

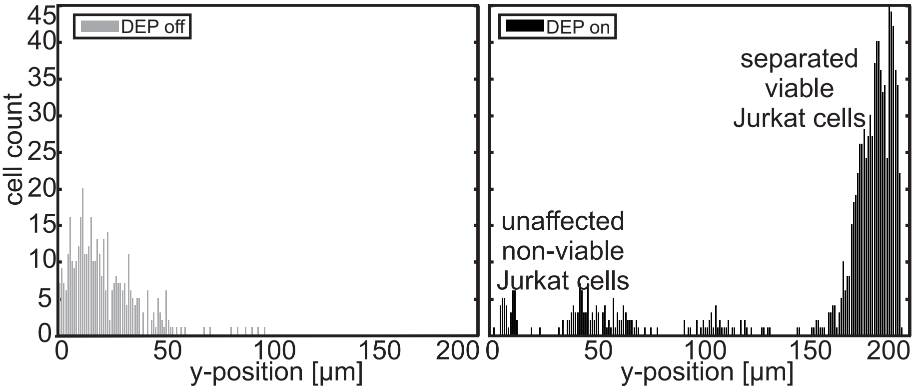

Figure 6.19: Viable Jurkat cells separated from cell culture debris containing non-viable cells and *L. casei* bacteria. The sample stream (0.1 µL/min) was introduced in the y-region between 0 and 60 µm by a sheath flow of 0.15 µL/min (DEP off). By applying a phase-shifted voltage of 3.5 V_{rms} at 100 kHz, a travelling electric field was obtained. The viable Jurkat cells were directed away from the field of travel(cells move in the 0° - 270° - 180° - 90° direction) towards the other side of the channel (y-region between 170 and 200 µm), while the *L. casei* bacteria, cell culture debris, and non-viable Jurkat cells were not (DEP on).

and 0.15 µL/min.

Altogether, 86.5% of the Jurkat cells were leaving the separation channel in the 170 to 200 µm y-region. These findings comply with the simulated trajectories showing that Jurkat cells move towards the opposite channel wall as they were introduced when exposed to a travelling electric field of 3.5 V_{rms} at 100 kHz. Furthermore, the required distance of approximately 450 µm along the channel to move 130 µm towards the channel wall is in line with the simulations (see Fig. 6.11 and 6.17b).

The remaining 13.5% of unaffected Jurkat cells and culture debris left the device without an applied voltage (DEP off, 0 - 60 µm y-region).

In order to determine the response of non-viable Jurkat cells exposed to a travelling electric field of 3.5 V_{rms} at 100 kHz, a cell sample was fixed with formaldehyde to keep the cells in the normal spherical shape, but make them non-viable at the same time. All fixed cells were unaffected and left the separation channel in the same y-region as they were introduced.

The *L. casei* bacteria left the separation channel at distinct positions. The 86.5% and 13.5% corresponds with the cell viability test results obtained prior to the separation measurement (tryphan blue non-viable cell staining; $\geq 90\%$ viable). The 3.5% difference in viability test and cell separation (viability) is due to the 1.5h time difference. From visual analysis of the video sequences we can conclude that no bacteria were leaving the separation channel in the 100 - 200 µm y-region, but at distinct positions ($y = 0, 35$ and 75 µm) guided by the electric field gradient minima above the electrodes and channel wall. The separated *S. cerevisiae* and Jurkat cells are not mixed with bacteria and non-viable cells when leaving the separation channel, which shows the high purity of the separation method.

6.5.5 Conclusions

The proposed travelling wave dielectrophoresis (Section 6.5) based cell from cell separation principle has been simulated and experimentally verified by exposing bacteria contaminated sample mixes containing *S. cerevisiae* or Jurkat cells to a travelling electric field perpendicular to the hydrodynamic flow direction. This travelling electric field is created by exposing parallel electrodes, divided in pairs of four and positioned along the microfluidic channel, to respectively a 0°, 90°, 180°, and 270°phase shifted voltage.

Cell attachment to the electrodes was prevented by selecting the separation conditions in such a way that the cells of interest were experiencing a small nDEP force away from the electrodes.

The DEP force scales with the 2^{nd} power of the applied electric field (see Eq. 6.15) and, therefore, only a $\sqrt{2}$-fold increase of the applied voltage is required to double the separation throughput (at a double flow-velocity).

Only cells affected strongly enough by the travelling electric field are pushed toward the opposite channel wall while being dragged by a hydrodynamic flow. Unaffected cells and cell culture debris will not enter this region of the channel allowing cell separation of high purity.

Bacteria movement towards the opposite channel wall, as opposed to where where they were introduced, was prevented by the electric field gradient minima above the electrodes (the electrode width is large compared to the size of the bacteria).

Viable suspended-grown cells have been successfully separated from bacteria contaminated cell mixes with the device. Experiments on both bacteria contaminated suspended-grown *S. cerevisiae* as well as Jurkat cells show nearly perfect separations of the viable cells, which could otherwise only be separated by flow-cytometry requiring elaborate labelling steps.

Chapter 7

Conclusions and Outlook

In this chapter, the main conclusions of the research conducted for this thesis and future research possibilities are described.

The potential of an infrared absorbance based sensor system for the determination of the CH_2-symmetric to CH_2-antisymmetric stretch ratio, to aid in the detection of the presence of cancer cells, and to differentiate between various cancer cells, has been successfully demonstrated for cell lines originated from kidney epithelial tissue and melanocytes. This methodology yielded statistical significant CH_2-stretch ratio differences between the individual cell lines, normal and tumorous, of both epithelial kidney and melanocyte origin (Chapter 4). To test this CH_2-stretch ratio cell discrimination method, a four-wavelength mid infrared absorbance sensor was designed and realised that has the potential to be further developed in a point-of-care instrument (Chapter 3). The mechanism influencing the CH_2-stretch ratio of mammalian cell membranes has been investigated by exposing a normal epithelial kidney cell line (MDCK) to the plasma membrane bound cholesterol reducing agent methyl-β-cyclodextrin. Measurement results indicate that an increase in CH_2-stretch ratio arises when there is a decrease in, or redistribution of, the membrane stabilizing agent cholesterol (Section 4.3.4). Preliminary CH_2-stretch ratio measurements to investigate the effect of the chemotherapeutic drug cisplatin on three different melanoma cell lines indicates that exposure to 20 µM cisplatin for 0.5 h to 16 h yielded a significant decrease in CH_2-stretch ratio for all three melanoma cell lines. This suggest that the CH_2-stretch ratio could be used to determine the lowest working dosage (concentration of cisplatin) reducing the chance of severe side effects such as multiorgan toxicity, deafness, blindness, seizures, and vomiting when administered to a patient (Section 4.3.5). Further experimentation to determine the effect of different concentrations of multiple chemotherapeutic drugs on tumour tissue would be of clinically importance improving and optimising chemotherapy. Besides determining and comparing the CH_2-stretch ratio of dried cells, also a measurement method has been designed for the determination of the CH_2-stretch ratio of cells suspended in PBS (Chapter 5). This has been realised by adding a self-designed IR transparent sample-chip to the measurement setup. The inner chamber height of this chip is approximately 20 µm, allowing a sufficient amount of IR-light to be transmitted by the water fraction and be detected by a photodiode. Measurements on as well two epithelial kidney cell lines as three melanoma cell lines yielded statistical significant CH_2-stretch ratio differences between the individual cell lines originated from the same organ. The possibility to measure infrared absorbance of cell samples suspended in PBS indicates the potential for further development of the sensor platform into a microfluidic measurement system allowing the screening of, for example, lymph fluid for the presence of tumour cells. Multiple cells could be accumulated/trapped when entering the detection region allowing IR absorbance measurements to determine the CH_2-stretch ratio of these suspicious cells. When recording the infrared spectra of biological samples the strong water absorbance bands should be taken into account. A way to overcome the strong peaks between 1500 and 1750 cm^{-1} and 2900 and 3700 cm^{-1} is by suspending the cell sample in deuterated (heavy) water instead of hydrogenated water (the absorbance peaks are shifted towards lower wavenumbers at 1100 - 1200 and 2200 - 2750 cm^{-1} (Fig. 7.1).

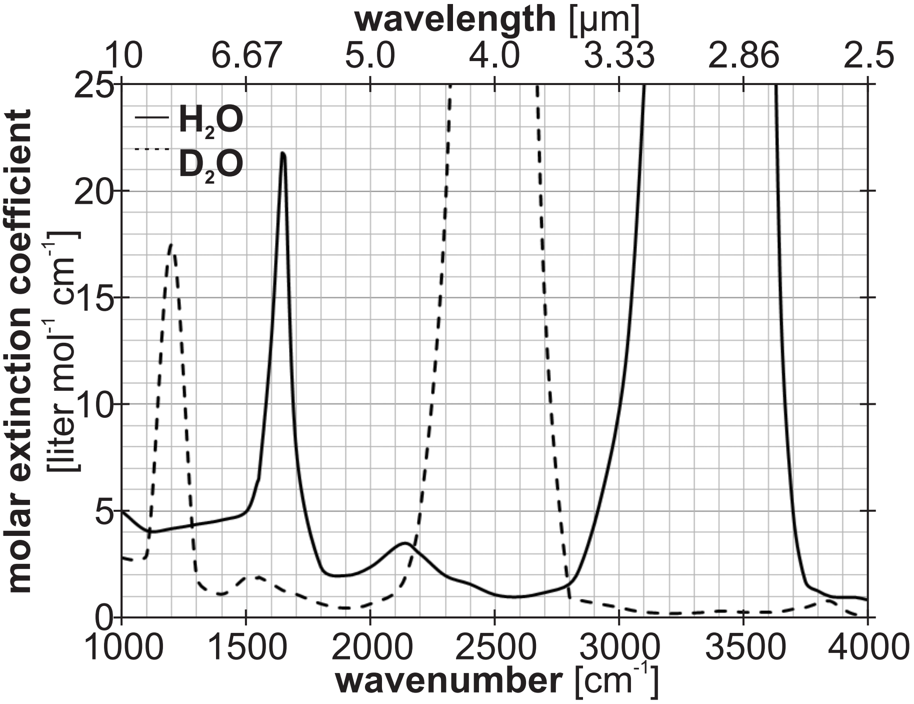

Figure 7.1: Molar extinction of H_2O and D_2O at 25°C [119].

The dielectrophoretic based cell separation method (and realised device) show the feasibility to separate cells from other cells, cell debris, and bacteria.

The experimental results presented in Section 6.5, where bacteria were aligned at distinct positions and not crossing the 20 µm wide electrodes (due to the large electrode gap, under the set conditions), shows that bacteria could be separated from the sample mix by an optimized electrode array. This electrode array could consist of electrodes of different widths (e.g. increasing from 5 µm, 10 µm, and 15 µm) positioned along the channel (Fig. 7.2). Under optimized conditions, mammalian cells will move towards the opposite channel wall as they were introduced when exposed to a travelling electric field. The much smaller bacteria however, will only cross the electrodes of smaller width and be aligned between the electrodes where the gap is too wide to be crossed. Unaffected, non-viable cells and cell debris will leave the channel in the same y-region as they were introduced.

The successful measurements shown in this thesis were all performed on well-defined cell lines, the next step is to investigate clinical samples such as biopsies and lymph fluid drainage.

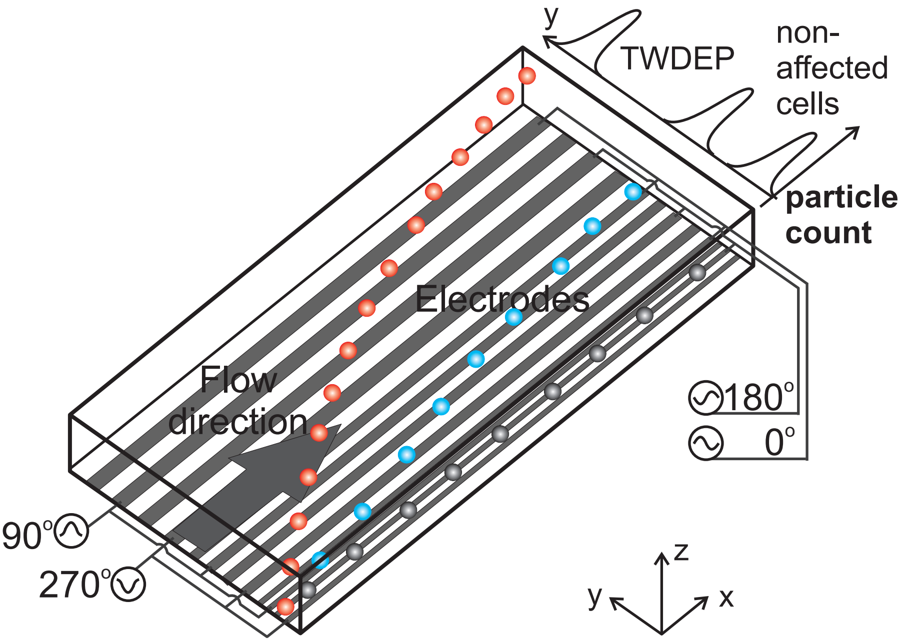

Figure 7.2: Travelling-wave dielectrophoresis separation concept based on an electrode array of increasing width. The sample is injected at the right side of the channel and is dragged through the channel by a pressure driven flow. Cells exposed to a non-uniform phase-shifted electric field experiencing twDEP move against the direction of field travel (cells move in the 0° - 270° - 180° - 90° direction) leaving the channel at the opposite side. Bacteria, moving towards the same direction as the cells, are aligned between the electrodes where the gap is too wide to be crossed. Unaffected, non-viable cells and cell debris will leave the channel in the same y-region as they were introduced.

In body fluids, such as blood and lymph fluid, also normal non-tumorous cells are present. For a dielectrophoretic based separation of suspicious tumour cells from normal cells, a clear difference in the ClausiusMossotti function for the different cell types is required. Gascoyne et al. have shown that there is a clear difference in the ClausiusMossotti function observed for T-lymphocytes and breast tumour cells [177], indicating the potential of dielectrophoresis as separation method to harvest suspicious tumour cells from body fluids. A label-free tumour cell separator combined with the CH_2-stretch ratio sensor would be a very helpful tool to aid physicians in the diagnosis of lymph fluid for the presence of tumour cells after lymph node dissection.

Appendix A

Cell lines

Table A.1: Cell lines, classified in biosafety level 1 (BSL-1), investigated for label-free cell analysis and separation.

Name	organism	organ	cell type (derived from)	disease
MDCK	*Canis familiaris*	kidney	epithelial	-
A-498	*Homo sapiens*	kidney	epithelial	carcinoma
Caki-1	*Homo sapiens*	kidney	epithelial	carcinoma
Renca	*Mus musculus*	kidney	epithelial	-
MM5.K	*Mus musculus*	kidney	epithelial	adenocarcinoma
M14	*Homo sapiens*	skin	neural crest	melanoma
518A2	*Homo sapiens*	skin	neural crest	melanoma
A375	*Homo sapiens*	skin	neural crest	melanoma
HEMa	*Homo sapiens*	skin	neural crest	-
Jurkat	*Homo sapiens*	blood	T-lymphocyte	acute leukaemia

Appendix B

Cholesterol extraction

This protocol was adapted from Bezrukov et al [178] and Zarzycki et al [179].

1. Prepare cultivator dishes by washing in methanol/HCl (1:1 v/v) 30 min at room temperature.
2. Rinse in ethanol, air dry.
3. Coat slides with 0.25 mg/mL Polylysine in 0.15 M borate buffer (pH 8.3).

    - Overnight, room temperature.

4. Seed cells, attachment for 5 h.
5. Treatment with MβCD (Sigma-Aldrich, Germany, C4555) in serum free medium: 10 mM and 20 mM for 1 h at room temperature.

    - Sample '20' for 20 mM MβCD.
    - Sample '10' for 10 mM MβCD.
    - Sample 'c' for control (0 mM MβCD).

6. Membrane disruption (2x):

    - Wash with distillated H_2O for 1 min.
    - Wash with tris-buffered-saline x2.

7. Isolation:

- Pour into plates (Merck Silica gel 60) 5 mL of chloroform/-methanol (2:1, v/v) shake gently at room temperature for 1 h.
- Collect solvent and wash with 0.2 x volume in 0.9 % NaCl solution.
- Vortex, spin down at 2000 rpm for 5 min.
- The upper phase was removed by a glass pipette and discarded.
- The interface was rinsed once with methanol/water (1:1, v/v) without mixing the whole preparation.
- The lower chloroform phase, containing the lipids, was carefully transferred to fresh tubes and evaporated under a stream of argon. The lipid residue was dissolved in chloroform [200 µL] and stored at -30°C.

8. Thin layer chromatography (TLC) analysis:

- Samples were loaded on silica gel, approx. 22 drops per sample; 0, 10, and 20 mM MβCD exposed MDCK cells, and a marker containing pure cholesterol (Sigma-Aldrich, Germany, C3045), diluted in chloroform/methanol (2:1, v/v), at a concentration of 2 µg/mL.
- A 20 min TLC run was made in n-hexane: ethyl ether: acetic acid (80:20:1, v/v/v), repeated after drying the plate.
- Detection: the spots were visualized by 10% sulfuric acid in ethanol.
- Development by heating at 100°C, [approx. 5 min].
- The migrated spots on the TLC plate were scanned with a SynGene scanner and analysed with GeneTools analysis software.

Appendix C

The CH_3-Stretch Ratio

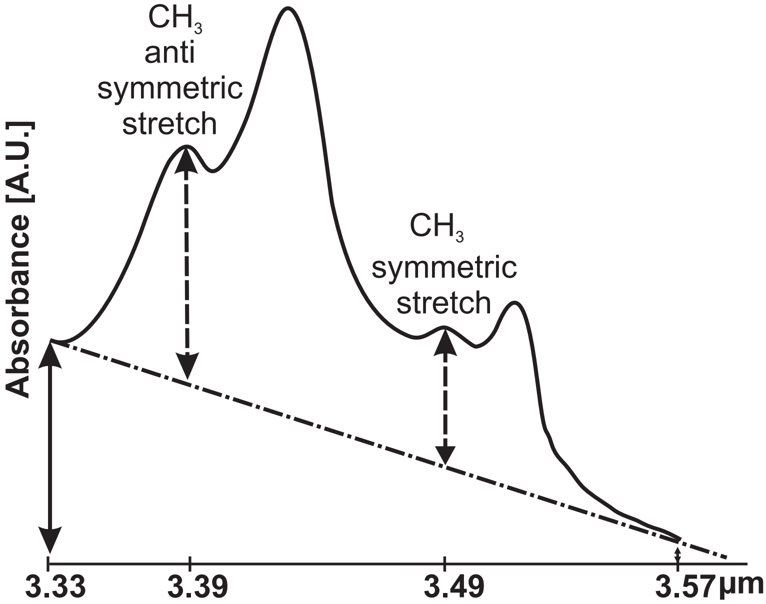

Figure C.1: Detection method. To evaluate the CH_3-stretch ratios of different samples base line correction is required. The absorbance values at 3.33 and 3.57 µm, solid arrows, are used to determine the base line. As a result the functional absorbance values at 3.49 and 3.39 µm, dashed arrows, can be calculated. By dividing the functional absorbance values, 3.49 / 3.39 µm, the normalized CH_3-stretch ratio will be obtained that can be used for sample comparison.

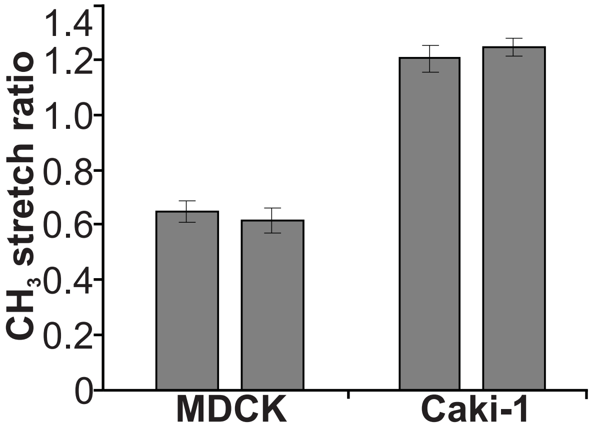

Figure C.2: Sensor CH_3-stretch ratio measurement of dried normal MDCK (mean ± standard deviation, 0.65 ± 0.04, and 0.62 ± 0.04) and malignant Caki-1 (1.20 ± 0.05 and 1.24 ± 0.03 epithelial kidney cells. Bars represent means ± standard deviation per cell passage (each bar comprises the average CH_3-stretch ratio of 5 spots with 500 - 1250 measurements per spot).

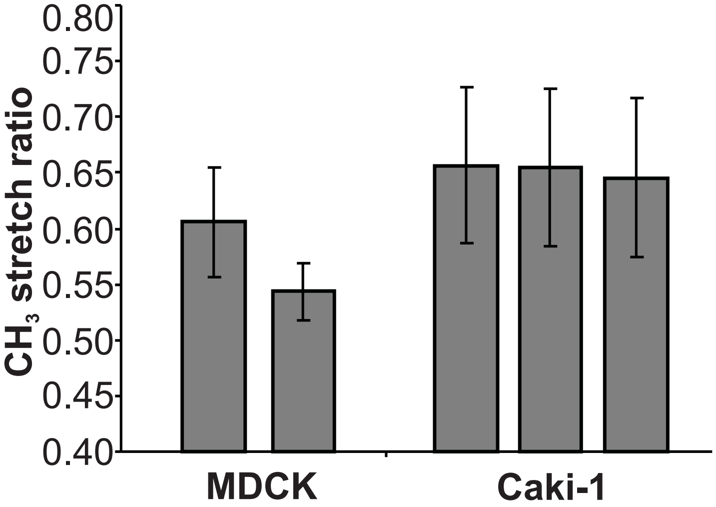

Figure C.3: Sensor CH_3-stretch ratio measurement of normal MDCK (mean ± standard deviation, 0.60 ± 0.05, and 0.54 ± 0.03) and malignant Caki-1 (0.66 ± 0.07, 0.66 ± 0.07, and 0.65 ± 0.07) epithelial kidney cells suspended in phosphate-buffered-saline. Bars represent means ± standard deviation per cell passage (each bar comprises the average CH_3-stretch ratio of 5 spots with 500 - 1250 measurements per spot).

Acknowledgements

It is a great pleasure to thank those who made this thesis possible.

First of all I would like to thank my supervisor Michael Vellekoop for giving me the opportunity to come to Austria to work as a PhD student in his research group. The four years of great support during the ups and downs of the research project were incredibly helpful. The many critical discussions about the PhD research, project proposals, and other topics I enjoyed very much.

I would also like to thank my co-examiner Peter Verhaert for introducing me to the CellCheck project and for his kind willingness to review this thesis.

I am very grateful to my colleagues and friends Stefan Kostner, Michael Rosenauer, Gabriel Hairer, Christian Riesch, Georg Fercher, Nicola Moscelli, Ioanna Giouroudi, Anna Haller, Wolfgang Buchegger, Dietmar Puchberger-Enengl, and Christoph Haiden for creating a perfect working atmosphere and the many nice after work meetings. I owe my deepest gratitude to Stefan Kostner for his kind hospitality, specially during the first months in Vienna. Also I would like to thank him for introducing me to the theoretical and practical challenges of microfluidics. Presenting the results of the conducted research at international conferences is an important part of the PhD work. Many thanks go to Michael Rosenauer for making our 2009 world tour to Munich, Seoul, and New Zealand, a great time. I would like to thank my room-mate Nicola Moscelli for the many discussions and being a great travel companion during the CellCheck meetings. Christian Riesch I would like to thank for providing the LaTeX class files and support.

Being a PhD student within a Marie Curie Research Training Network has let to many great opportunities. The partner institute visits, summerschools, technical presentations, international conferences, and joined cooperation's were very stimulating and a valuable experience. The international working atmosphere made the world feel much smaller. I would like to thank Wojciech Witarski, Marco Ballini, Gianluca Cama, Inez Finoulst, Josef Horak, Teresa Valero, Patricia Vazquez, Elina Iervolino, Kermen Bolaeva, Filippo Iuliano, Emanuel Weber, and all other fellows and partners of the CellCheck network, special thanks to Silvia Pastorekova, Wojciech Witarski and Filippo Iuliano, Institute of Virology, Slovak Academy of Sciences, Bratislava for cultivating and preparing the kidney cell lines and fruitful discussions.

I am grateful to Christine Hafner and Nina Balazs, Department for Pathophysiology and Allergy Research, Center for Pathophysiology, Infectiology & Immunology, Medical University of Vienna for kindly cultivating the melanoma cell lines and the nice cooperation investigating melanoma cells.

Bernard Lendl, Sergio Armenta-Estrela, and Alison Hobro, Institute of Chemical Technologies and Analytics, Vienna University of Technology I would like to thank for conducting the infrared spectroscopy measurements. The infrared absorbance recordings of the kidney cell lines showed the feasibility of the cell type discrimination method.

I would like to show my gratitude to my students Dietmar Puchberger-Enengl, Vivek Rao, Christoph Haiden, and Heléne Zirath for successfully contributing to our research.

The work presented in this thesis is part of an EU Marie Curie Research Training Network (MRTN): On-Chip Cell Handling and Analysis, CellCheck. Project number MRTN-CT-2006-035854.

Furthermore, I would like to thank the people from the Institute of Sensor and Actuator Systems, Franz Keplinger, Robert Schawarz, Peter Svasek, Edeltraud Svasek, Ewald Pirker, Theresia Bruckner, Martina Bittner, and Sabine Fuchs for their great support. Special thanks to Peter Svasek and Edeltraud Svasek from the Sensor Technology Lab at ISAS and the Center for Micro- and Nanostructures (ZMNS), for realising the designed microfluidic devices. Ewald Pirker I would like to thank for fabricating the sample holder.

Special thanks to my family and friends for their support during the last few years. I am very grateful to my sister Leonie van den Driesche for English language editing. Also, I would like to thank my fiancé Lidia Golubeva for her love and great support, specially in the final months of the research.

Last, but not least, I would like to thank my parents Catharina and Gerard van den Driesche for their love, support, and guidance.

List of Publications

Journal Papers

S. van den Driesche, W. Witarski, S. Pastorekova, and M. J. Vellekoop, “A quadruple wavelength IR sensor system for label-free tumour screening.” *Meas. Sci. Technol.*, vol. 20, p. 124015, 2009. doi:10.1088/0957-0233/20/12/124015

S. Kostner, S. van den Driesche, W. Witarski, S. Pastorekova, and M. J. Vellekoop, “Guided dielectrophoresis: a robust method for continuous particle and cell separation.” *IEEE Sens. J.*, vol. 10, pp. 1440–1446, 2010. doi:10.1109/jsen.2010.2044787

S. van den Driesche, V. Rao, D. Puchberger-Enengl, W. Witarski, and M. J. Vellekoop, “Continuous cell from cell separation by traveling wave dielectrophoresis.” *Sens. Actuators B*, 2011. doi:10.1016/j.snb.2011.01.012

S. van den Driesche, W. Witarski, S. Pastorekova, H. Breiteneder, C. Hafner, and M. J. Vellekoop, “A label-free indicator for tumor cells based on the CH_2-stretch ratio.” *Analyst*, 2011. doi:10.1039/c1an15076f

Proceedings International Conferences

S. van den Driesche, W. Witarski, and M. J. Vellekoop, “3.0-3.7 µm infrared sensor system for cell analysis.” in *Proceedings of SPIE vol. 7362*, Dresden, Germany, May 2009, pp. 73 620Y–73 620Y–9. doi:10.1117/12.822058

S. van den Driesche, W. Witarski, and M. J. Vellekoop, “CH_2-symmetric/CH_2-antisymmetric stretch ratio sensor for cell analysis.” in *World Congress on Medical Physics and Biomedical Engineering, September 7 - 12, 2009, Munich, Germany*, ser. IFMBE Proceedings, O. Dössel and W. C. Schlegel, Eds., vol. 25/VIII. Munich, Germany: Springer, Sept. 2009, pp. 15–18.

S. van den Driesche, W. Witarski, C. Hafner, H. Kittler, and M. J. Vellekoop, “A mid infrared led-photodiode based sensor for cell analysis.” in *Proc IEEE Sensors*, Oct. 25-28, 2009, pp. 1562–1566. doi:10.1109/icsens.2009.5398482

S. van den Driesche, S. Kostner, W. Witarski, and M. J. Vellekoop, “A strip electrode design for robust continuous cell separation based on positive and negative dielectrophoresis.” in *Proceedings of the 13th International Conference on Miniaturized Systems for Chemistry and Life Science, μTAS*, Jeju Island, Korea, Nov 2009, pp. 1473–1475.

S. van den Driesche, V. Rao, D. Puchberger, W. Witarski, and M. J. Vellekoop, “Continuous separation of viable cells by travelling wave dielectrophoresis.” in *Procedia Engineering 5*, B. Jakoby and M. J. Vellekoop, Eds. Linz, Austria: Elsevier B.V., Sep 2010, p. 4144. doi:10.1016/j.proeng.2010.09.043

S. van den Driesche, A. Haller, D. Puchberger-Enengl, W. Witarski, and M. J. Vellekoop, “Cell-cell separation of suspended-grown cells by interdigitated triangular electrodes based on negative dielectrophoresis.” in *Proceedings of the Second Conference on Advances in Microfluidics and Nanofluidics and Asian-Pacific International Symposium on Lab on Chip (AMN - APLOC 2011)*, Singapore, January 2011, pp. 22–23.

S. van den Driesche, C. Haiden, W. Witarski, and M. J. Vellekoop, “Mid-infrared CH_2-stretch ratio sensor system for suspended mammalian cells.” in *Proceedings of SPIE (accepted for publication)*, Prague, Czech Republic, April 2011.

A. Hobro, S. van den Driesche, C. Hafner, M. J. Vellekoop, and B. Lendl, “FPA analysis of cancer cells as an assessment of the validity of a quadruple wavelength ’cancer sensor’.” in *Book of Abstract of the SPEC 2010. The 6th International SPEC conference, ”Shedding Light on Disease: Optical Diagnosis for the new Millennium”*, Manchester, UK, June 2010, pp. 92–93.

Utility Model (Gebrauchsmuster)

S. van den Driesche and M. J. Vellekoop, “Vorrichtung zur identifizierung von zellen.” Utility Model DE 20 2009 006 771.8, AT11722(U1), 2009.

Other Publications

S. van den Driesche, S. Kostner, G. Hairer, and M. J. Vellekoop, “Microfluidics as a tool for in-flow single cell positioning.” in *Abstracts book of the FTIR Spectroscopy in Microbiological and Medical Diagnostics workshop*, Berlin, Germany, Oct 2007, p. 73620Y.

S. van den Driesche and M. J. Vellekoop, “A sensor concept for label-free cell analysis.” in *GMe Forum 2008 - Proceedings of the Seminar at the Vienna University Of Technology*, K. Riedling, Ed., Vienna, Austria, Oct. 2009, pp. 139–143.

S. van den Driesche and M. J. Vellekoop, “Quadruple wavelength infrared sensor for label-free tumour screening.” in *Proceedings of the ARGE Sensorik PhD-Summit 2009*, B. Jakoby, Ed., 2010, pp. 20–26.

Supervision of Students

D. Puchberger-Enengl, “Dielectrophoresis-based characterization and separation of cells.” Master’s thesis, Vienna University of Technology, 2009.

V. Rao, “Travelling wave dielectrophoresis: simulations and design.” Vienna University of Technology, 2010.

C. Haiden, “IR-absorption measurements for discrimination of mammalian cells.” Master’s thesis, Vienna University of Technology, 2010.

H. Zirath, “Separation of viable cells from bacteria contaminated cell cultures by traveling wave dielectrophoresis.” Master’s thesis, Vienna University of Technology, 2011.

Publications Related to other Projects

Journal Papers

I. Giouroudi, S. van den Driesche, J. Kosel, R. Grössinger, and M. J. Vellekoop, “On-chip bio-analyte detection utilizing the velocity of magnetic microparticles in a fluid.” *J. Appl. Phys.*, vol. 109, 2011. doi:10.1063/1.3556952

Proceedings International Conferences

N. Moscelli, S. van den Driesche, and M. J. Vellekoop, “A position control system of a microfluidic sample flow.” in *Proceedings of the MicroMechanics Europe, MME*, Toulouse, France, sept 2009, pp. A11–1 – A11–4.

I. Giouroudi, S. van den Driesche, and J. Kosel, “Biosensing utilizing the motion of magnetic microparticles in a microfluidic system.” in *Procedia Engineering 5*, Linz, Austria, Sep 2010, pp. 824–827. doi:10.1016/j.proeng.2010.09.235

N. Moscelli, S. van den Driesche, W. Witarski, F. Iuliano, and M. J. Vellekoop, “A real-time monitoring system for adherently grown cells.” in *Procedia Engineering 5*, Linz, Austria, Sep 2010, pp. 492–495. doi:10.1016/j.proeng.2010.09.154

I. Giouroudi, S. van den Driesche, J. Kosel, and R. Grössinger, “On chip pathogen detection utilizing the velocity decrease of magnetic microparticles.” in *Proceedings of the 55th Conference on Magnetism and Magnetic Materials*, Atlanta, Georgia, USA, November 2010.

N. Moscelli, S. van den Driesche, W. Witarski, and M. J. Vellekoop, “A real-time cell proliferation and motility monitoring system.” in *Proceedings of Biodevices 2011 Conference*, Rome, Italy, Jan 2011.

N. Moscelli, W. Witarski, S. van den Driesche, and M. J. Vellekoop, “In incubator live cell imaging platform.” in *Proceedings of SPIE (accepted for publication)*, Prague, Czech Republic, April 2011.

Bibliography

[1] M. J. Horner, L. A. G. Ries, M. Krapcho, N. Neyman, R. Aminou, N. Howlader, S. F. Altekruse, E. J. Feuer, L. Huang, A. Mariotto, B. A. Miller, D. R. Lewis, M. P. Eisner, D. G. Stinchcomb, and B. K. Edwards. (2009) Seer cancer statistics review, 1975-2006. National Cancer Institute. Bethesda, MD.

[2] R. D. Lillie, *Histopathologic technic and practical histochemistry.*, 4th ed., H. M. Fullmer, Ed. New York: McGraw-Hill Inc., 1976.

[3] M. H. Stoler and M. Schiffman, "Interobserver reproducibility of cervical cytologic and histologic interpretations: realistic estimates from the ASCUS-LSIL triage study." *JAMA*, vol. 285, pp. 1500–1505, 2001. doi:10.1001/jama.285.11.1500

[4] C. Urso, F. Rongioletti, D. Innocenzi, C. Saieva, D. Batolo, S. C. R. F. R. G. M. Lentini, C. T. A. Rebora, and M. Pippione, "Interobserver reproducibility of histological features in cutaneous malignant melanoma." *J. Clin. Pathol.*, vol. 58, pp. 1194–1198, 2005. doi:doi:10.1136/jcp.2005.026765

[5] A. Nezos, P. Lembessis, A. Sourla, N. Pissimissis, H. Gogas, and M. Koutsilieris, "Molecular markers detecting circulating melanoma cells by reverse transcription polymerase chain reaction: methodological pitfalls and clinical relevance." *Clin. Chem. Lab. Med.*, vol. 47, pp. 1–11, 2009. doi:10.1515/CCLM.2009.009

[6] J. L. Young, S. D. Roffers, L. A. G. Ries, A. G. Fritz, and A. A. Hurlbut. (2001) SEER summary staging manual - 2000: Codes and coding instructions. National Cancer Institute. Bethesda, MD. NIH Pub. No. 01-4969.

[7] M. Berwick and C. Wiggins, "The current epidemiology of cutaneous malignant melanoma." *Front. Biosci.*, vol. 11, pp. 1244–1254, 2006. doi:10.2741/1877

[8] C. Garbe and T. K. Eigentler, "Diagnosis and treatment of cutaneous melanoma: state of the art 2006." *Melanoma Res.*, vol. 17, no. 2, pp. 117–127, Apr 2007. doi:10.1097/CMR.0b013e328042bb36

[9] P. E. LeBoit, G. Burg, D. Weedon, and A. Sarasain, Eds., *Pathology and genetics of skin tumours.* World Health Organization, 2006.

[10] S. Boyden, "The chemotactic effect of mixtures of antibody and antigen on polymorphonuclear leucocytes." *J. Exp. Med.*, vol. 115, pp. 453–466, Mar 1962.

[11] H. C. Chen, "Boyden chamber assay." *Methods Mol. Biol.*, vol. 294, pp. 15–22, 2005.

[12] M. Tarantola, A.-K. Marel, E. Sunnick, H. Adam, J. Wegener, and A. Janshoff, "Dynamics of human cancer cell lines monitored by electrical and acoustic fluctuation analysis." *Integr. Biol.*, vol. 2, no. 2-3, pp. 139–150, Mar 2010. doi:10.1039/b920815a

[13] S. Chen, T. Zheng, M. R. Shortreed, C. Alexander, and L. M. Smith, "Analysis of cell surface carbohydrate expression patterns in normal and tumorigenic human breast cell lines using lectin arrays." *Anal. Chem.*, vol. 79, pp. 5698–5702, 2007. doi:10.1021/ac070423k

[14] L. M. R. Ferreira, "Cancer metabolism: the warburg effect today." *Exp. Mol. Pathol.*, vol. 89, no. 3, pp. 372–380, Dec 2010. doi:10.1016/j.yexmp.2010.08.006

[15] X. T. Zheng, H. B. Yang, and C. M. Li, "Optical detection of single cell lactate release for cancer metabolic analysis." *Anal. Chem.*, vol. 82, no. 12, pp. 5082–5087, Jun 2010. doi:10.1021/ac100074n

[16] P. M. Schmidt, C. Lehmann, E. Matthes, and F. F. Bier, "Detection of activity of telomerase in tumor cells using fiber optical biosensors." *Biosens. Bioelectron.*, vol. 17, no. 11-12, pp. 1081–1087, Dec 2002. doi:10.1016/S0956-5663(02)00102-1

[17] J. W. Shay, Y. Zou, E. Hiyama, and W. E. Wright, "Telomerase and cancer." *Hum. Mol. Genet.*, vol. 10, no. 7, pp. 677–685, Apr 2001. doi:10.1093/hmg/10.7.677

[18] R. de la Rica, S. Thompson, A. Baldi, C. Fernandez-Sanchez, C. M. Drain, and H. Matsui, "Label-free cancer cell detection with impedimetric transducers." *Anal. Chem.*, vol. 81, pp. 10 167–10 171, 2009. doi:10.1021/ac9021049

[19] O. Y. Henry, A. Fragoso, V. Beni, N. Laboria, J. L. A. Snchez, D. Latta, F. V. Germar, K. Drese, I. Katakis, and C. K. O'Sullivan, "Design and testing of a packaged microfluidic cell for the multiplexed electrochemical detection of cancer markers." *Electrophoresis*, vol. 30, no. 19, pp. 3398–3405, Oct 2009. doi:10.1002/elps.200900368

[20] H. Lee, T.-J. Yoon, J.-L. Figueiredo, F. K. Swirski, and R. Weissleder, "Rapid detection and profiling of

cancer cells in fine-needle aspirates." *Proc. Natl. Acad. Sci. U. S. A.*, vol. 106, no. 30, pp. 12 459–12 464, Jul 2009. doi:10.1073/pnas.0902365106

[21] M. J. Vellekoop, "The emergence of physical chemosensors and biosensors." in *Proc. Transducers*, Munich, 2001.

[22] M. J. Vellekoop, *Smart sensor systems*, G. C. M. Meijer, Ed. John Wiley & Sons, 2008.

[23] S. K. Patra and S. Bettuzzi, "Epigenetic DNA-methylation regulation of genes coding for lipid raft-associated components: a role for raft proteins in cell transformation and cancer progression (review)." *Oncol. Rep.*, vol. 17, no. 6, pp. 1279–1290, Jun 2007.

[24] L. S. Friedman, E. A. Ostermeyer, C. I. Szabo, P. Dowd, E. D. Lynch, S. E. Rowell, and M. C. King, "Confirmation of brca1 by analysis of germline mutations linked to breast and ovarian cancer in ten families." *Nat. Genet.*, vol. 8, no. 4, pp. 399–404, Dec 1994. doi:10.1038/ng1294-399

[25] F. Schroeder and J. M. Gardiner, "Membrane lipids and enzymes of cultured high- and low-metastatic B16 melanoma variants." *Cancer Res.*, vol. 44, pp. 3262–3269, 1984.

[26] L. K. Tamm and S. A. Tatulian, "Infrared spectroscopy of proteins and peptides in lipid bilayers." *Q. Rev. Biophys.*, vol. 30, pp. 365–429, 1997. doi:10.1017/S003358359700337

[27] M. Fritzsche and C. F. Mandenius, "Fluorescent cell-based sensing approaches for toxicity testing." *Anal. Bioanal. Chem.*, vol. 398, pp. 181–191, 2010. doi:10.1007/s00216-010-3651-6

[28] J. Wiedenmann, F. Oswald, and G. U. Nienhaus, "Fluorescent proteins for live cell imaging: opportunities, limitations, and challenges." *IUBMB Life*, vol. 61, pp. 1029–1042, 2009. doi:10.1002/iub.256

[29] E. A. Widder, "Bioluminescence in the ocean: origins of biological, chemical, and ecological diversity." *Science*, vol. 328, no. 5979, pp. 704–708, May 2010. doi:10.1126/science.1174269

[30] K. E. Luker and G. D. Luker, "Bioluminescence imaging of reporter mice for studies of infection and inflammation." *Antiviral Res.*, vol. 86, pp. 93–100, 2010. doi:10.1016/j.antiviral.2010.02.002

[31] D. A. Proshlyakov, "UV optical absorption by protein radicals in cytochrome c oxidase." *Biochim. Biophys. Acta*, vol. 1655, pp. 282–289, 2004. doi:10.1016/j.bbabio.2003.10.014

[32] D. Markovitsi, T. Gustavsson, and A. Banyasz, "Absorption of UV radiation by DNA: spatial and temporal features." *Mutation Research/Reviews in Mutation Research*, vol. 704, pp. 21–28, 2010. doi:10.1016/j.mrrev.2009.11.003

[33] J. Chow and V. A. Tron, "Molecular aspects of ultraviolet radiation-induced apoptosis in the skin." *J. Cutan. Med. Surg.*, vol. 9, no. 6, pp. 289–295, Dec 2005. doi:10.1007/s10227-005-0109-0

[34] C. Cao and Y. Wan, "Parameters of protection against ultraviolet radiation-induced skin cell damage." *J. Cell. Physiol.*, vol. 220, no. 2, pp. 277–284, Aug 2009. doi:10.1002/jcp.21780

[35] P. A. Tipler, *Physics for scientists and engineers.*, 4th ed. W. H. Freeman, 1999.

[36] R. Rigler, "Fluorescence and single molecule analysis in cell biology." *Biochem. Biophys. Res. Commun.*, vol. 396, no. 1, pp. 170–175, May 2010. doi:10.1016/j.bbrc.2010.04.070

[37] J. W. Taraska and W. N. Zagotta, "Fluorescence applications in molecular neurobiology." *Neuron*, vol. 66, no. 2, pp. 170–189, Apr 2010. doi:10.1016/j.neuron.2010.02.002

[38] Invitrogen, "Molecular probes - the handbook." [Online]. Available: http://www.invitrogen.com

[39] "Database of fluorescent dyes properties and applications." [Online]. Available: http://www.fluorophores.org

[40] Invitrogen, "Manuals & protocols: vybrant cell-labeling solutions." [Online]. Available: http://probes.invitrogen.com/media/pis/mp22885.pdf

[41] R. Richards-Kortum and E. Sevick-Muraca, "Quantitative optical spectroscopy for tissue diagnosis." *Annu. Rev. Phys. Chem.*, vol. 47, pp. 555–606, 1996. doi:10.1146/annurev.physchem.47.1.555

[42] J. Talbot, J. N. Barrett, E. F. Barrett, and G. David, "Stimulation-induced changes in NADH fluorescence and mitochondrial membrane potential in lizard motor nerve terminals." *J. Physiol.*, vol. 579, no. Pt 3, pp. 783–798, Mar 2007. doi:10.1113/jphysiol.2006.126383

[43] R. J. Verbunt, M. A. Fitzmaurice, J. R. Kramer, N. B. Ratliff, C. Kittrell, P. Taroni, R. M. Cothren, J. Baraga, and M. Feld, "Characterization of ultraviolet laser-induced autofluorescence of ceroid deposits and other structures in atherosclerotic plaques as a potential diagnostic for laser angiosurgery." *Am. Heart J.*, vol. 123, no. 1, pp. 208–216, Jan 1992. doi:10.1016/0002-8703(92)90767-P

[44] P. N. Prasad, *Introduction to biophotonics.* Hoboken, New Jersey: John Wiley & Sons, 2003.

[45] H. W. Rhee, H. Y. Choi, K. Han, and J. I. Hong, "Selective fluorescent detection of flavin adenine dinucleotide in human eosinophils by using bis(zn2+-dipicolylamine) complex." *J. Am. Chem. Soc.*, vol. 129, no. 15, pp. 4524–4525, Apr 2007. doi:10.1021/ja070026r

[46] R. Y. Tsien, "The green fluorescent protein." *Annu. Rev. Biochem.*, vol. 67, pp. 509–544, 1998. doi:10.1146/annurev.biochem.67.1.509

[47] B. R. Martin, B. N. G. Giepmans, S. R. Adams, and R. Y. Tsien, "Mammalian cell-based optimization

of the biarsenical-binding tetracysteine motif for improved fluorescence and affinity." *Nat. Biotechnol.*, vol. 23, no. 10, pp. 1308–1314, Oct 2005. doi:10.1038/nbt1136

[48] N. C. Shaner, M. Z. Lin, M. R. McKeown, P. A. Steinbach, K. L. Hazelwood, M. W. Davidson, and R. Y. Tsien, "Improving the photostability of bright monomeric orange and red fluorescent proteins." *Nat. Methods*, vol. 5, no. 6, pp. 545–551, Jun 2008. doi:10.1038/nmeth.1209

[49] S. B. Primrose, R. M. Twyman, and R. W. Old, *Principles of gene manipulation.*, 6th ed. Oxford ; Malden, MA: Blackwell Science, 2001.

[50] J. A. Prescher and C. H. Contag, "Guided by the light: visualizing biomolecular processes in living animals with bioluminescence." *Curr. Opin. Chem. Biol.*, vol. 14, no. 1, pp. 80–89, Feb 2010. doi:10.1016/j.cbpa.2009.11.001

[51] D. W. Ow, J. R. D. Wet, D. R. Helinski, S. H. Howell, K. V. Wood, and M. Deluca, "Transient and stable expression of the firefly luciferase gene in plant cells and transgenic plants." *Science*, vol. 234, no. 4778, pp. 856–859, Nov 1986. doi:10.1126/science.234.4778.856

[52] J. R. de Wet, K. V. Wood, M. DeLuca, D. R. Helinski, and S. Subramani, "Firefly luciferase gene: structure and expression in mammalian cells." *Mol. Cell. Biol.*, vol. 7, no. 2, pp. 725–737, Feb 1987.

[53] V. R. Viviani, "The origin, diversity, and structure function relationships of insect luciferases." *Cell. Mol. Life Sci.*, vol. 59, no. 11, pp. 1833–1850, Nov 2002. doi:10.1007/PL00012509

[54] J. C. Day, L. C. Tisi, and M. J. Bailey, "Evolution of beetle bioluminescence: the origin of beetle luciferin." *Luminescence*, vol. 19, no. 1, pp. 8–20, 2004. doi:10.1002/bio.749

[55] V. R. Viviani, F. G. C. Arnoldi, A. J. S. Neto, T. L. Oehlmeyer, E. J. H. Bechara, and Y. Ohmiya, "The structural origin and biological function of ph-sensitivity in firefly luciferases." *Photochem. Photobiol. Sci.*, vol. 7, no. 2, pp. 159–169, Feb 2008. doi:10.1039/b714392c

[56] H. M. Shapiro, *Practical flow cytometry.*, 4th ed. John Wiley & Sons, Inc., 2003.

[57] F. Träger, *Springer handbook of lasers and optics.* Springer, 2007.

[58] G. D. Fasman, *Handbook of biochemistry and molecular biology, physical and chemical data, vol. 1.*, 3rd ed. CRC Press, 1976.

[59] C. N. Pace, F. Vajdos, G. G. L. Fee, and T. Gray, "How to measure and predict the molar absorption coefficient of a protein." *Protein Sci.*, vol. 4, pp. 2411–2423, 1995. doi:10.1002/pro.5560041120

[60] L. M. Ng and R. Simmons, "Infrared spectroscopy." *Anal. Chem.*, vol. 71, pp. 343–350, 1999. doi:10.1021/a1999908r

[61] J. Dubois and R. A. Shaw, "Peer reviewed:IR spectroscopy in clinical and diagnostic applications." *Anal. Chem.*, vol. 76, pp. 360–367, 2004. doi:10.1021/ac041647v

[62] D. Naumann, "FT-infrared and FT-raman spectroscopy in biomedical research." *Appl. Spectrosc. Rev.*, vol. 36, pp. 239–298, 2001. doi:10.1081/ASR-100106157

[63] T. D. Wang, G. Triadafilopoulos, J. M. Crawford, L. R. Dixon, T. Bhandari, P. Sahbaie, S. Friedland, R. Soetikno, and C. H. Contag, "Detection of endogenous biomolecules in barretts esophagus by fourier transform infrared spectroscopy." *Proc. Natl. Acad. Sci. U. S. A.*, vol. 104, pp. 15 864–15 869, 2007. doi:10.1073/pnas.0707567104

[64] R. J. Anderson, D. Bendell, P. W. Groundwater, and E. W. Abel, *Organic Spectroscopic Analysis.* Royal Society of Chemistry, 2004.

[65] J. W. Suggs, *Organic chemistry.* Barron's Educational Series, 2001.

[66] C. M. Bender and T. T. Wu, "Anharmonic oscillator." *Phys. Rev.*, vol. 184, no. 5, pp. 1231–1260, Aug 1969. doi:10.1103/PhysRev.184.1231

[67] D. S. Eisenberg and W. Kauzmann, *The structure and properties of water.* Oxford University Press, 2005.

[68] P. Lasch, M. Boese, A. Pacifico, and M. Diem, "FT-IR spectroscopic investigations of single cells on the subcellular level." *Vib. Spectrosc.*, vol. 28, pp. 147–157, 2002. doi:10.1016/S0924-2031(01)00153-9

[69] B. Rigas, S. Morgello, I. S. Goldman, and P. T. Wong, "Human colorectal cancers display abnormal fourier-transform infrared spectra." *Proc. Natl. Acad. Sci. U. S. A.*, vol. 87, pp. 8140–8144, 1990.

[70] D. E. Maziak, M. T. Do, F. M. Shamji, S. R. Sundaresan, D. G. Perkins, and P. T. T. Wong, "Fourier-transform infrared spectroscopic study of characteristic molecular structure in cancer cells of esophagus: an exploratory study." *Cancer Detect Prev.*, vol. 31, pp. 244–253, 2007. doi:10.1016/j.cdp.2007.03.003

[71] J. Anastassopoulou, E. Boukaki, C. Conti, P. Ferraris, E. Giorgini, C. Rubini, S. Sabbatini, T. Theophanides, and G. Tosi, "Microimaging FT-IR spectroscopy on pathological breast tissues." *Vib. Spectrosc.*, vol. 51, pp. 270–275, 2009. doi:10.1016/j.vibspec.2009.07.005

[72] H. Fabian, N. A. Thi, M. Eiden, P. Lasch, J. Schmitt, and D. Naumann, "Diagnosing benign and malignant lesions in breast tissue sections by using IR-microspectroscopy." *Biochim. Biophys. Acta*, vol. 1758, pp. 874–882, 2006. doi:10.1016/j.bbamem.2006.05.015

[73] A. Zwielly, J. Gopas, G. Brkicb, and S. Mordechai, “Discrimination between drug-resistant and non-resistant human melanoma cell lines by FTIR spectroscopy.” *Analyst*, vol. 134, p. 294300, 2009. doi:10.1039/b805223a

[74] W. A. Schulz, *Molecular biology of human cancers (An advanced student’s text).* Springer, 2005.

[75] H. Heller, M. Schaefer, and K. Schulten, “Molecular dynamics simulation of a bilayer of 200 lipids in the gel and in the liquid crystal phase.” *J. Phys. Chem. B*, vol. 97, pp. 8343–8360, 1993. doi:10.1021/j100133a034

[76] M. J. Piccart, W. C. Wood, C. M. Hung, J. L. Solin, and F. Cardoso, *Breast cancer and molecular medicine.*, U. Heilmann, Ed. Springer, 2006.

[77] C. Ohe, T. Sasaki, M. Noi, Y. Goto, and K. Itoh, “Sum frequency generation spectroscopic study of the condensation effect of cholesterol on a lipid monolayer.” *Anal. Bioanal. Chem.*, vol. 388, pp. 73–79, 2007. doi:10.1007/s00216-006-1030-0

[78] C. Cai, H. Zhu, and J. Chen, “Overexpression of caveolin-1 increases plasma membrane fluidity and reduces p-glycoprotein function in Hs578T/Dox.” *Biochem. Biophys. Res. Commun.*, vol. 320, p. 868874, 2004. doi:10.1016/j.bbrc.2004.06.030

[79] P. Guyot-Sionnest, J. H. Hunt, and Y. R. Shen, “Sum-frequency vibrational spectroscopy of a langmuir film: study of molecular orientation of a two-dimensional system.” *Phys. Rev. Lett.*, vol. 59, no. 14, pp. 1597–1600, 1987. doi:10.1103/PhysRevLett.59.1597

[80] S. J. Blanksby and G. B. Ellison, “Bond dissociation energies of organic molecules.” *Acc. Chem. Res.*, vol. 36, no. 4, pp. 255–263, Apr 2003. doi:10.1021/ar020230d

[81] S. N. Eğe, *Organic Chemistry.*, 4th ed. Houghton Mifflin Company, 1999.

[82] Z. Arsov and L. Quaroni, “Direct interaction between cholesterol and phosphatidylcholines in hydrated membranes revealed by ATR-FTIR spectroscopy.” *Chem. Phys. Lipids*, vol. 150, no. 1, pp. 35–48, 2007. doi:10.1016/j.chemphyslip.2007.06.215

[83] M. Pasenkiewicz-Gierula, T. Róg, K. Kitamura, and A. Kusumi, “Cholesterol effects on the phosphatidylcholine bilayer polar region: a molecular simulation study.” *Biophys. J.*, vol. 78, pp. 1376–1389, 2000. doi:10.1016/S0006-3495(00)76691-4

[84] A. Rothnie, D. Theron, L. Soceneantu, C. Martin, M. Traikia, G. Berridge, C. F. Higgins, P. F. Devaux, and R. Callaghan, “The importance of cholesterol in maintenance of p-glycoprotein activity and its membrane perturbing influence.” *Eur. Biophys. J.*, vol. 30, pp. 430–442, 2001. doi:10.1007/s002490100156

[85] A. Kusumi, M. Tsuda, T. Akino, S. Ohnishi, and Y. Terayama, “Protein-phospholipid-cholesterol interaction in the photolysis of invertebrate rhodopsin.” *Biochemistry*, vol. 22, no. 5, p. 11651170, 1983. doi:10.1021/bi00274a027

[86] O. G. Mouritsen and K. Jørgensen, “Dynamical order and disorder in lipid bilayers.” *Chem. Phys. Lipids*, vol. 73, pp. 3–25, 1994. doi:10.1016/0009-3084(94)90171-6

[87] G. Vanderkooi, “Computation of mixed phosphatidylcholine-cholesterol bilayer structures by energy minimization.” *Biophys. J.*, vol. 66, no. 5, pp. 1457–1468, 1994. doi:10.1016/S0006-3495(94)80936-1

[88] “Cdc/national center for health statistics.”

[89] M. Kriege, C. T. M. Brekelmans, H. Peterse, I. M. Obdeijn, C. Boetes, H. M. Zonderland, S. H. Muller, T. Kok, R. A. Manoliu, A. P. E. Besnard, M. M. A. Tilanus-Linthorst, C. Seynaeve, C. C. M. Bartels, S. Meijer, J. C. Oosterwijk, N. Hoogerbrugge, R. A. E. M. Tollenaar, H. J. de Koning, E. J. T. Rutgers, and J. G. M. Klijn, “Tumor characteristics and detection method in the MRISC screening program for the early detection of hereditary breast cancer.” *Breast Cancer Res. Treat.*, vol. 102, pp. 357–363, 2007. doi:10.1007/s10549-006-9341-6

[90] S. van den Driesche, W. Witarski, and M. J. Vellekoop, “3.0-3.7 µm infrared sensor system for cell analysis.” in *Proceedings of SPIE vol. 7362*, Dresden, Germany, May 2009, pp. 73 620Y–73 620Y–9. doi:10.1117/12.822058

[91] S. van den Driesche, W. Witarski, S. Pastorekova, and M. J. Vellekoop, “A quadruple wavelength IR sensor system for label-free tumour screening.” *Meas. Sci. Technol.*, vol. 20, p. 124015, 2009. doi:10.1088/0957-0233/20/12/124015

[92] C. Krafft, K. Thmmler, S. B. Sobottka, G. Schackert, and R. Salzer, “Classification of malignant gliomas by infrared spectroscopy and linear discriminant analysis.” *Biopolymers*, vol. 82, pp. 301–305, 2006. doi:10.1002/bip.20492

[93] S. van den Driesche, W. Witarski, S. Pastorekova, H. Breiteneder, C. Hafner, and M. J. Vellekoop, “A label-free indicator for tumor cells based on the CH_2-stretch ratio.” *Analyst*, 2011. doi:10.1039/c1an15076f

[94] T. Rg, M. Pasenkiewicz-Gierula, I. Vattulainen, and M. Karttunen, “Ordering effects of cholesterol and

its analogues." *Biochim. Biophys. Acta*, vol. 1788, no. 1, pp. 97–121, Jan 2009. doi:10.1016/j.bbamem.2008.08.022

[95] F. de Meyer and B. Smit, "Effect of cholesterol on the structure of a phospholipid bilayer." *Proc. Natl. Acad. Sci. U. S. A.*, vol. 106, no. 10, pp. 3654–3658, Mar 2009. doi:10.1073/pnas.0809959106

[96] M. Bonn, S. Roke, O. Berg, L. B. F. Juurlink, A. Stamouli, and M. Müller, "A molecular view of cholesterol-induced condensation in a lipid monolayer." *J. Phys. Chem. B*, vol. 108, pp. 19 083–19 085, 2004. doi:10.1021/jp0452249

[97] E. P. Kilsdonk, P. G. Yancey, G. W. Stoudt, F. W. Bangerter, W. J. Johnson, M. C. Phillips, and G. H. Rothblat, "Cellular cholesterol efflux mediated by cyclodextrins." *J. Biol. Chem.*, vol. 270, p. 1725017256, 1995. doi:10.1074/jbc.270.29.17250

[98] S. K. Rodal, G. Skretting, Ø. Garred, F. Vilhardt, B. van Deurs, and K. Sandvig, "Extraction of cholesterol with methyl-β-cyclodextrin perturbs formation of clathrin-coated endocytic vesicles." *Mol. Biol. Cell*, vol. 10, p. 961974, 1999.

[99] G. L. Patrick, *An introduction to medicinal chemistry*, 2nd ed. Oxford, New York: Oxford University Press, 2001.

[100] M. M. Wright and C. R. McMaster, "Phospholipid synthesis, diacylglycerol compartmentation, and apoptosis." *Biol. Res.*, vol. 35, no. 2, pp. 223–229, 2002.

[101] S. Baritaki, S. Apostolakis, P. Kanellou, M. T. Dimanche-Boitrel, D. A. Spandidos, and B. Bonavida, "Reversal of tumor resistance to apoptotic stimuli by alteration of membrane fluidity: therapeutic implications." *Adv. Cancer Res.*, vol. 98, pp. 149–190, 2007. doi:10.1016/S0065-230X(06)98005-1

[102] G. Chu, "Cellular responses to cisplatin. the roles of DNA-binding proteins and DNA repair." *J. Biol. Chem.*, vol. 269, pp. 787–790, 1994.

[103] G. Chu, R. Mantin, Y. M. Shen, G. Baskett, and H. Sussman, "Massive cisplatin overdose by accidental substitution for carboplatin. toxicity and management." *Cancer*, vol. 72, no. 12, pp. 3707–3714, Dec 1993. doi:10.1002/1097-0142

[104] A. Rebillard, X. Tekpli, O. Meurette, O. Sergent, G. LeMoigne-Muller, L. Vernhet, M. Gorria, M. Chevanne, M. Christmann, B. Kaina, L. Counillon, E. Gulbins, D. Lagadic-Gossmann, and M. Dimanche-Boitrel, "Cisplatin-induced apoptosis involves membrane fluidification via inhibition of NHE1 in human colon cancer cells." *Cancer Res.*, vol. 67, pp. 7865–7874, 2007. doi:10.1158/0008-5472.CAN-07-0353

[105] S. Lacour, A. Hammann, S. Grazide, D. Lagadic-Gossmann, A. Athias, O. Sergent, G. Laurent, P. Gambert, E. Solary, and M. Dimanche-Boitrel, "Cisplatin-induced CD95 redistribution into membrane lipid rafts of HT29 human colon cancer cells." *Cancer Res*, vol. 64, p. 35933598, 2004.

[106] J. K. Singh, A. Dasgupta, T. Adayev, S. A. Shahmehdi, D. Hammond, and P. Banerjee, "Apoptosis is associated with an increase in saturated fatty acid containing phospholipids in the neuronal cell line, HN2-5." *Biochim. Biophys. Acta*, vol. 1304, pp. 171–178, 1996. doi:10.1016/S0005-2760(96)00134-8

[107] S. A. Francis, J. M. Kelly, J. McCormack, R. A. Rogers, J. Lai, E. E. Schneeberger, and R. D. Lynch, "Rapid reduction of mdck cell cholesterol by methyl-beta-cyclodextrin alters steady state transepithelial electrical resistance." *Eur. J. Cell Biol.*, vol. 78, pp. 473–484, 1999.

[108] S. Kamau, S. Krämer, M. Günthert, and H. Wunderli-Allenspach, "Effect of the modulation of the membrane lipid composition on the localization and function of p-glycoprotein in MDR1-MDCK cells." *In Vitro Cell Dev. Bio.l Anim.*, vol. 41, pp. 207–216, 2005. doi:10.1290/0502016.1

[109] J. Szejtli, "Past, present, and future of cyclodextrin research*," *Pure Appl. Chem.*, vol. 76, pp. 1825–1845., 2004. doi:10.1002/chin.200517261

[110] P. G. Yancey, W. V. Rodrigueza, E. P. Kilsdonk, G. W. Stoudt, W. J. Johnson, M. C. Phillips, and G. H. Rothblat, "Cellular cholesterol efflux mediated by cyclodextrins. demonstration of kinetic pools and mechanism of efflux." *J. Biol. Chem.*, vol. 271, no. 27, pp. 16 026–16 034, Jul 1996. doi:10.1074/jbc.271.27.16026

[111] P. Danthi and M. Chow, "Cholesterol removal by methyl-beta-cyclodextrin inhibits poliovirus entry." *J. Virol.*, vol. 78, no. 1, pp. 33–41, Jan 2004. doi:10.1128/JVI.78.1.3341.2004

[112] E. P. Kilsdonk, P. G. Yancey, G. W. Stoudt, F. W. Bangerter, W. J. Johnson, M. C. Phillips, and G. H. Rothblat, "Cellular cholesterol efflux mediated by cyclodextrins." *J. Biol. Chem.*, vol. 270, no. 29, pp. 17 250–17 256, Jul 1995. doi:10.1074/jbc.270.29.17250

[113] Data obtained from the comment section of product details atcc htb-46.

[114] C. Heuber, F. Formaggio, C. Baldini, C. Toniolo, and K. Müller, "Multinuclear solid-state-NMR and FT-IR-absorption investigations on lipid/trichogin bilayers." *Chem. Biodiversity*, vol. 4, no. 6, pp. 1200–1218, 2007. doi:10.1002/cbdv.200790105

[115] D. J. Moore, A. Gericke, and R. Mendelsohn, "Fluctuations in IR spectral parameters detected in mixed

acyl chain membranes of *Acholeplasma laidlawii B*." *Biochim. Biophys. Acta*, vol. 1279, pp. 49–57, 1996. doi:10.1016/0005-2736(95)00243-X

[116] E. E. Lawson, A. N. C. Anigbogu, A. C. Williams, B. W. Barry, and H. G. M. Edwards, "Thermally induced molecular disorder in human stratum corneum lipids compared with a model phospholipid system FT-Raman spectroscopy." *Spectrochim. Acta A*, vol. 54, p. 543558, 1998. doi:10.1016/S1386-1425(97)00268-0

[117] J. V. Swinnen, H. Heemers, T. van de Sande, E. de Schrijver, K. Brusselmans, W. Heyns, and G. Verhoeven, "Androgens, lipogenesis and prostate cancer." *J. Steroid Biochem. Mol. Biol.*, vol. 92, no. 4, pp. 273–279, Nov 2004. doi:10.1016/j.jsbmb.2004.10.013

[118] K. Simons and E. Ikonen, "Functional rafts in cell membranes." *Nature*, vol. 387, pp. 569–572, 1997. doi:10.1038/42408

[119] S. Y. Venyaminov and F. G. Prendergast, "Water (H_2O and D_2O) molar absorptivity in the 1000-4000 cm^{-1} range and quantitative infrared spectroscopy of aqueous solutions." *Anal. Biochem.*, vol. 248, pp. 234–245, 1997. doi:10.1006/abio.1997.2136

[120] "http://www.korth.de." [Online]. Available: www.korth.de

[121] S. Kulka, N. Kaun, J. R. Baena, J. Frank, P. Svasek, D. Moss, M. J. Vellekoop, and B. Lendl, "Mid-IR synchrotron radiation for molecular specific detection in microchip-based analysis systems." *Anal. Bioanal. Chem.*, vol. 378, no. 7, pp. 1735–1740, Apr 2004. doi:10.1007/s00216-004-2534-0

[122] P. Hinsmann, J. Frank, P. Svasek, M. Harasek, and B. Lendl, "Design, simulation and application of a new micromixing device for time resolved infrared spectroscopy of chemical reactions in solution." *Lab Chip*, vol. 1, no. 1, pp. 16–21, Sep 2001. doi:10.1039/b104391a

[123] M. Kölhed, P. Hinsmann, P. Svasek, J. Frank, B. Karlberg, and B. Lendl, "On-line fourier transform infrared detection in capillary electrophoresis." *Anal. Chem.*, vol. 74, no. 15, pp. 3843–3848, Aug 2002.

[124] P. Svasek, E. Svasek, B. Lendl, and M. J. Vellekoop, "Fabrication of miniaturized fluidic devices using SU-8 based lithography and low temperature wafer bonding." *Sens. Actuators A*, vol. 115, pp. 591–599, 2004. doi:10.1016/j.sna.2004.03.055

[125] H. B. Mann and D. R. Whitney, "On a test of whether one of two random variables is stochastically larger than the other." *Ann. Math. Statist.*, vol. 18, pp. 50–60, 1947. doi:10.1214/aoms/1177730491

[126] A. Pevsner and M. Diem, "Infrared spectroscopic studies of major cellular components. part I: The effect of hydration on the spectra of proteins." *Appl. Spectrosc.*, vol. 55, pp. 788–793, 2001. doi:10.1366/0003702011952497

[127] A. Pevsner and M. Diem, "IR spectroscopic studies of major cellular components. III. hydration of protein, nucleic acid, and phospholipid films." *Biopolymers*, vol. 72, no. 4, pp. 282–289, 2003. doi:10.1002/bip.10416

[128] J. R. Mourant, R. R. Gibson, T. M. Johnson, S. Carpenter, K. W. Short, Y. R. Yamada, and J. P. Freyer, "Methods for measuring the infrared spectra of biological cells." *Phys. Med. Biol.*, vol. 48, pp. 243–257, 2003. doi:10.1088/0031-9155/48/2/307

[129] A. Y. Fu, C. Spence, A. Scherer, F. H. Arnold, and S. R. Quake, "A microfabricated fluorescence-activated cell sorter." *Nat. Biotechnol.*, vol. 17, no. 11, pp. 1109–1111, Nov 1999. doi:10.1038/15095

[130] S. F. Ibrahim and G. van den Engh, "Flow cytometry and cell sorting." *Adv. Biochem. Engin. Biotechnol.*, vol. 106, pp. 19–39, 2007. doi:10.1007/10.2007.073

[131] S. H. Cho, C. H. Chen, F. S. Tsai, J. M. Godin, and Y.-H. Lo, "Human mammalian cell sorting using a highly integrated micro-fabricated fluorescence-activated cell sorter (μfacs)." *Lab Chip*, vol. 10, no. 12, pp. 1567–1573, Jun 2010. doi:10.1039/c000136h

[132] I. Safarik and M. Safarikova, "Use of magnetic techniques for the isolation of cells." *J. Chromatogr. B*, vol. 722, pp. 33–53, 1999. doi:10.1016/S0378-4347(98)00338-7

[133] J. D. Adams, U. Kim, and H. T. Soh, "Multitarget magnetic activated cell sorter." *Proc. Natl. Acad. Sci. U. S. A.*, vol. 105, no. 47, pp. 18 165–18 170, Nov 2008. doi:10.1073/pnas.0809795105

[134] N. Pamme, "Continuous flow separations in microfluidic devices." *Lab Chip*, vol. 7, no. 12, pp. 1644–1659, Dec 2007. doi:10.1039/b712784g

[135] J. Liu, J. D. Andya, and S. J. Shire, "A critical review of analytical ultracentrifugation and field flow fractionation methods for measuring protein aggregation." *AAPS J.*, vol. 8, no. 3, pp. 580–589, 2006. doi:10.1208/aapsj080367

[136] B. Roda, A. Zattoni, P. Reschiglian, M. H. Moon, M. Mirasoli, E. Michelini, and A. Roda, "Field-flow fractionation in bioanalysis: A review of recent trends." *Anal. Chim. Acta*, vol. 635, no. 2, pp. 132–143, Mar 2009. doi:10.1016/j.aca.2009.01.015

[137] M. P. MacDonald, G. C. Spalding, and K. Dholakia, "Microfluidic sorting in an optical lattice." *Nature*, vol. 426, no. 6965, pp. 421–424, Nov 2003. doi:10.1038/nature02144

[138] D. Pappas and K. Wang, “Cellular separations: a review of new challenges in analytical chemistry.” *Anal. Chim. Acta*, vol. 601, no. 1, pp. 26–35, Oct 2007. doi:10.1016/j.aca.2007.08.033

[139] M. Yamada, M. Nakashima, and M. Seki, “Pinched flow fractionation: continuous size separation of particles utilizing a laminar flow profile in a pinched microchannel.” *Anal. Chem.*, vol. 76, no. 18, pp. 5465–5471, Sep 2004. doi:10.1021/ac049863r

[140] M. Yamada and M. Seki, “Microfluidic particle sorter employing flow splitting and recombining.” *Anal. Chem.*, vol. 78, no. 4, pp. 1357–1362, Feb 2006. doi:10.1021/ac0520083

[141] K. B. Andersen, S. Levinsen, W. E. Svendsen, and F. Okkels, “A generalized theoretical model for ”continuous particle separation in a microchannel having asymmetrically arranged multiple branches”.” *Lab Chip*, vol. 9, no. 11, pp. 1638–1639, Jun 2009. doi:10.1039/b822959g

[142] H. A. Pohl, “The motion and precipitation of suspensoids in divergent electric fields.” *J. Appl. Phys.*, vol. 22, pp. 869–871, 1951. doi:10.1063/1.1700065

[143] T. B. Jones, *Electromechanics of particles.* Cambridge University Press, 1995.

[144] I. Doh and Y. H. Cho, “A continuous cell separation chip using hydrodynamic dielectrophoresis (DEP) process.” *Sens. Actuators A*, vol. 121, pp. 59–65, 2005. doi:10.1016/j.sna.2005.01.030

[145] Y. Li, C. Dalton, H. J. Crabtree, G. Nilsson, and K. V. I. S. Kaler, “Continuous dielectrophoretic cell separation microfluidic device.” *Lab Chip*, vol. 7, no. 2, pp. 239–248, 2007. doi:10.1039/b613344d

[146] T. Braschler, N. Demierre, E. Nascimento, T. Silva, A. G. Oliva, and P. Renaud, “Continuous separation of cells by balanced dielectrophoretic forces at multiple frequencies.” *Lab Chip*, vol. 8, no. 2, pp. 280–286, Feb 2008. doi:10.1039/b710303d

[147] N. Demierre, T. Braschler, R. Muller, and P. Renaud, “Focusing and continuous separation of cells in a microfluidic device using lateral dielectrophoresis.” *Sens. Actuators B*, vol. 132, pp. 388–396, 2008. doi:10.1016/j.snb.2007.09.078

[148] L. Wang, J. Lu, S. A. Marchenko, E. S. Monuki, L. A. Flanagan, and A. P. Lee, “Dual frequency dielectrophoresis with interdigitated sidewall electrodes for microfluidic flow-through separation of beads and cells.” *Electrophoresis*, vol. 30, pp. 1–10, 2009. doi:10.1002/elps.200800637

[149] K. H. Han and A. B. Frazier, “Lateral-driven continuous dielectrophoretic microseparators for blood cells suspended in a highly conductive medium.” *Lab Chip*, vol. 8, pp. 1079–1086, 2008. doi:10.1039/b802321b

[150] I. F. Cheng, V. E. Froude, Y. Zhu, H. C. Chang, and H. C. Chang, “A continuous high-throughput bioparticle sorter based on 3d traveling-wave dielectrophoresis.” *Lab Chip*, vol. 9, no. 22, pp. 3193–3201, Nov 2009. doi:10.1039/b910587e

[151] I. F. Cheng, C. C. Chung, and H. C. Chang, “High-throughput electrokinetic bioparticle focusing based on a travelling-wave dielectrophoretic field.” *Microfluid. Nanofluid.*, pp. 1–12, 2010. doi:10.1007/s10404-010-0699-8

[152] L. Cui and H. Morgan, “Design and fabrication of travelling wave dielectrophoresis structures.” *J. Micromech. Microeng.*, vol. 10, pp. 72–79, 2000. doi:10.1088/0960-1317/10/1/310

[153] D. W. Inglis, N. Herman, and G. Vesey, “Highly accurate deterministic lateral displacement device and its application to purification of fungal spores.” *Biomicrofluidics*, vol. 4, p. 024109, 2010. doi:10.1063/1.3430553

[154] J. P. Beech, P. Jönsson, and J. O. Tegenfeldt, “Tipping the balance of deterministic lateral displacement devices using dielectrophoresis.” *Lab Chip*, vol. 9, pp. 2698–2706, 2009. doi:10.1039/b823275j

[155] S. Kostner, S. van den Driesche, W. Witarski, S. Pastorekova, and M. J. Vellekoop, “Guided dielectrophoresis: a robust method for continuous particle and cell separation.” *IEEE Sens. J.*, vol. 10, pp. 1440–1446, 2010. doi:10.1109/jsen.2010.2044787

[156] S. van den Driesche, S. Kostner, W. Witarski, and M. J. Vellekoop, “A strip electrode design for robust continuous cell separation based on positive and negative dielectrophoresis.” in *Proceedings of the 13th International Conference on Miniaturized Systems for Chemistry and Life Science, μTAS*, Jeju Island, Korea, Nov 2009, pp. 1473–1475.

[157] S. Kostner, “Sensors and actuators for single particles and cells.” Ph.D. dissertation, Vienna University of Technology, Oct 2009.

[158] F. Bezanilla, “Ion channels: from conductance to structure.” *Neuron*, vol. 60, no. 3, pp. 456–468, Nov 2008. doi:10.1016/j.neuron.2008.10.035

[159] C. D. Resta and A. Becchetti, “Introduction to ion channels.” *Adv. Exp. Med. Biol.*, vol. 674, pp. 9–21, 2010.

[160] T. B. Jones, “Basic theory of dielectrophoresis and electrorotation.” *IEEE Eng Med Biol*, vol. 22, no. 6, pp. 33–42, Nov. 2003. doi:10.1109/MEMB.2003.1304999

[161] R. Hine, *Membrane, the facts on file dictionary of biology.*, 3rd ed. New York: Checkmark Books,

1999.

[162] H. P. Schwan and S. Takashima, "Dielectric behavior of biological cells and membranes." *Bull. Inst. Chem. Res., Kyoto Univ.*, vol. 69, no. 4, pp. 459–475, 1991.

[163] P. Gascoyne, F. F. Becker, and X. B. Wang, "Numerical analysis of the influence of experimental conditions on the accuracy of dielectric parameters derived from electrorotation measurements." *Bioelectrochem. Bioenerg.*, vol. 36, pp. 115–125, 1995. doi:10.1016/0302-4598(94)05015-M

[164] K. L. Chan, P. Gascoyne, F. Becker, and R. Pethig, "Electrorotation of liposomes: verification of the dielectric multi-shell model for cells." *Biochim. Biophys. Acta*, vol. 1349, pp. 182–196, 1997. doi:10.1016/S0005-2760(97)00092-1

[165] D. Puchberger-Enengl, "Dielectrophoresis-based characterization and separation of cells." Master's thesis, Vienna University of Technology, 2009.

[166] R. Pethig and M. S. Talary, "Dielectrophoretic detection of membrane morphology changes in jurkat t-cells undergoing etoposide-induced apoptosis." *IET Nanobiotechnol.*, vol. 1, no. 1, pp. 2–9, Feb. 2007. doi:10.1049/iet-nbt:20060018

[167] Y. Huang, R. Hlzel, R. Pethig, and X. Wang, "Differences in the ac electrodynamics of viable and non-viable yeast cells determined through combined dielectrophoresis and electrorotation studies." *Phys. Med. Biol.*, vol. 37, no. 7, pp. 1499–1517, 1992. doi:10.1088/0031-9155/37/7/003

[168] H. Feldmann, "Yeast molecular biology." Available online, visited 05.10.2009, University of Munich, 2005, http://biochemie.web.med.uni-muenchen.de/Yeast_Biol.

[169] P. Bican and B. Blanc, "Partial characterization of *Lactobacillus lactis* cell envelope proteins." *J. Dairy Sci.*, vol. 64, no. 3, pp. 384–390, 1981.

[170] S. van den Driesche, V. Rao, D. Puchberger, W. Witarski, and M. J. Vellekoop, "Continuous separation of viable cells by travelling wave dielectrophoresis." in *Procedia Engineering 5*, B. Jakoby and M. J. Vellekoop, Eds. Linz, Austria: Elsevier B.V., Sep 2010, p. 4144. doi:10.1016/j.proeng.2010.09.043

[171] S. van den Driesche, V. Rao, D. Puchberger-Enengl, W. Witarski, and M. J. Vellekoop, "Continuous cell from cell separation by traveling wave dielectrophoresis." *Sens. Actuators B*, 2011. doi:10.1016/j.snb.2011.01.012

[172] G. Fuhr, R. Hagedorn, T. Muller, B. Wagner, and W. Benecke, "Linear motion of dielectric particles and living cells in microfabricated structures induced by traveling electric fields." in *Proc. 'An Investigation of Micro Structures, Sensors, Actuators IEEE Machines and Robots' Micro Electro Mechanical Systems, MEMS '91*, Jan.30-Feb.2 1991, pp. 259–264. doi:10.1109/MEMSYS.1991.114807

[173] P. Gascoyne, C. Mahidol, M. Ruchirawat, J. Satayavivad, P. Watcharasit, and F. F. Becker, "Microsample preparation by dielectrophoresis: isolation of malaria." *Lab Chip*, vol. 2, pp. 70–75, 2002. doi:10.1039/b110990c

[174] X. B. Wang, Y. Huang, X. Wang, F. F. Becker, and P. R. Gascoyne, "Dielectrophoretic manipulation of cells with spiral electrodes." *Biophys. J.*, vol. 72, no. 4, pp. 1887–1899, Apr 1997. doi:10.1016/S0006-3495(97)78834-9

[175] K. Pant, J. Feng, G. Wang, S. Krishnamoorthy, and S. Sundaram, "Separation of bioparticulate matter using traveling wave dielectrophoresis." in *Proceedings of µTAS*, M. A. Northrup, K. F. Jensen, and D. J. Harrison, Eds., 2003, pp. 1207–1210.

[176] D. R. Lide, *Handbook of chemistry and physics.*, 87th ed. CRC Press, 2006.

[177] P. R. C. Gascoyne, X. B. Wang, Y. Huang, and F. F. Becker, "Dielectrophoretic separation of cancer cells from blood." *IEEE T. Ind. Appl.*, vol. 33, no. 3, pp. 670–678, May 1997. doi:10.1109/28.585856

[178] L. Bezrukov, P. S. Blank, I. V. Polozov, and J. Zimmerberg, "An adhesion-based method for plasma membrane isolation: Evaluating cholesterol extraction from cells and their membranes." *Anal. Biochem.*, vol. 394, pp. 171–176, 2009. doi:10.1016/j.ab.2009.07.027

[179] P. K. Zarzycki, M. A. Bartoszuk, and A. I. Radziwon, "Optimization of TLC detection by phosphomolybdic acid staining for robust quantification of cholesterol and bile acids." *J. Planar Chromatogr.*, vol. 19, pp. 52–57, 2006. doi:10.1556/jpc.19.2006.1.9

About the Author

Sander van den Driesche was born in Rotterdam, the Netherlands, in 1978. Between 1998 and 2001 he studied Electrical Engineering at Delft University of Technology. He received the B.Sc. degree in Life Science and Technology from Delft University of Technology in 2004 and the Ir. (M.Sc.) degree, specialisation in cell diagnostics, in 2006. His M.Sc. thesis topic was the development of a high throughput method for biochemical assays on single mammalian cells in nanotiter plates. Between 2007 and 2011 he was working in the European Ph.D. project: On-Chip Cell Handling and Analysis “CellCheck”, project number MRTN-CT-2006-035854, at the Vienna University of Technology, Austria.